Wolfgang Mader

Estimating states and interactions in complex systems

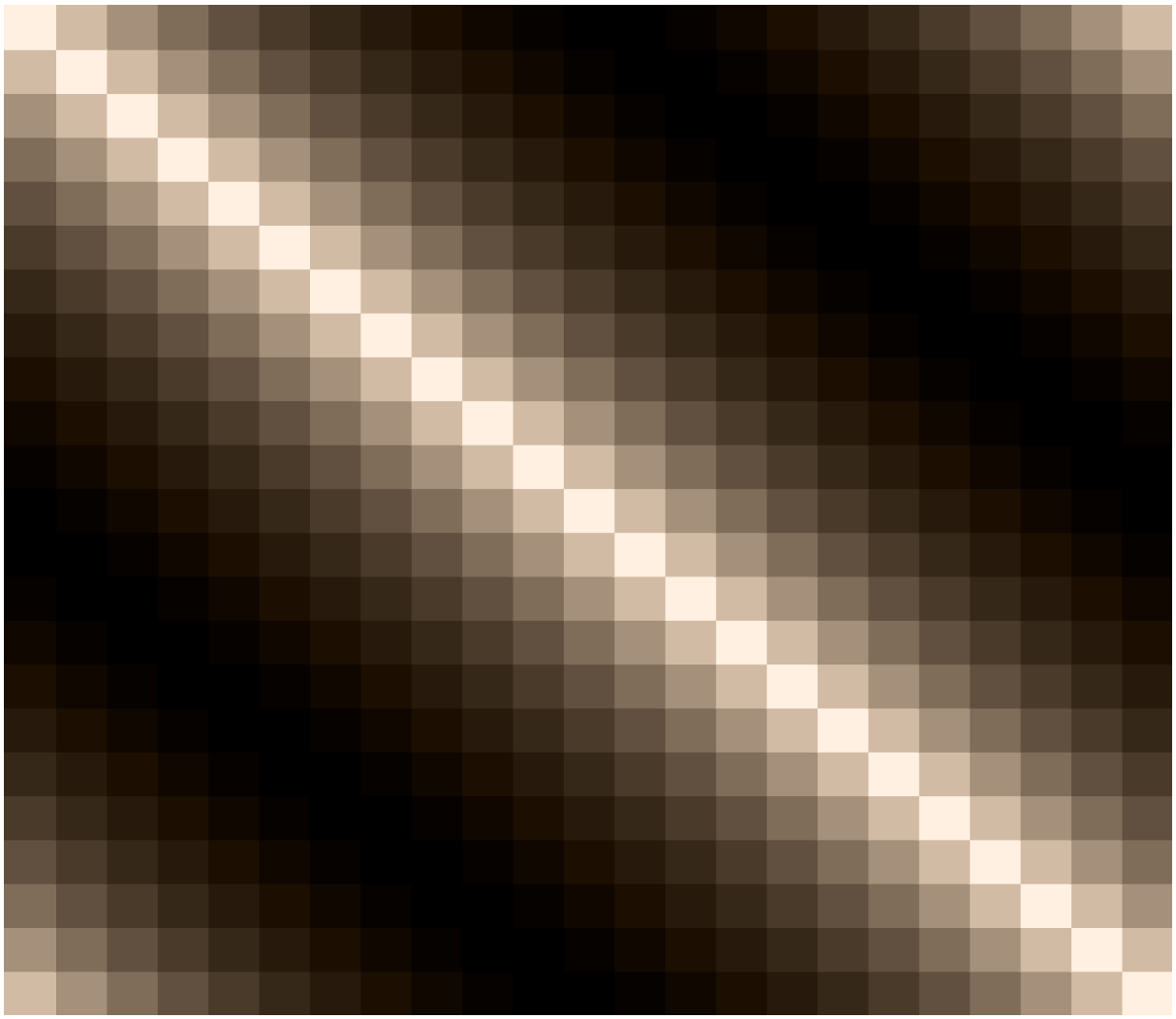

UNI FREIBURG

Albert-Ludwigs-Universität Freiburg
Fakultät für Mathematik und Physik

Estimating states and interactions in complex systems

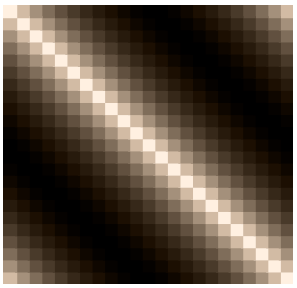

Dissertation
zur Erlangung des Doktorgrades
der Fakultät für Mathematik und Physik
der
Universität Freiburg im Breisgau

vorgelegt von
Wolfgang Mader
im April 2016

UNI FREIBURG

Dekan:	Prof. Dr. Dietmar Kröner
Betreuer der Arbeit:	Prof. Dr. Jens Timmer
Referent:	Prof. Dr. Jens Timmer
Koreferent:	Prof. Dr. Alexander Blumen
Prüfer (Experimentalphysik):	Prof. Dr. Günter Reiter
Prüfer (Theoretische Physik):	apl. Prof. Dr. Thomas Filk
Datum der mündlichen Prüfung:	23. Juni 2016

Published articles

2015

- A. Raue et al. Data2Dynamics: a modeling environment tailored to parameter estimation in dynamical systems. *Bioinformatics*, 32(21):3558–3560, 2015
- W. Buchenberg, W. Mader, G. Hoppe, R. Lorenz, M. Menza, M. Buechert, J. Timmer, and B. Jung. In vitro study to simulate the intracardiac magnetohydrodynamic effect. *Magnetic Resonance in Medicine*, 74(3):850–857, 2015
- W. Mader, M. Mader, J. Timmer, M. Thiel, and B. Schelter. Networks: On the relation of bi- and multivariate measures. *Scientific Reports*, 5:10805, 2015
- L. Sommerlade, M. Thiel, M. Mader, W. Mader, J. Timmer, B. Platt, and B. Schelter. Assessing the strength of directed influences among neural signals: An approach to noisy data. *Journal of Neuroscience Methods*, 239:47–64, 2015

2014

- M. Mader, W. Mader, B. Gluckman, J. Timmer, and B. Schelter. Statistical evaluation of forecasts. *Physical Review E*, 90(2), 2014
- W. Mader, Y. Linke, M. Mader, L. Sommerlade, J. Timmer, and B. Schelter. A numerically efficient implementation of the expectation maximization algorithm for state space models. *Applied Mathematics and Computation*, 241:222–232, 2014
- L. Sommerlade, M. Mader, W. Mader, J. Timmer, M. Thiel, C. Grebogi, and B. Schelter. Optimized spectral estimation for nonlinear synchronizing systems. *Physical Review E*, 89(3), 2014
- B. Schelter, M. Mader, W. Mader, L. Sommerlade, B. Platt, YC. Lai, C. Grebogi, and M. Thiel. Overarching framework for data-based modelling. *EPL*, 105(3), 2014

2013

- Y. Vives-Gilabert, A. Abdulkadir, C. Kaller, W. Mader, R. Wolf, B. Schelter, and S. Kloppel. Detection of preclinical neural dysfunction from functional connectivity graphs derived from task fMRI. An example from degeneration. *Psychiatry Research-Neuroimaging*, 214(3):322–330, 2013
- M. Mader, W. Mader, L. Sommerlade, J. Timmer, and B. Schelter. Block-bootstrapping for noisy data. *Journal of Neuroscience Methods*, 219(2):285–295, 2013

2012

- M. Killmann, L. Sommerlade, W. Mader, J. Timmer, and B. Schelter. Inference of time-dependent causal influences in Networks. *Biomedical Engineering*, 57(1), 2012
- D.-B. den Ouden, D. Saur, W. Mader, B. Schelter, S. Lukic, E. Wali, J. Timmer, and C. Thompson. Network modulation during complex syntactic processing. *NeuroImage*, 59(1):815–823, 2012

2010 and earlier

- D. Saur, B. Schelter, S. Schnell, D. Kratochvil, H. Küpper, P. Kellmeyer, D. Kümmerer, S. Klöppel, V. Glauche, R. Lange, W. Mader, D. Feess, J. Timmer, and C. Weiller. Combining functional and anatomical connectivity reveals brain networks for auditory language comprehension. *NeuroImage*, 49(4):3187–3197, 2010
- W. Mader, D. Feess, R. Lange, D. Saur, R. Lange, V. Glauche, C. Weiller, J. Timmer, and B. Schelter. Investigating multivariate systems using directed partial correlation. *International Journal of Bioelectromagnetism*, 12(1):21–25, 2010
- W. Mader, D. Feess, R. Lange, D. Saur, V. Glauche, C. Weiller, J. Timmer, and B. Schelter. On the detection of direct directed information flow in fMRI. *IEEE Journal of Selected Topics in Signal Processing*, 2(6):965–974, 2008

In preparation

- W. Mader, W. Buchenberg, M. Mader, B. Schelter, and J. Timmer. Reconstruction of the cardiac ECG signal in a MRI environment. *Insights in Medical Physics*, in preparation

Book chapters

- L. Sommerlade, M. Thiel, B. Platt, A. Plano, G. Riedel, C. Grebogi, W. Mader, M. Mader, J. Timmer, and B. Schelter. Time-Variant Estimation of Connectivity and Kalman's Filter. In: K. Sameshima and L. Baccala, editors, *Methods in Brain Connectivity Inference through Multivariate Time Series Analysis*, chapter 9, pages 161–177. Florida: CRC Press, 2014
- B. Schelter, M. Thiel, M. Mader, and W. Mader. Signal Processing of the EEG: Approaches tailored to Epilepsy. In: R. Tetzlaff, C. Elger, and K. Lehnertz, editors, *Recent Advances in Predicting and Preventing Epileptic Seizures: Proceedings of the 5th International Workshop on Seizure Prediction*, chapter 9, pages 119–131. Singapore: World Scientific Publishing Co Pte Ltd, 2013

Conference talks

- Networks: On the relation of bi- and multivariate measures, XXXIV Dynamics Days Europe, Bayreuth, 2014
- On the detection of direct directed information flow in fMRI, Biosignalverarbeitung, Potsdam, 2008

Reviewer for

- Engineering Science and Technology
- Transactions on Biomedical Engineering

Contents

Introduction

Science has a long tradition in exploring a subject by examining its parts. This is done with the anticipation that findings about the parts of a subject yield knowledge about the subject itself. This successful strategy facilitated the development of sophisticated measurement devices and experiments, from the microscope to telescopes, spectrometers, and particle accelerators. In biology, this approach has led from the description of the anatomy of e.g., plants and animals, to a detailed understanding of the construction and function on the cellular level [1]. Chemistry has started with describing chemical reactions on the level of atoms but has nowadays developed a branch called quantum chemistry, where results from quantum mechanics are used in order to e.g., describe the electron transfer process at electrochemical interfaces such as provided by a metal electrode placed in an electrolyte solution [2].

With the construction of the Large Hadron Collider, physics makes the largest effort in science in learning about the most fundamental parts from which matter is built. The standard model of particle physics is a result of this effort. It classifies all known subatomic particles and describes the most important fundamental forces acting on them. While the standard model is not the only fundamental theory, the discovery of a boson in 2012 which so far conforms to the Higgs boson predicted within the standard model has strengthened its case [3, 4].

For sciences dealing with subjects built from matter, the idea might occur that by investigating the most fundamental parts of matter, particle physics is the basic science from which all other sciences can be derived. Many-body physics is concerned with effects manifesting in large ensembles of bosons and fermions only, such as magnetism or superconductivity. Thus, even though these particles are described in the standard model, their collective behavior is fundamentally different from their behavior when treated as free particles. Consequently, many-body physics, is not just applied particle physics. Further up the scale one finds that biology is not just applied cell biology, and behavioral science is not just applied biology. Each science deals with new phenomena whose description demands new laws, concepts, and generalizations [5].

An example for such an *emergent* phenomenon is friction. Forces between elementary particles are conservative. However, even though macroscopic structures are built

from elementary particles, motion on the macroscopic scale can be a dissipative process. This is due to the fact that the surface of a macroscopic structure can convert mechanical energy into thermal energy, a property not described on the scale of elementary particles. Another example is the concept of temperature or pressure as defined in thermodynamics. On the scale of fundamental particles such as atoms or molecules, the motion of each particle must be described. Only for an ensemble of particles the notion of temperature and pressure is definable.

Systems with emergent phenomena are termed *complex systems*. The study of complex systems is the study of the *interaction* of the parts of a system. Particularly, the collective behavior of the parts which emerges from their interaction is studied [6, 7]. Prominent complex systems are social societies, the brain, the stock market, or the signaling in living cells [6, 8–11].

An important tool for studying complex systems is network theory [12–20]. A complex system is modeled as a network by identifying its individual parts as nodes and modeling the interaction between its parts as links. A network provides an accessible visual representation of a complex system. By means of its network representation a complex system can also be treated mathematically.

In application, the network representing a complex systems is constructed based on observations. The nodes of such an empirical network are commonly defined by the recording sites, its links are established by applying a measure of interdependence such as the correlation coefficient to the observations. The correlation coefficient is a bivariate measure, i.e., the recordings of two nodes are taken into account while the recordings of all other nodes are disregarded. Bivariate methods lead to so-called *indirect* links in a network. An indirect link suggests a direct interaction between two nodes, even though the latter share no direct physical connection in the system under investigation. The physical interaction of the two nodes is indirect, which leads to the term indirect link. Indirect links are spurious and a known peculiarity of bivariate measures [21]. However, the fundamental argument for indirect links to arise in the context of bivariate measures is missing. This argument is derived in the course of the first part of the present thesis. To this end, the notion of networks, network models, and network classes is introduced in Chap. 1.

In Chap. 2, the task of network reconstruction from data is discussed such that the cause for the emergence of indirect links is revealed. The interdependence measure for establishing the links in an empirical network yields a coefficient of the respective measure. This can e.g., be the correlation coefficient. All such coefficients can be collected in a matrix which then characterizes the interaction structure of the entire system as assessed by the measure.

Bivariate measures can be generalized to the multivariate domain. Multivariate measures include the entire set of measurements when assessing the relation of two nodes. By virtue of a linear regression, a multivariate measure can be derived for each bivariate one. For the correlation coefficient, the partial correlation coefficient is the multivariate counterpart. Such a multivariate measure relates to its bivariate one by the inversion of the matrix of interaction coefficients of the latter. The missing

argument for the emergence of indirect links is derived by finding the relation in the other direction, from the bivariate measure to the multivariate measure.

To challenge the theory established in Chap. 2, a series of simulation studies is conducted in Chap. 3. On the example of the correlation coefficient, the results illustrate that bivariate measures yield indirect links as predicted by the theory. Moreover, the classification of a network is shown to be affected. It is shown that a random network once analyzed by a bivariate interdependence measure is indistinguishable from a small-world network [22]. Therefore, despite the common practice [11, 15, 23–26], it is not reasonable to claim a complex system to conform to the small-world model when its interaction structure is inferred by an bivariate interdependence measure.

The partial correlation coefficient is adequate in avoiding indirect links as long as the states of all relevant parts of the complex system are directly observed and the observation is independent identically normally distributed. However, a complex system consisting of dynamical subsystems exhibits temporal correlations. Observational noise usually prevents the direct observation of states. Such empirical data can be modeled by the state-space model (SSM). In the linear SSM, the state of the system is modeled by an autoregressive process, its observation by a stochastic linear function. The state of the system in the SSM is optimally estimated by the so-called Kalman filter [27]. As the Kalman filter is model-based, it requires the parameter values of the SSM. These values can either be provided by external knowledge or can be estimated. Based on the estimated parameters, a set of interdependence measures has been proposed [18, 28–31]. Employing these interdependence measures renders a reliable identification of network links possible even if the observed system is dynamic and measurements are prone to observational noise. A maximum-likelihood estimator (MLE) of the parameters in the SSM has been constructed using the expectation-maximization (EM) algorithm [32]. The major drawback of this algorithm is its computational complexity resulting in long runtimes. In Chap. 4, strategies for reducing the complexity of the EM algorithm are presented. The implementation of these strategies allows the application of the EM algorithm to large data sets [33]. A simulation study comparing the conventional and the optimized EM algorithm validates the significant reduction in runtime by two orders of magnitude [34]. The source code of the optimized algorithm is freely available. *

In Chap. 5, a state-estimation problem is considered. It addresses the situation where an electrocardiogram (ECG) is recorded in the presence of an external magnetic field, such as inside a magnetic resonance imaging (MRI) scanner. In this situation, the ECG is the superposition of the electrical activity of the heart and the Hall voltage evoked by the Lorentz force acting on ions dissolved in blood. The Hall voltage is commonly called magnetohydrodynamic (MHD) signal. The total ECG is referred to as MHD-ECG. To date, it is an unsolved problem to reliably reconstruct the electrical activity of the heart from the MHD-ECG. A possible solution is proposed in Chap. 5. The approach employs the extended Kalman filter for state estimation.

*https://github.com/wmader/fdmb

In the Kalman filter, model prediction and observation are weighted such that the mean squared prediction error is minimized [27]. To this end it is assumed that the observational noise is independent identically normally distributed. Since the MHD signal leads to temporally correlated non-normally distributed observational noise, the extended Kalman filter needs adaptions. In Chap. 5, it is proposed that the amount of model-based smoothing applied to the state estimate is adjusted manually. At the example of an application, the effect of this tuning is demonstrated. It is shown that under certain assumptions, the proposed filtering procedure is capable of reconstructing the cardiac ECG from measurements recorded inside a MRI scanner.

Part I.

Network reconstruction and classification

Chapter 1.

Networks: definition, properties, and models

In this chapter networks are defined, fundamental network properties are discussed, and models for regular, random, and small-world networks are presented.

A possibility to model and visualize complex systems is their description by networks. To this end, the entities of the complex system are denoted nodes and their relations are denoted links [7, 35, 36]. Complex systems which have been investigated based on their network description include power grids [12], traffic networks [13, 14], disease spreading [37], climate networks [15], stock market interactions [16, 17], and biological networks such as the interaction of different areas in the human brain [18–20]. This list, despite incomplete, motivates the usefulness of the network approach in a variety of fields. Mathematically, networks are treated by tools from graph theory [38].

The purpose of this chapter is to give an overview of network theory on which successive chapters built upon. Networks are defined in Sec. 1.1. Core properties of networks are introduced and discussed in Sec. 1.2. The characteristics of models for regular, random, and small-world networks are established in Sec. 1.3. In order to distinguish these three network models, the average distance and the clustering coefficient can be employed. Hence, their behavior within the three network models is discussed in detail.

1.1. Definition of a network

A *network* $G = (\mathfrak{N}, \mathfrak{L})$ is defined as a set of *nodes* $\mathfrak{N} = \{n_1, n_2, \ldots, n_N\} \neq \emptyset$ of size $N = |\mathfrak{N}|$, and a set of *links* $\mathfrak{L} = \{l_1, l_2, \ldots, l_M\}$ enumerated from 1 to $M = |\mathfrak{L}|$. A link l_k joins two nodes, say n_i and n_j. Accordingly, this link is alternatively denoted $l_{ij} = (n_i, n_j)$ [39]. The *adjacency matrix* $\boldsymbol{A}$ is a $N \times N$ matrix describing the topology

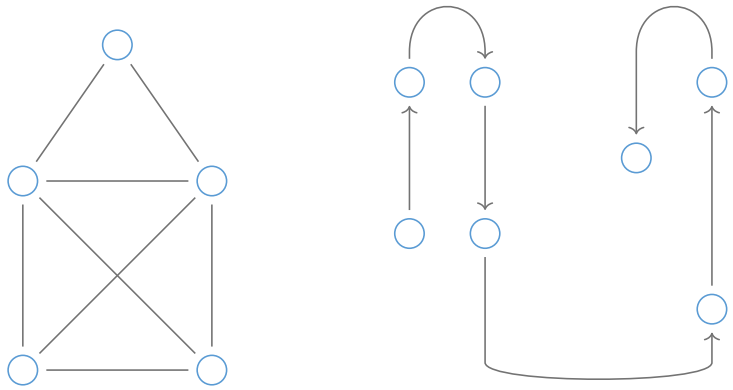

(a) Undirected network (b) Directed network

Figure 1.1.: Graphical representation of an (a) undirected and a (b) directed network. While the directed network could have been drawn in a straight line, it is arranged to reassemble the seven bridges of Königsberg which motivated Leonhard Euler to start the field of graph theory in 1736 [41].

of the network. It is $A_{ij} = 1$ if $l_{ij} \in \mathfrak{L}$, and zero otherwise. The diagonal of $\boldsymbol{A}$ is zero [39].

Undirected networks If l_{ij} is an unordered pair of nodes, then $l_{ij} \in \mathfrak{L} \Leftrightarrow l_{ji} \in \mathfrak{L}$. Such a link carries no directional information, and a network solely possessing such links is called *undirected* [→ Fig. 1.1 (a)]. The associated adjacency matrix $\boldsymbol{A}$ is symmetric. By arranging nodes in rows and links in columns, the $N \times M$ *incidence matrix* $\boldsymbol{B}$ is constructed. It is $B_{ij} = 1$ if l_j is attached to n_i, and zero otherwise. The adjacency and incidence matrices are connected by $\boldsymbol{A} = \Theta\left(\boldsymbol{B}\boldsymbol{B}^{\mathrm{T}}\right) - \boldsymbol{I}$ [40], where $\Theta(\cdot)$ denotes the componentwise Heaviside step function and $(\cdot)^{\mathrm{T}}$ matrix transposition. The maximum number of links in an undirected network is $N(N-1)/2$. If attained, the network is called *complete* [40].

Directed networks In a *directed* network, l_{ij} is an ordered pair of nodes. Therefore, $l_{ij} \in \mathfrak{L}$ no longer implies $l_{ji} \in \mathfrak{L}$. It is possible to move from n_j to n_i along l_{ij}, but not the other way round [→ Fig. 1.1 (b)]. With respect to node n_k, links leading away from n_k are called *outgoing* links, while links leading towards n_k are called *incoming* links. The link l_{ij} is thus an outgoing links with respect to n_j and an incoming one with respect to n_i. In general, the adjacency matrix of a directed network is not symmetric. A directed network is complete if there are $N(N-1)/2$ outgoing as well as incoming links.

1.2. Properties of networks

This section introduces network properties which are of interest to describe and discriminate regular, random, and small-world networks. Specifically, these are the node degree, distance, clustering coefficient, and efficiency.

1.2.1. Node degree

The *degree* g_k of node n_k is the number of links attached to n_k. In undirected networks it is

$$g_k = \sum_{i=1}^{N} A_{ik} = \sum_{j=1}^{N} A_{kj} \,. \tag{1.1}$$

In directed networks, the degree of outgoing links is $g_k^{\mathrm{o}} = \sum_i A_{ik}$, the degree of incoming links is $g_k^{\mathrm{i}} = \sum_j A_{kj}$.

1.2.2. Distance

A *path* is an alternating sequence of nodes and links starting at n_i and ending at n_j. No node is allowed to appear more than once in a path. The *path length* is a function of the path. A common choice is to identify the path length with the number of links in the path. The shortest path connecting n_i and n_j is called *geodesic*. Its length D_{ij} is the *distance* of n_i and n_j. The matrix $\boldsymbol{D}$ is the $N \times N$ matrix of distances in G. For undirected networks, $\boldsymbol{D}$ is symmetric. The maximum of $\boldsymbol{D}$ is the *diameter* e of G [39].

The distance matrix is an important quantity of a network as it quantifies the costs to travel from one node to another. Example costs are time, when sending data packages over the internet [39], money, when transporting goods between cities via railway, or information, when a longer transmission time of messages causes disadvantages in a competitive situation.

If any set of two nodes is connected by a path, G is called *connected*. Otherwise, the network is said to be *disconnected*. In a disconnected network nodes separate in at least two disjoint sets. Each set is termed a *component* of a network [39]. If two nodes n_i and n_j belong to different components, they are not reachable from each other. Conventionally, their distance D_{ij} is set to infinity [42].

The *average distance*

$$L = \frac{1}{N^2} \sum_{i,j=1}^{N} D_{ij} \,. \tag{1.2}$$

quantifies the average separation among all nodes. Subtle variations of this definition are discussed in App. A.1. If G is disconnected, L diverges. By calculating L for the largest component of G only, the divergence of L is avoided [12]. It is also common to

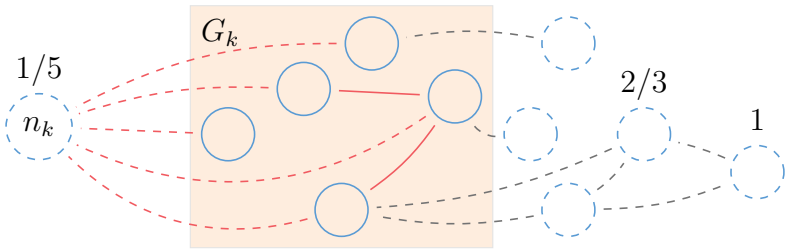

Figure 1.2.: Entire network G, subnetwork G_k, and local clustering coefficient. Each node without a direct connection to n_k is depicted by a dashed circle. This includes n_k itself. Each nodes which shares a links with n_k is depicted by a full circles. The respective link is drawn as a dashed red line. The subnetwork G_k contains exactly all nodes depicted as full circles. The links withing G_k are drawn as solid red lines. All other links are drawn as dashed black lines. As each node in G_k shares a link with n_k in G each link withing G_k induces a triangle about n_k in G established by two dashed red lines and a solid red line. The relative number of triangles about a node is quantified by the local clustering coefficient. For some nodes, the local clustering coefficient is given above the node. Node n_k for example has the local clustering coefficient $c_k = 1/5$, cf., Eq. (1.4)

exclude all paths of infinite length from L [42]. To avoid the ambiguous definition of L for disconnected networks, the *efficiency*

$$E = \frac{1}{N(N-1)} \sum_{i \neq j}^{N} \frac{1}{D_{ij}} \tag{1.3}$$

has been proposed [43]. Evaluated on the entire network G, the *global efficiency* corresponds to the average distance.

Let $\mathfrak{N}_k$ be the set of all direct neighbors of node n_k and $\mathfrak{L}_k$ the links among them. Keep in mind that n_k is not contained in $\mathfrak{N}_k$. The subnetwork of direct neighbor of n_k is given by $\mathfrak{N}_k$ and $\mathfrak{L}_k$. This subnetwork is termed G_k. An example of such as subnetwork in the context of an entire network G is given in Fig. 1.2. Evaluated on G_k, the *local efficiency* corresponds to the local clustering coefficient which is introduced in the following [43, 44].

1.2.3. Clustering coefficient

The local clustering coefficient is a local measure of connectivity. For an undirected network, let $\tilde{\boldsymbol{A}}$ denote the adjacency matrix of G_k. Note that n_k is not part of G_k. Then, the *local clustering coefficient* of n_k is defined as [12]

$$c_k = \begin{cases} \dfrac{2}{g_k(g_k-1)} \displaystyle\sum_{i>j}^{N} \tilde{A}_{ij} & \text{if } g_k \geq 2, \\ 0 & \text{otherwise.} \end{cases} \tag{1.4}$$

By construction, each pair of nodes (n_i, n_j) part of G_k is connected in G by a path of length two going through n_k

Consequently, each link in G_k yields a triangle about n_k in G. This is also illustrated in Fig. 1.2. The maximum number of links in G_k is $(g_k(g_k-1))/2$. The sum over $\tilde{A}_{ij}$ in Eq. (1.4) counts the actual number of links in G_k. Therefore, the local clustering coefficient $0 \leq c_k \leq 1$ is the ratio of existing and possible triangles about n_k [→ Fig. 1.2].

Alternatively, the local clustering coefficient can be calculated from the adjacency matrix $\boldsymbol{A}$ of G directly [39],

$$c_k = \begin{cases} \dfrac{1}{g_k(g_k-1)} \displaystyle\sum_{i,j=1}^{N} A_{ki}A_{ij}A_{jk} & \text{if } g_k \geq 2, \\ 0 & \text{otherwise.} \end{cases} \tag{1.5}$$

By averaging c_k over the entire network G, the average clustering coefficient, or short the *clustering coefficient*,

$$C = \frac{1}{N}\sum_{k=1}^{N} c_k \tag{1.6}$$

is defined.

The definition of the local clustering coefficient can be generalized naturally to directed networks. Every node then possesses a separate clustering coefficient with respect to its outgoing and incoming links.

Transitivity Originating from the sociology literature, *transitivity* is another measure on how well a network is connected locally [42, 45]. For completeness, a short discussion on the matter can be found in App. A.2.

1.3. Network models

A network model is a set of instructions on how to obtain a specific type of network. Thus, a network might be viewed as the realization of a network model. Each model exhibits specific properties such as a small or large clustering coefficient or a certain probability to separate in more than one component. If the properties of an empirical network G complies with the properties of the, say, small-world model, G is said to belong to the class of small-world networks. Models for regular, random, and small-world networks are discussed in the following. The three models are distinguished by the scaling of the average distance and the clustering coefficient. Thus, the scaling of these properties is discussed in detail for each model.

1.3.1. Regular ring networks

Networks in which all nodes have the same degree g [→ Eq. (1.1)] are called *regular* [40]. A special case within this class are *regular ring* networks [→ Fig. 1.3]. A regular ring network $G_{N,h}$ is determined by its number of nodes N and the number of left-hand neighbors h of each node. The parameter h is in $[0, \lfloor N/2 \rfloor] \subset \mathbb{N}$,* where $\lfloor x \rfloor$ denotes the largest integer smaller than or equal to x. The node degree in $G_{N,h}$ is $g_k = 2h$ for all nodes n_k. As all nodes are equal, a property of a single node matches the respective property averaged over the entire network.

Average distance

In the model for regular ring networks, the average distance

$$L_{\mathrm{rr}} \propto \frac{N}{4h} = \frac{N}{2g_k} \tag{1.7}$$

scales linearly with N [46]. This result together with exact equations for the average distance is derived in App. A.3.

Clustering coefficient

The clustering coefficient in the regular ring model is [46]

$$C_{\mathrm{rr}} = \frac{3h-3}{4h-2}\,. \tag{1.8}$$

This result can be derived by noting that the subnetwork G_k of the neighboring nodes of n_k includes the $2h$ nodes $\{n_{k-h}, \ldots, n_{k+h}\} \setminus \{n_k\}$. Node n_{k-h} is not adjoined with $\{n_{k+1}, \ldots, n_{k+h}\}$, n_{k-h+1} not with $\{n_{k+2}, \ldots, n_{k+h}\}$, and so forth [→ Fig. 1.3]. Consequently, the lower and upper h-triangle of the adjacency matrix $\tilde{\boldsymbol{A}}$ of G_k is zero, leaving

$$M_k = \frac{1}{2}\left[4h^2 - 2h - (h+1)h\right] \tag{1.9}$$

$$= \frac{h}{2}[3h-3] \tag{1.10}$$

links in G_k. The first two terms in Eq. (1.9) count the number of elements in G_k without the diagonal, the last term subtracts the lower and upper h-triangle. Using

*Strictly speaking, for N even, $h = N/2$ leads to two links between one pair of nodes. Since two nodes are allowed to be connected by at most a single link, the second link is dropped.

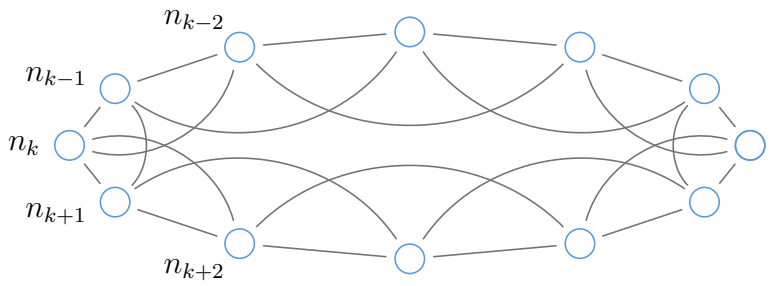

Figure 1.3.: A regular ring network with $N = 12$ and $h = 2$. Direct neighbors of n_k are labeled.

Eq. (1.4) with $g_k = 2h$, the clustering coefficient

$$\begin{aligned} C_{\mathrm{rr}} = c_k &= \frac{2M_k}{g_k(g_k-1)} \\ &= \frac{h(3h-3)}{2h(2h-1)} \\ &= \frac{3h-3}{4h-2} \end{aligned} \tag{1.11}$$

is derived. As $h \gg 1$, C_{rr} approaches $3/4$. Since $0 \leq C \leq 1$, the clustering coefficient is considered large in regular ring networks.

1.3.2. Random network

In the model for random networks considered here, every link is equally likely. Thus, node properties like the degree or the local clustering coefficient are random variables yet with the same probability distribution for each node.

Models of random networks

Interpreting all networks with N nodes and M links as the ensemble of $\binom{\binom{N}{2}}{M}$ possible networks, a *random network* $G_{N,M}$ is obtained by choosing any network from the ensemble with equal probability [47]. Without building up the ensemble in the first place, such a random network can be realized by drawing M links from the ensemble of all $\binom{N}{2}$ possible links without replacement [48]. This model is known as the Erdős-Rényi model of random networks [47].

In a related model, all M links are drawn with replacement from the ensemble of possible links. This model includes the possibility of two nodes being connected by more than one link [49]. In the following, the scaling of L and C in the Erdős-Rényi model is considered.

Scaling of the average distance

From the scaling of the diameter $e(N)$ in a random network [50], the scaling of the average distance

$$L_{\mathrm{rd}}(N) \propto e(N) \propto \ln N \tag{1.12}$$

is derived. Details can be found in App. A.4. Compared to the linear scaling in regular ring networks [→ Eq. (1.7)], the logarithmic scaling of L_{rd} is slow. The average distance in random networks is thus considered small compared to regular ring networks.

Clustering coefficient

Denoting the mean degree $\mathrm{E}(g_k) = z$, the clustering coefficient of $G_{N,M}$ is $C = z/N$ [39] when self-loops were allowed in the network. The Erdős-Rényi model excludes self-loops in its realizations, such that the clustering coefficient is obtained as follows.

A network from the Erdős-Rényi model has $M = Nz/2$ links. The probability of any two nodes being adjacent is

$$\begin{aligned} w &= \frac{2M}{N(N-1)} \\ &= \frac{z}{N-1}\,. \end{aligned} \tag{1.13}$$

The expected number of nodes included in the subnetwork G_k is z. The number of links within G_k is a binomially distributed random variable $X \sim \mathrm{B}\left(\left[\frac{z}{2}(z-1), w\right)\right]$ with expected value

$$\mathrm{E}(X) = \frac{z}{2}(z-1)w = \frac{z(z-1)}{2}\frac{z}{N-1}\,. \tag{1.14}$$

The expected value of the local clustering coefficient is hence

$$\mathrm{E}(c_k) = \frac{2\,\mathrm{E}(X)}{z(z-1)} = \frac{z}{N-1}\,. \tag{1.15}$$

Without self loops, n_k cannot be its own neighbor, yielding $N-1$ in the denominator. Since the derivation of Eq. (1.15) is node independent, the expected value of the local clustering coefficient equals the clustering coefficient

$$C_{\mathrm{rd}} = \mathrm{E}(c_k)\,. \tag{1.16}$$

Scaling of the clustering coefficient

To investigate the scaling of the clustering coefficient with N, the mean degree z is considered constant, such that $\mathrm{E}(c_k)$, Eq. (1.15), is a function of N only. It is readily found that C_{rd} scales as $1/N$. Consequently, as N increases, C_{rd} tends to zero. Compared to regular ring networks, random networks exhibit a small clustering coefficient, except for rather dense networks with $z \approx N$.

1.3.3. Small-world networks

The term *small world* has been introduced to science in 1967 by Stanley Milgram [51]. The discussion on the topic, however, had started in the 1950s with a manuscript which was not published until 1978 [52]. The expression small world refers to the everyday observation that the chain of acquaintance connecting oneself to a random person somewhere on the globe is much shorter than naively expected. This finding leads to the impression that this world must be a small one. The term small-world phenomenon was coined to refer to this finding. Within the scope of network theory, the small-world phenomenon translates to a short average distance, which is intrinsic to random networks.

A second everyday experience is not captured by random networks: a friend of a friend is likely to be a friend of oneself, too. This translates into a large clustering coefficient as in regular ring networks.

In [12], a model which covers both everyday observations and thus resides between regular and random networks is proposed. Realizations of the model can exhibit a short average distance and a large clustering coefficient at the same time. In analogy to the small-world phenomenon, these networks are called small-world networks. Small-world networks are not only found in the context of social groups. Their diverse appearance ranges from biological systems such as the neuronal network of Caenorhabditis elegans [12] to technical ones as the power grid of the western United States of America [12].

The effect of the small-world property in dynamical systems is investigated in [12] within the scope of a simple disease spreading model as well as coupled phase oscillators. It is found that diseases spread quickly on a small-world topology and that the synchronization of phase oscillators happens almost as readily as in a complete network [12].

These findings suggest that small-world networks pass information efficiently. In fact, the efficiency E of small-world networks is high, both on the global and the local scale [43].

The model of small-world networks

The small-world model involves a rewiring strategy starting from a regular ring network $G_{N,h}$. One after the other, each node in $G_{N,h}$ is visited h times. Let $i \in [1, h] \subset \mathbb{N}$ denote the i-th visit of node n_k. The link connecting n_k and n_{k+i} is detached from n_{k+i} and attached to any node in $\mathfrak{N} \setminus \{n_k\}$ with equal probability w. Rewired links usually span longer distances than before. Thus, these links are referred to as *shortcuts* [12].

The small-world model was contrived to obtain networks with a large clustering coefficient as in a regular ring but a much lower average distance. Denote $\bar{C}(w)$ the mean of the clustering coefficient obtained from a set of realizations of the small-world model at rewiring probability w; $\bar{L}(w)$ is the respective mean of the average distance. Since the small-world model equals the regular-ring model at $w = 0$, $\bar{C}(w)/C(0) \approx 1$

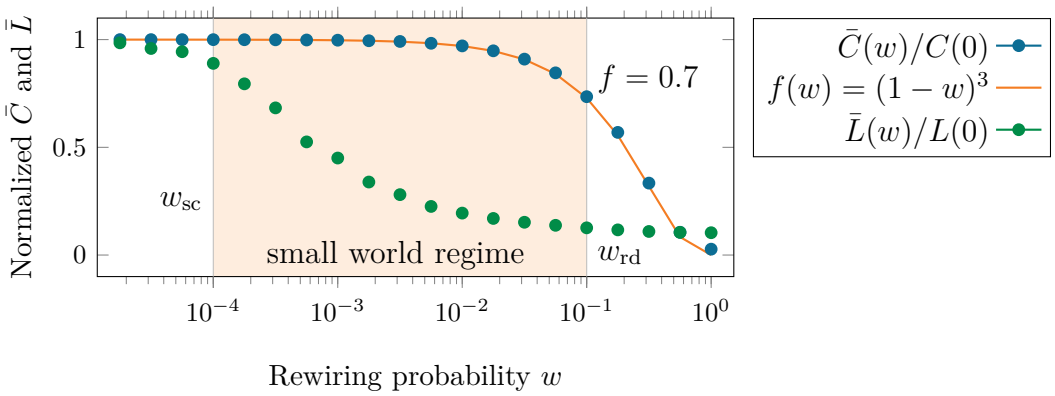

Figure 1.4.: Normalized clustering coefficient $\bar{C}(w)$ and average distance $\bar{L}(w)/L(0)$ in the small-world model averaged over multiple realizations with $N = 1000$ and $h = 10$. The ratio $\bar{L}(w)/L(0)$ undergoes a phase transition at $w_{sc} = (Nh)^{-1} = 10^{-4}$ when the first shortcuts appear [→ Eq. (1.17)]. This rewire probability marks the start of the transition into the small-world regime. The ratio $\bar{C}(w)/C(0)$ complies with $(1-w)^3$ [→ Eq. (1.20)]. At $w = 0.1$, $\bar{C}(w)/C(0)$ is about 0.7 which can be considered as the upper limit of the small-world regime [46]. This figure extends on [12, Fig. 2]

and $\bar{L}(w)/L(0) < 1$ define the small-world regime of the small world model. For a network with $N = 1000$ and $h = 10$, these ratios are depicted in Fig. 1.4 as a function of w averaged over 20 realizations [12].

At small values of w, the regime of regular-ring networks resides [→ Fig. 1.4 and Fig. 1.5, left], where $\bar{C}(w)/C(0) \approx 1$ and $\bar{L}(w)/L(0) \approx 1$.

For an intermediate range of w, shortcuts yield a dramatic decrease of the average distance while the clustering coefficient remains large. In this range, realizations of the small-world model exhibit the small-world property [→ Fig. 1.4]. An example at $w = 0.1$ is given in Fig. 1.5 in the middle.

The regime of random networks resides at large values of w [→ Fig. 1.4 and Fig. 1.5, right]. Both, clustering coefficient and average distance have decreased, such that $\bar{C}(w)/C(0) \approx 0$ and $\bar{L}(w)/L(0) \approx 0$. By means of the average distance and the clustering coefficient, realizations of the small-world model become indistinguishable from realizations of the random network model [12, 46]. It is worth mentioning that even at $w = 1$, the local structure of realizations of the small-world and random model differ [→ Fig. 1.5, right]. Since the starting nodes of all left-hand links are not affected by the rewiring, $g_k \geq h$ for all nodes in a network from the small-world model [46]. The random model allows for $g_k \geq 0$.

Average distance

The average distance starts to drop as the first shortcuts occur. The scaling of the average distance with N than changes from linear as in regular ring network to logarithm as in random networks [53]. This regime is entered once the expected

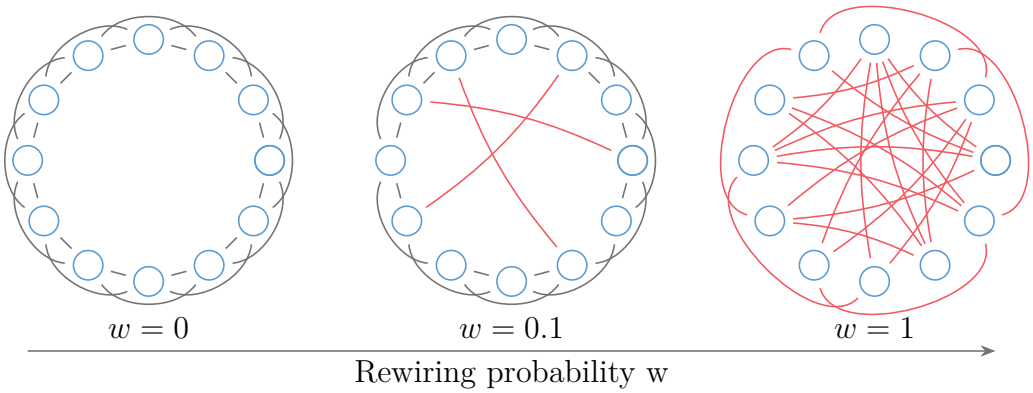

Figure 1.5.: Three realizations of the small-world model with $N = 12$ and $h = 2$. The realization shown on the left is obtained at $w = 0$ and thus equals the initial network $G_{N=12,h=2}$. In the middle, a realization at $w = 0.1$ with three shortcuts (red lines) is presented. At $w = 1$ (right), all links are rewired. However, since only left-hand neighbors are affected by the rewiring procedure, $g_k \geq h \; \forall k$.

number of rewired links $M_\mathrm{r} = wNh$ is equal or larger than one. Thus,

$$w_\mathrm{sc} = \frac{1}{Nh} \tag{1.17}$$

is the critical rewiring probability for shortcuts to arise [53]. For $w \geq w_\mathrm{sc}$, small-world networks might be obtained as realizations of the small-world model.

Clustering coefficient

In the initial network $G_{N,h}$, the clustering coefficient is $C(0) = \frac{3h-3}{4h-2}$ [→ Eq. (1.11), p. 27]. For $w > 0$, the probability for two nodes which were adjacent in G_k at $w = 0$ still being part of and adjacent in G_k is $(1-w)^3$ [46]. This can be seen by recognizing that the probability for one link to stay in place is $1-w$. Consequently, the probability for all three links of a triangle to stay in place is $(1-w)^3$. Rewiring can also add links to G_k. The effect is in the order of $1/N$ as illustrated in Fig. 1.6. In total, after rewiring, the average number of links in G_k is $\frac{h}{2}(3h-3)(1-w)^3 + \mathcal{O}(1/N)$ [→ Eq. (1.10)] [46]. Since the total number of links in G is invariant under rewiring, the mean node degree is constant. Therefore the average number of possible links in G_k remains $h(2h-1)$. By defining the clustering coefficient as the ratio of the mean number of links in G_k to the mean number of possible links in G_k, it takes the form

$$\tilde{C}(w) = \tilde{c}_k(w) = \frac{3h-3}{4h-2}(1-w)^3 + \mathcal{O}\left(\frac{1}{N}\right) \tag{1.18}$$

$$= C(0)(1-w)^3 + \mathcal{O}\left(\frac{1}{N}\right) \tag{1.19}$$

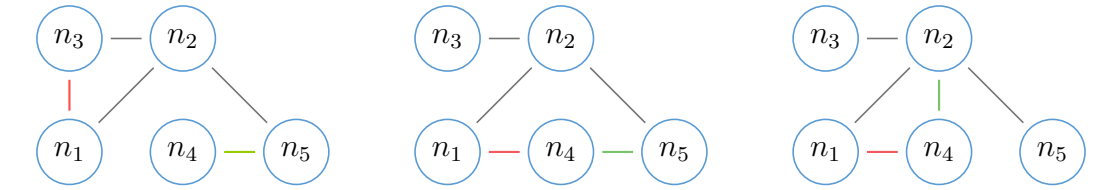

Figure 1.6.: Addition of a link to G_1 by rewiring. The two links which move between sketches are drawn as a red and a green line, respectively. The initial state is shown on the left, in which G_1 consists of the two nodes n_2 and n_3 which are themselves connected. As depicted in the middle, by rewiring l_{13} (red), n_3 is removed from G_1 and some randomly chosen node, here n_4, is added to G_1. Even though n_4 is now part of G_1, it is not *per se* a neighbor of any other node in G_1. Thus, G_1 is currently a network without any link. On the right it is shown that by rewiring l_{45} (green) which is attached to n_4, l_{45} may be connected to a node in G_1. This happens with probability $(wg_1)/N$ which is in the order of $1/N$. This is the reason for the correction in Eq. (1.18).

such that the equation for the ratio

$$\begin{aligned} \frac{\tilde{C}(w)}{C(0)} &\approx (1-w)^3 \\ &=: f(w) \end{aligned} \tag{1.20}$$

is derived. This definition is compatible with the common clustering coefficient in the sense that the dependence on w as well as on N and the physical interpretation remain unchanged [46] as depicted in Fig. 1.4. As $(1-w)^3 < u$ for a fixed $u \in [0,1] \subset \mathbb{R}$, $C(w)$ has decreased to the point where the small-world property is considered lost. Thus,

$$w_{\mathrm{rd}} = 1 - u^{1/3} \tag{1.21}$$

is the critical rewiring probability to leave the small-world regime and enter the random regime of the small-world model. In literature, the value $u = 0.7$ is proposed [46].

Existence of the small-world regime

The preceding discussion assumes that the beginning of the small-world regime is defined by the average distance while the clustering coefficient defines its ending, cf., Fig. 1.4. For the existence of the small-world regime in the model, this implies that the average distance must drop earlier than the clustering coefficient, and consequently $w_{\mathrm{sc}} < w_{\mathrm{rd}}$ must hold. It follows from Eqs. (1.17) and (1.21) that this is the case for

$$N \geq \frac{1}{(1-u^{1/3})\,h} \tag{1.22}$$

nodes in the network. The lower boundary of h can be determined by recognizing that for $h = 1$, the clustering coefficient is zero. Thus, the minimal admissible value for h in the regular ring network initializing the small-world model is 2. Together with $u = 0.7$ from literature [46], Eq. (1.22) determines $N = 5$ as the minimal network size for which a small-world network can be obtained from the model. However, a network with $N = 5$ and $h = 2$ is fully connected, such that the notion small world becomes meaningful only for networks with $N > 5$ nodes. Thus, for all relevant network sizes $N > 5$, ideally $N \gg 5$, a small-world network can be obtained from the small-world model.

Chapter 2.

Network reconstruction based on bivariate and multivariate measures

In this chapter the relation of the bivariate correlation coefficient and its multivariate counterpart, the partial correlation coefficient, is investigated in order to identify the reason for the existence of so-called indirect links. Parts of this chapter are published in [22]: W. Mader, M. Mader, J. Timmer, M. Thiel, and B. Schelter. Networks: On the relation of bi- and multivariate measures. Scientific Reports, 5:10805, 2015 .

In the previous chapter, networks are discussed from a graph-theoretical point of view. This is, nodes and links are accessible such that the properties of networks can readily be investigated. This aspect of network theory finds its application, e.g., when the resilience of a power-grid is concerned or bottlenecks in the throughput of a public transportation system are to be identified.

In the case that networks are used to describe complex systems, regularly, no prior knowledge about nodes and links exists. Instead, the representing network needs to be inferred from measurements. Network nodes are identified with measurement sites [18, 54, 55]. In order to establish links, commonly symmetric bivariate measures are applied to measurements [11]. In particular, the correlation coefficient is frequently employed [15, 24, 26, 56, 57]. The partial correlation coefficient is the multivariate counterpart of the correlation coefficient. In empirical networks, so-called indirect links can occur. An indirect link does not correlate to a direct physical connection. Thus, indirect links hamper the analysis of a complex system by means of its representing network. By exploiting the relation of the bi- and multivariate correlation coefficient, the bivariate correlation coefficient is characterized with respect to the occurrence of indirect links. This characterization provides the yet missing argument why bivariate interdependence measures identify indirect links.

2.1. Complex systems

Networks are used to model and visualize a wide range of *complex systems* such as power grids, traffic systems, social communities, climate, or neuronal systems [12–15, 18–20, 58]. By modeling a system as a network, the system is decomposed into individual entities which are represented as nodes. The links in the network encode the interaction pattern among these entities. It is thus a requirement of the network approach that the system can be decomposed in individual entities. Complex systems suitable for network analysis can be filed in three categories.

Complex systems with explicit network representation Complex systems of this category explicitly provide their network representation. Examples are power grids, in which the nodes are readily identified as power plants, transformer stations, and appliances, or subways, in which subway stations define the nodes. In the former system, links are defined by power lines, in the latter by tracks.

Complex systems with individual entities In contrast to the last category, complex systems of this category provide their set of nodes, but not their set of links. For example social communities naturally decompose into individual entities defining the nodes in the corresponding network. In consequence, also the number and locations of recording sites are determined by the system itself. Links represent the interaction between entities and must be estimated from observations of the dynamics of the entities.

General complex systems In general, both nodes and links must be externally provided. This is, the entities constituting a complex system as well as their interactions are not predefined but must be constructed from data. When modeling the climate or seismic activity, the beginning and ending of a local subsystem might not be clearly definable [59], such that the identification of entities is hampered. In other systems, e.g., the human brain, the resolution of the measurement device might be too poor to resolve individual entities. Theoretically, a brain decomposes without ambiguity into single neurons. It is however impossible nowadays to observe all single neurons and their anatomical connectivity. Measurement techniques such as on-scalp electroencephalography capture the mean activity across a patch of neurons [60], which is not defined by anatomical considerations, but by technical constraints. Beforehand, it is unclear whether each spatial sample point corresponds to an unique functional region of the brain. While the term spatial sampling is intuitive for the following discussion, the sampling problem is not necessarily a truly spatial one. For example, the behavior of individuals can be observed, such that the system is not distributed spatially but across individual persons. In such systems, it is nontrivial or even impossible to tailor the spatial sampling to the system under investigation [11]. While systems described in the last paragraphs themselves define their nodes and with them

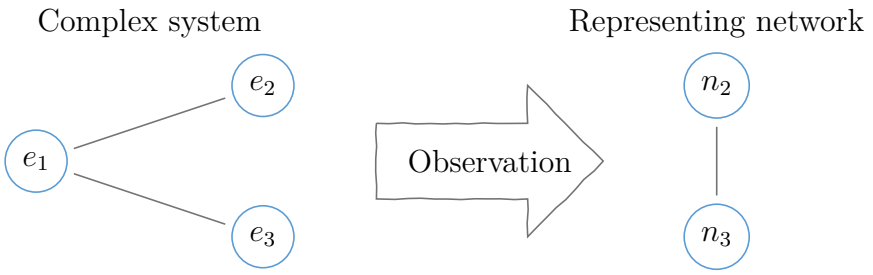

Figure 2.1.: Defining nodes by measurements sites. In case the entity e_1 is not observed, no node for e_1 is introduced in the associated network. Since e_1 influences e_2 and e_3, a direct link between n_2 and n_3 must be concluded in the network, in contrast to the true connectivity.

the number and positions of recording sites, here the opposite is true: network nodes are identified with measurement sites. In consequence, three situations may arise.

Firstly, the spatial sampling chosen is too wide-meshed, such that individual entities of the system, and therefore nodes in the network, are missed. A missing entity which influences two or more other entities creates spurious links in the representing network, as shown in Fig. 2.1. If e_1 is unobserved, no node n_1 is introduced in the corresponding network. The influence of e_1 onto e_2 and e_3 can only be explained by a spurious link directly connecting n_2 and n_3. In some situations, entities, even though they are unobserved, can be identified. These approaches are naturally limited, however. An overview can be found in [28, 61]

Secondly, if the spatial sampling it too close-meshed, two or more sensors might record from the same entity leading to a cluster of two or more highly connected nodes. This scenario is investigated in [11], where also the effect on the classification of the network is discussed.

Thirdly, the spatial sampling is ideal such that the sampling does not cause spurious links.

When recording from an unknown complex system attention must be paid to which extent the spatial sampling defines the corresponding network. Once the nodes are defined, links remain to be identified.

2.2. Bi- and multivariate interdependence measures

While it is important to remember the possible impact of the spatial sampling, this thesis assumes nodes as given. The emphasis is placed on the inference of links from recordings of the nodes. The connectivity of two nodes is established by an interdependence measure which is applied to recordings of the dynamics of the nodes. Interdependence measures are bi- or multivariate in nature.

In this section, the Pearson correlation coefficient and its multivariate counterpart, the partial correlation, is introduced [62]. The discussion of the partial correlation

will demonstrate a generic strategy on how to extend a bivariate measure into the multivariate domain.

Both measures operate on the first two central moments of a random vector. Thus, they can be applied to every random vector from any distribution with existing first and second moment. Since the multivariate normal distribution is the only distribution determined by the first two moments, clearly, this is the distribution both measures are designed for.

2.2.1. The multivariate normal distribution

The multivariate normal distribution is the generalization of the normal distribution to $k \geq 2$ dimensions. It has the probability density function

$$f_{\boldsymbol{X}}(\boldsymbol{x}) = \frac{1}{\sqrt{(2\pi)^k \, |\boldsymbol{\Sigma}|}} \exp\left(-\frac{1}{2}(\boldsymbol{x}-\boldsymbol{\mu})^{\mathrm{T}}\boldsymbol{\Sigma}^{-1}(\boldsymbol{x}-\boldsymbol{\mu})\right) , \tag{2.1}$$

with $\boldsymbol{\mu}$ the k-dimensional mean vector, $\boldsymbol{\Sigma}$ the $k \times k$-dimensional covariance matrix, and $|\cdot|$ the determinant of a matrix. For $k = 2$, Eq. (2.1) describes the bivariate normal distribution. For the density to exist, $\boldsymbol{\Sigma}$ must be positive definite. A multivariate normally distributed random variable is denoted $\boldsymbol{X} \sim \mathcal{N}(\boldsymbol{\mu}, \boldsymbol{\Sigma})$. Let $\boldsymbol{\epsilon} \sim \mathcal{N}(\boldsymbol{0}, \boldsymbol{I})$, and $\boldsymbol{T}$ such that $\boldsymbol{\Sigma} = \boldsymbol{T}\boldsymbol{T}^{\mathrm{T}}$, then

$$\boldsymbol{X} = \boldsymbol{T}\boldsymbol{\epsilon} + \boldsymbol{\mu} \tag{2.2}$$

is a random vector with density as given by Eq. (2.1) [63]. From $\boldsymbol{\Sigma}$, $\boldsymbol{T}$ can be obtained by the Cholesky decomposition, for which $\boldsymbol{T}$ can be chosen as a lower triangular matrix. It is then denoted $\boldsymbol{T}_{\mathrm{c}}$. Samples from $\boldsymbol{X}$ are drawn by transforming samples of $\boldsymbol{\epsilon}$ according to Eq. (2.2).

2.2.2. Construction of the multivariate normal distribution for a system of interest

In order to analyze the correlation and partial correlation with respect to a system of interest S, the multivariate normal distribution arising from S must be found. In particular, the covariance $\boldsymbol{\Sigma}$ of the distribution must conform to the topology of S. To this end, its topology is translated in a directed network with weighted adjacency matrix $\breve{\boldsymbol{A}}$. The network is directed since the interactions in a physical system are necessarily causal.

In case the topology of S is without loops, no circular dependency among variables exists, such that variables are naturally ordered. Taking the loop-free system shown in Fig. 2.2 (a) as an example, the system of linear equations

$$X_1 = \epsilon_1 \,, \qquad X_2 = aX_1 + \epsilon_2 \,, \qquad X_3 = bX_2 + \epsilon_3 \,, \qquad X_4 = cX_3 + \epsilon_4 \,, \tag{2.3}$$

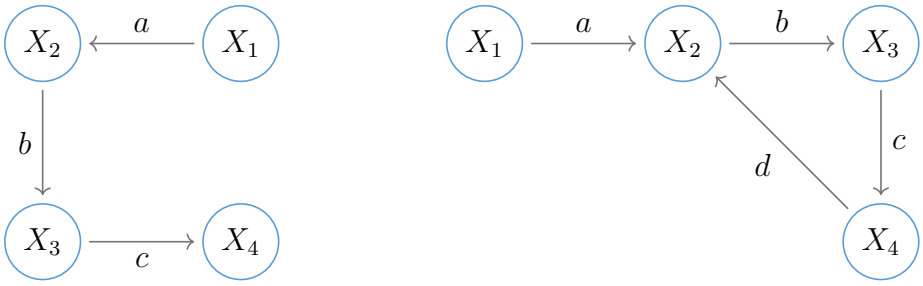

(a) Loop-free chain (b) Mesh with a loop

Figure 2.2.: Topologies of physical systems for which the transformation matrix $\boldsymbol{T}$ is to be found. A loop-free topology (a) induces a natural ordering of nodes. With the occurrence of loops, (b), the ordering is lost.

describing it is readily found. It is $\epsilon_i \sim \mathcal{N}(\mu_i, \sigma_i^2), i = 1, \ldots, 4$. In Fig. 2.2 (b), an exemplary network with one loop is shown. Its weighted adjacency matrix is

$$\breve{\boldsymbol{A}} = \begin{pmatrix} 0 & 0 & 0 & 0 \\ a & 0 & 0 & d \\ 0 & b & 0 & 0 \\ 0 & 0 & c & 0 \end{pmatrix}, \quad a, b, c, d \in \mathbb{R}\,. \tag{2.4}$$

Since loops break the ordering of variables, the equivalent of Eq. (2.3) takes the form

$$\boldsymbol{X} = \breve{\boldsymbol{A}}\boldsymbol{X} + \boldsymbol{\epsilon} + (\boldsymbol{I} - \breve{\boldsymbol{A}})\boldsymbol{\mu}\,. \tag{2.5}$$

Solving for $\boldsymbol{X}$ yields

$$\boldsymbol{X} = (\boldsymbol{I} - \breve{\boldsymbol{A}})^{-1}[\boldsymbol{\epsilon} + (\boldsymbol{I} - \breve{\boldsymbol{A}})\boldsymbol{\mu}] = \boldsymbol{T}\boldsymbol{\epsilon} + \boldsymbol{\mu}\,, \quad \text{with} \tag{2.6}$$

$$\boldsymbol{T} = (\boldsymbol{I} - \breve{\boldsymbol{A}})^{-1}\,, \quad \text{such that} \tag{2.7}$$

$$\boldsymbol{T}\boldsymbol{T}^{\mathrm{T}} = \boldsymbol{\Sigma}\,. \tag{2.8}$$

Uniqueness of $\boldsymbol{T}$ By retaining $\boldsymbol{\Sigma}$, Eq. (2.8) can be generalized to

$$\boldsymbol{\Sigma} = \boldsymbol{T}\boldsymbol{E}(\boldsymbol{T}\boldsymbol{E})^{\mathrm{T}} = \boldsymbol{T}_{\mathrm{e}}\boldsymbol{T}_{\mathrm{e}}{}^{\mathrm{T}} \tag{2.9}$$

if $\boldsymbol{E}\boldsymbol{E}^{\mathrm{T}} = \boldsymbol{I}$ holds. This determines $\boldsymbol{E}$ as the identity matrix but with the additional freedom to choose the sign of the diagonal entries. It follows from Eqs. (2.8) and (2.9) that the two systems defined by

$$\begin{aligned} \breve{\boldsymbol{A}} = -\boldsymbol{T}^{-1} + \boldsymbol{I}\,, \quad \text{and} \quad \breve{\boldsymbol{A}}_{\mathrm{e}} &= -\boldsymbol{T}_{\mathrm{e}}{}^{-1} + \boldsymbol{I}\,, \\ &= -\boldsymbol{E}\boldsymbol{T}^{-1} + \boldsymbol{I}\,, \end{aligned} \tag{2.10}$$

respectively, lead to the same covariance matrix $\boldsymbol{\Sigma}$. Concerning links among different nodes, $\boldsymbol{E}$ only influences the sign of the entries of $\boldsymbol{T}^{-1}$, such that the systems $\breve{\boldsymbol{A}}$ and

$\breve{\boldsymbol{A}}_\mathrm{e}$ are topologically equivalent, but the sign of connections might differ. While the diagonal of $\breve{\boldsymbol{A}}$ is zero, this in not necessarily true for $\breve{\boldsymbol{A}}_\mathrm{e}$. In case the diagonal element of $(T^{-1})_{ii}$, $i \in [1,k] \subset \mathbb{N}$ changes on multiplying $\boldsymbol{T}^{-1}$ with $\boldsymbol{E}$, $(\breve{A}_\mathrm{e})_{ii} = 2$ follows.

For the same covariance matrix $\boldsymbol{\Sigma}$, also a topologically different system $\breve{\boldsymbol{A}}_\mathrm{c}$ can be constructed using the Cholesky decomposition. If $\breve{\boldsymbol{A}}$ is a strictly lower triangular matrix, $\boldsymbol{T}$ must be lower triangular, but in general, $\boldsymbol{T}$ is fully occupied. Since $\boldsymbol{\Sigma}$ is symmetric and positive definite, a lower triangular matrix $\boldsymbol{T}_\mathrm{c}$ can be obtained as the Cholesky decomposition of $\boldsymbol{\Sigma}$. Consequently, both $\boldsymbol{T}$ and $\boldsymbol{T}_\mathrm{c}$ lead to the same covariance matrix. It transpires that there are also two matrices $\breve{\boldsymbol{A}}$ and $\breve{\boldsymbol{A}}_\mathrm{c}$ defining two different topologies with the same $\boldsymbol{\Sigma}$. The matrix $\breve{\boldsymbol{A}}_\mathrm{c}$ is guaranteed to be lower triangular, but its diagonal, in general, is nonzero. Thus, both systems $\breve{\boldsymbol{A}}_\mathrm{e}$ and $\breve{\boldsymbol{A}}_\mathrm{c}$ can include self-loops. The systems $\breve{\boldsymbol{A}}$, $\breve{\boldsymbol{A}}_\mathrm{e}$, and $\breve{\boldsymbol{A}}_\mathrm{c}$ are inherently indistinguishable by correlation analysis.

2.2.3. Bivariate measures

A bivariate measure for the dependency of two random variables X and Y is the *covariance*

$$\mathrm{cov}(X,Y) = \mathrm{E}\left\{[X - \mathrm{E}(X)]\,[Y - \mathrm{E}(Y)]\right\}\,, \tag{2.11}$$

where $\mathrm{E}(\cdot)$ denotes the expected value. The *Pearson correlation coefficient*

$$\varrho_{XY} = \frac{\mathrm{cov}(X,Y)}{\sqrt{\mathrm{var}(X)\,\mathrm{var}(Y)}}\,, \tag{2.12}$$

is the dimensionless, normalized version of the covariance.

Bivariate measures operate on two variables, here X and Y. Other variables possibly affecting X and Y are not taken into account when investigating their dependency.

2.2.4. Limitations of bivariate measures

Consider the loop-free network depicted in Fig. 2.2 (a). The pairwise correlation is nonzero between all components of $\boldsymbol{X} = (X_1, X_2, X_3, X_4)$. It is the gist of the following Sec. 2.3 to show that this result is independent of the specific bivariate measure used. Consequently, all bivariate measures fail in reconstructing the connectivity structure of a complex system. For $a = -c = 0.57$ and $b = 1.35$, the correlation coefficients of $\boldsymbol{X}$ are displayed in Fig. 2.3 (a). Dashed lines indicate that correlation coefficients of unconnected nodes are nonzero, such that link are suggested even though they do not exist in the underlying system.

2.2.5. Direct and indirect links

It follows from the previous section that direct and indirect links need to be conceptually distinguished. *Direct* links have a representation in the physical world, *indirect* links

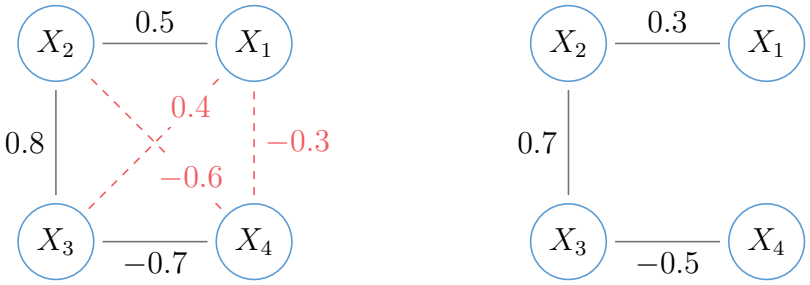

(a) Bivariate result (b) Multivariate result

Figure 2.3.: Correlation and partial correlation analysis of realizations of Eq. (2.3). For $a = -c = 0.57$ and $b = 1.35$, realizations from Eq. (2.3) are drawn and analyzed both with the correlation and partial correlation coefficient. Correlation analysis yields the fully connected network shown in (a). Direct links (black) as well as indirect links (red, dashed) are reported. In contrast, partial correlation analysis, (b), reveals direct connections only.

do not and are thus spurious. Taking the network shown in Fig. 2.3 (a) as an example, black lines indicate direct, while the red lines indicate indirect links. An indirect link occurs whenever

1. no path of length one, but at least one path of length larger than one connects two variables, and

2. the dependency measure cannot make use of the full information of the variables along these paths.

All pairs of variables for which both conditions are fulfilled are connected by an indirect link. The major drawback of bivariate measures applied to establish network links is thus that indirect links are induced.

2.2.6. Multivariate measures

Multivariate measures are designed to overcome this limitation. Let $\boldsymbol{Z} = (\boldsymbol{X}^{\mathrm{T}}, \boldsymbol{Y}^{\mathrm{T}})^{\mathrm{T}}$ be an $(u+v)$-dimensional random vector partitioned in the two u- and v-dimensional random vectors $\boldsymbol{X}$ and $\boldsymbol{Y}$. A multivariate analysis of the relation withing $\boldsymbol{Y}$ takes into account all information provided by $\boldsymbol{X}$. The generic pattern to extend a bivariate measure to the multivariate domain is to apply the respective bivariate measure to the residuals $\boldsymbol{\varepsilon_Y}$ obtained from regressing $\boldsymbol{Y}$ on $\boldsymbol{X}$. This procedure is called *partialization*. If $\boldsymbol{Y}$ is of dimension two and $\boldsymbol{\varepsilon_Y}$ is statistically independent of $\boldsymbol{X}$, the multivariate measure is nonzero between actually linked variables only.* An example network constructed by the partial correlation is given in Fig. 2.3 (b).

*The marrying of parents with a joint child is an exception. It is discussed in Sec. 2.3.3.

The partial correlation

The multivariate counterpart of the Pearson correlation coefficient is the *partial correlation*. The regression model used is linear both in its parameters and its variables.

The best linear predictor Let $\boldsymbol{X}$, $\boldsymbol{Y}$, and $\boldsymbol{Z}$ be as above. The mean

$$\boldsymbol{\mu_Z} = \begin{pmatrix} \boldsymbol{\mu_X} \\ \boldsymbol{\mu_Y} \end{pmatrix} \tag{2.13}$$

and covariance

$$\boldsymbol{\Sigma_{ZZ}} = \begin{pmatrix} \boldsymbol{\Sigma_{XX}} & \boldsymbol{\Sigma_{XY}} \\ \boldsymbol{\Sigma_{YX}} & \boldsymbol{\Sigma_{YY}} \end{pmatrix} \tag{2.14}$$

of $\boldsymbol{Z}$ also partition into subsystems [62]. The partialization of $\boldsymbol{Y}$ with respect to $\boldsymbol{X}$ is based on the linear regression model

$$\boldsymbol{Y} = \boldsymbol{a} + \boldsymbol{b}\boldsymbol{X} + \boldsymbol{\epsilon}\,. \tag{2.15}$$

Its parameters are determined by minimizing

$$\mathrm{E}\left[(\boldsymbol{Y} - \boldsymbol{a} - \boldsymbol{b}\boldsymbol{X})(\boldsymbol{Y} - \boldsymbol{a} - \boldsymbol{b}\boldsymbol{X})^{\mathrm{T}}\right]\,. \tag{2.16}$$

The minimum $\boldsymbol{\Sigma_{YY}} - \boldsymbol{\Sigma_{YX}}\boldsymbol{\Sigma_{XX}^{-1}}\boldsymbol{\Sigma_{XY}}$ is attained for the v-vector

$$\boldsymbol{a} = \boldsymbol{\mu_Y} - \boldsymbol{\Sigma_{YX}}\boldsymbol{\Sigma_{XX}^{-1}}\boldsymbol{\mu_X} \tag{2.17}$$

and the $v \times u$ matrix of regression coefficients

$$\boldsymbol{b} = \boldsymbol{\Sigma_{YX}}\boldsymbol{\Sigma_{XX}^{-1}}\,, \tag{2.18}$$

where $\boldsymbol{\Sigma_{XY}} = \boldsymbol{\Sigma_{YX}^{\mathrm{T}}}$ [62]. Consequently, the *best linear predictor* of $\boldsymbol{Y}$ given $\boldsymbol{X}$ is defined [62, 64]

$$\mathrm{E}(\boldsymbol{Y} \mid \boldsymbol{X}) = \boldsymbol{\mu_Y} + \boldsymbol{\Sigma_{YX}}\boldsymbol{\Sigma_{XX}^{-1}}(\boldsymbol{X} - \boldsymbol{\mu_X})\,. \tag{2.19}$$

Partial covariance of $\boldsymbol{Y}$ given $\boldsymbol{X}$ The difference

$$\begin{aligned} \boldsymbol{\varepsilon_Y} &= \boldsymbol{Y} - \mathrm{E}(\boldsymbol{Y} \mid \boldsymbol{X}) \\ &= \boldsymbol{Y} - \boldsymbol{\mu_Y} - \boldsymbol{\Sigma_{YX}}\boldsymbol{\Sigma_{XX}^{-1}}(\boldsymbol{X} - \boldsymbol{\mu_X}) \end{aligned} \tag{2.20}$$

is the residual of $\boldsymbol{Y}$ after the linear influence of $\boldsymbol{X}$ is removed. The covariance of $\boldsymbol{\varepsilon_Y}$

$$\boldsymbol{\Sigma_{\varepsilon_Y \varepsilon_Y}} = \boldsymbol{\Sigma_{YY}} - \boldsymbol{\Sigma_{YX}}\boldsymbol{\Sigma_{XX}^{-1}}\boldsymbol{\Sigma_{XY}} \tag{2.21}$$

constitutes the *partial covariance matrix* of $\boldsymbol{Y}$ given $\boldsymbol{X}$ [62]. The diagonal of $\boldsymbol{\Sigma_{\varepsilon_Y \varepsilon_Y}}$ contains the *partial variance* of $\boldsymbol{Y}$. The off-diagonal entries characterizing the interaction structure within $\boldsymbol{Y}$ after removal of the linear information contained in $\boldsymbol{X}$ by the *partial covariance* of $\boldsymbol{Y}$.

Partial correlation of $\boldsymbol{Y}$ given $\boldsymbol{X}$ The partial correlation matrix

$$\boldsymbol{\pi_{YY}} = \boldsymbol{s} \cdot \boldsymbol{\Sigma}_{\boldsymbol{\varepsilon_Y \varepsilon_Y}} \cdot \boldsymbol{s}\,, \quad \boldsymbol{s}_{ii} = (\boldsymbol{\Sigma}_{\boldsymbol{\varepsilon_Y \varepsilon_Y}})_{ii}^{-1/2}\,, \quad \boldsymbol{s}_{ij} = 0 : i \neq j\,, \quad i,j = 1,\ldots,v \tag{2.22}$$

is the normalized partial covariance matrix, Eq. (2.21) [62].

2.2.7. Partialization as a matrix operation

The partial correlation for partitions with $v = 2$ is of particular interest since only than the dependency between the two variables of $\boldsymbol{Y}$ is assessed with respect to the information of the entire system. To obtain all such partitions, the best linear predictor has to be calculated for each partition, separately. Fortunately, the pairwise partial correlation matrix $\boldsymbol{\pi}$ relates to the normalized inverse of the correlation matrix $\boldsymbol{\varrho}$ [65–67]

$$\tilde{\boldsymbol{\pi}} = \boldsymbol{s} \cdot \boldsymbol{u} \cdot \boldsymbol{s}\,, \quad \boldsymbol{s}_{ii} = \boldsymbol{u}_{ii}^{-1/2}\,, \quad \boldsymbol{s}_{ij} = 0 : i \neq j\,, \quad i,j = 1,\ldots,u+v\,. \tag{2.23}$$

with

$$\boldsymbol{u} = \boldsymbol{\varrho}^{-1} \tag{2.24}$$

by

$$\boldsymbol{\pi} = 2\boldsymbol{I} - \tilde{\boldsymbol{\pi}}\,. \tag{2.25}$$

The proof of Eq. (2.25) [67] can also be found in App. A.5.

For theoretical considerations, this approach is convenient. In application however, the numerical inversion of an ill conditioned matrix can easily fail. Therefore, at least for larger systems, more robust results are expected by directly relying on the best linear predictor.

2.3. Emergence of indirect links

As explained in Sec. 2.2.5, bivariate measures provoke indirect links. In this section, the complete picture of the emergence of such links is rigorously analyzed. It becomes evident that any bivariate measure which is based on partialization causes indirect links, not only the correlation coefficient.

By reversing the steps of partialization for $v = 2$ as discussed in Sec. 2.2.7, the covariance matrix

$$\boldsymbol{\Sigma} = (2\boldsymbol{I} - \boldsymbol{\pi})^{-1} \tag{2.26}$$

is calculated from the partial correlation matrix. The inverse is guaranteed to exist since $2\boldsymbol{I} - \boldsymbol{\pi} \overset{2.25}{=} \tilde{\boldsymbol{\pi}} \overset{2.23}{=} \boldsymbol{sus}$, and $\boldsymbol{s}$ and $\boldsymbol{u}$ are both invertible. In case the absolute value of the largest eigenvalue of $2\boldsymbol{I} - \boldsymbol{\pi}$ is smaller than one, the matrix inversion can be expanded in a Taylor series. This allows to analyze the emergence of indirect links in great detail.

Taylor expansion of the covariance matrix The matrix of any normalized measure, e.g., the partial correlation matrix, can be written as

$$\boldsymbol{\pi} = \boldsymbol{I} + \boldsymbol{P}\,. \tag{2.27}$$

In order to reverse the steps of partialization, first the off-diagonal entries of $\boldsymbol{\pi}$ have to be multiplied by -1, yielding

$$\breve{\boldsymbol{\pi}} = \boldsymbol{I} - \boldsymbol{P}\,. \tag{2.28}$$

The inverse of $\breve{\boldsymbol{\pi}}$ is a covariance matrix $\boldsymbol{\Sigma}$ of the system described by $\boldsymbol{\pi}$. Key to the insight in the emergence of indirect links is the Taylor expansion of

$$\boldsymbol{\Sigma} = \breve{\boldsymbol{\pi}}^{-1} = f(\boldsymbol{P}) = (\boldsymbol{I} - \boldsymbol{P})^{-1} \tag{2.29}$$

about $\boldsymbol{P}_0 = \boldsymbol{0}$ which is the geometric series

$$\boldsymbol{\Sigma} = Tf(\boldsymbol{P}, \boldsymbol{P}_0) = \boldsymbol{I} + \sum_{q=1}^{\infty} \boldsymbol{P}^q\,, \quad [\rightarrow \text{App. A.6}]. \tag{2.30}$$

Links emerge from powers of $\boldsymbol{P}$. The first order approximation

$$T_1 f(\boldsymbol{P}, \boldsymbol{P}_0) = \boldsymbol{I} + \boldsymbol{P}\,, \tag{2.31}$$

comes with already normalized diagonal, such that in first order $\boldsymbol{\Sigma}$ coincides with the partial correlation matrix $\boldsymbol{\pi}$, cf., Eq. (2.27). Indirect links start to emerge with the second order of $Tf(\boldsymbol{P}, \boldsymbol{P}_0)$. This allows to infer some properties of indirect links.

1. In general, powers of $\boldsymbol{P}$ contribute nonzero values to all entries of $\boldsymbol{\Sigma}$ leading to a fully connected network.
2. The normalization of $\boldsymbol{\Sigma}$ in order to obtain $\boldsymbol{\varrho}$ alters the values of direct links.
3. For a network with coinciding correlation and partial correlation, $\boldsymbol{P}$ must be nilpotent of degree 2 [$\rightarrow$ Eq. (2.30)]. With $\boldsymbol{P}$ symmetric, this is only possible for $\boldsymbol{P} = \boldsymbol{0}$. Thus, only networks without any links are correctly reconstructed by a bivariate interdependence measure.

2.3.1. Correlation coefficient of indirect links

As shown in the previous section, bivariate measures inevitably provoke indirect links. For any partial correlation matrix $\boldsymbol{\pi}$, Eq. (2.26) specifies the corresponding bivariate covariance matrix $\boldsymbol{\Sigma}$. Now, consider the special case of the three-node chain which translates to

$$\boldsymbol{A} = \begin{pmatrix} 0 & 0 & 0 \\ a & 0 & 0 \\ 0 & b & 0 \end{pmatrix}, \quad \boldsymbol{T} = \begin{pmatrix} 1 & 0 & 0 \\ a & 1 & 0 \\ ab & b & 1 \end{pmatrix}, \text{ and network } \tag{2.32}$$

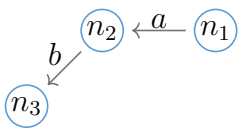

.

The special interest in this situation arises from the fact that the chain transforms into a triangle by adding a single indirect link between n_1 and n_3. The relative number of triangles in a network is considered a distinctive characteristic quantified by the clustering coefficient. The emergence of artificial triangles is expected if the correlation coefficient of the indirect link attains values comparable to the correlation coefficient of direct links. The artificial increase of triangles may cause false conclusion upon the class of the underlying network.

Proposition 2.3.1 (Correlation coefficient of indirectly linked nodes, isolated case)**.** *In the three-node chain network, Eq.* (2.32)*, the correlation coefficients of the two pairs of directly linked nodes and the correlation coefficient of the indirectly linked node pair can attain comparable values.*

Proof. The covariance matrix of the three-node chain network is

$$\boldsymbol{T}\boldsymbol{T}^{\mathrm{T}} = \boldsymbol{\Sigma} = \begin{pmatrix} 1 & a & ab \\ a & a^2+1 & ba^2+b \\ ab & ba^2+b & a^2b^2+b^2+1 \end{pmatrix}, \tag{2.33}$$

leading to the correlation matrix

$$\boldsymbol{\varrho} = \begin{pmatrix} 1 & \frac{a}{\sqrt{\alpha}} & \frac{ab}{\sqrt{\alpha\beta-a^2}} \\ \frac{a}{\sqrt{\alpha}} & 1 & \frac{b\sqrt{\alpha}}{\sqrt{\alpha\beta-a^2}} \\ \frac{ab}{\sqrt{\alpha\beta-a^2}} & \frac{b\sqrt{\alpha}}{\sqrt{\alpha\beta-a^2}} & 1 \end{pmatrix}, \quad \alpha = 1+a^2,\ \beta = 1+b^2\,. \tag{2.34}$$

In particular, the correlation coefficient characterizing the indirect link reads

$$\varrho_{31} = \frac{ab}{\sqrt{(1+a^2)(1+b^2)-a^2}} \tag{2.35}$$

$$= \frac{ab}{\sqrt{1+b^2(1+a^2)}}\,. \tag{2.36}$$

In case $b^2(1+a^2) \ll 1$, ϱ_{31} is approximately ab. For $b^2(1+a^2) \gg 1$

$$\begin{aligned} \varrho_{31} &\approx \frac{ab}{b\sqrt{1+a^2}} \\ &\approx \begin{cases} a & \text{for } a^2 \ll 1\,, \\ 1 & \text{for } a^2 \gg 1\,. \end{cases} \end{aligned} \tag{2.37}$$

Likewise, the relative strengths of the indirect link compared to the two direct ones

$$\frac{\varrho_{21}}{\varrho_{31}} = \frac{1}{b}\sqrt{b^2+1-\frac{a^2}{1+a^2}}\,, \tag{2.38}$$

$$\frac{\varrho_{32}}{\varrho_{31}} = \frac{\sqrt{\alpha}}{a} = \sqrt{1+\frac{1}{a^2}}\,, \tag{2.39}$$

also approximate one for $a \gg 1$ and $b \neq 0$. Equations (2.35) – (2.39) show that the correlation coefficient of the indirect link in a three-node chain can reach a value comparable to the ones of the direct links. □

This is the theoretical explanation for the so-called transitivity property of bivariate measures [21, 68], and it follows that in general, a correlation analysis fails at distinguishing direct and indirect links.

The above derivation is based on an isolated three-node chain. If embedded in a larger network, other nodes connected to the chain also influence the correlation coefficients. This influence is characterized by the following proposition.

Proposition 2.3.2 (Correlation coefficient of indirectly linked nodes, embedded case)**.** *Connecting an additional node n_0 to the head of the isolated three-node chain [→ Eq. (2.32)] with linkage parameter z, Eq. (2.41), yields*

$$\varrho_{31}^{z} = \varrho_{31} \cdot \sqrt{\frac{1+z^2}{1+z^2\varrho_{31}^2}}\,, \tag{2.40}$$

as the correlation coefficient of the indirect link. The superscript z indicates the presence of n_0.

Proof. The four-node chain subject to this proposition translates to

$$\boldsymbol{A} = \begin{pmatrix} 0 & 0 & 0 & 0 \\ z & 0 & 0 & 0 \\ 0 & a & 0 & 0 \\ 0 & 0 & b & 0 \end{pmatrix}, \quad \boldsymbol{T} = \begin{pmatrix} 1 & 0 & 0 & 0 \\ z & 1 & 0 & 0 \\ za & a & 1 & 0 \\ zab & ab & b & 1 \end{pmatrix}, \quad \text{with } n_2 \xleftarrow{a} n_1,\ n_2 \xrightarrow{b} n_3,\ n_1 \xrightarrow{z} n_0\,. \tag{2.41}$$

Let n_1 to n_3 constitute the three-node chain of Prop. 2.3.1, and n_0 the additional node linked to n_1 by parameter z. In analogy to Eq. (2.36), the correlation coefficient of the indirect link between n_1 and n_3 is now

$$\varrho_{31}^{z} = \frac{ab\sqrt{1+z^2}}{\sqrt{1+b^2+(ab)^2+(zab)^2}}\,. \tag{2.42}$$

Equation (2.42) can be rewritten as

$$\begin{aligned} \varrho_{31}^{z} &= \frac{ab}{\sqrt{1+b^2+(ab)^2}} \cdot \frac{\sqrt{1+b^2+(ab)^2}}{\sqrt{1+b^2+(ab)^2+(zab)^2}} \cdot \sqrt{1+z^2} \\ &= \varrho_{31} \cdot \sqrt{\frac{1}{1+\frac{(zab)^2}{1+b^2+(ab)^2}}} \cdot \sqrt{1+z^2} \\ &= \varrho_{31} \cdot \sqrt{\frac{1}{1+z^2\varrho_{31}^2}} \cdot \sqrt{1+z^2} \\ &= \varrho_{31} \cdot \sqrt{\frac{1+z^2}{1+z^2\varrho_{31}^2}}\,, \end{aligned} \tag{2.43}$$

which proofs the proposition. □

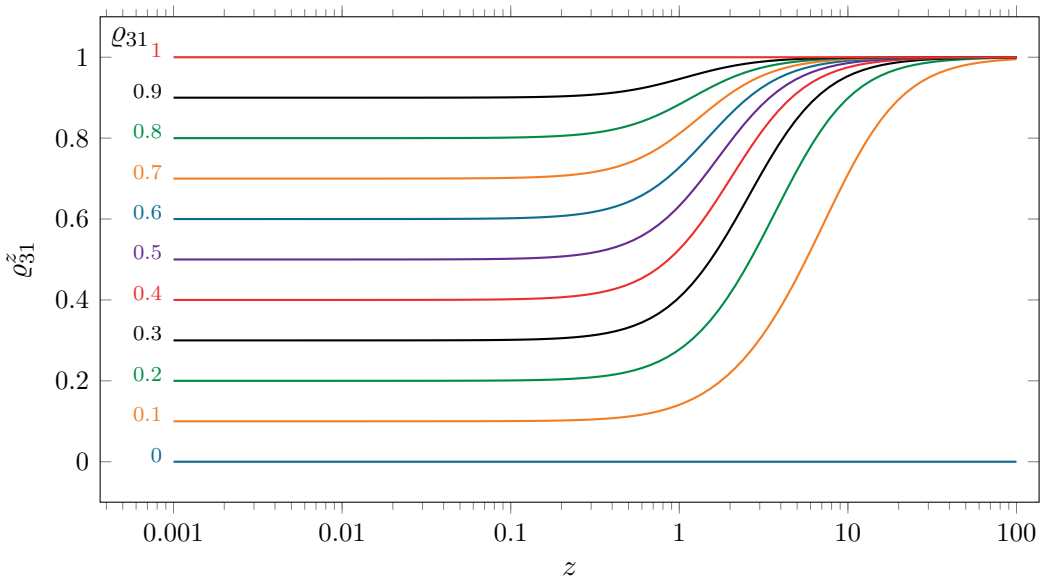

Figure 2.4.: Correlation coefficient ϱ_{31}^z of the indirect link discussed in Prop. 2.3.2. As ϱ_{31}^z is expressed in terms of ϱ_{31}, cf., Eq. (2.40), $z = 0$ equals the value of ϱ_{31} which is given in front of each line. For $z < 1$, ϱ_{31}^z is virtually independent of z. With $z > 1$, the impact of n_0 increases such that ϱ_{31}^z eventually reaches one for all $\varrho_{31} \neq 0$.

Based on Prop. 2.3.1 and 2.3.2, the influence of the extra node n_0 onto the correlation coefficient of the indirect link is now discussed. In Fig. 2.4, the graph of Eq. (2.40) is shown where different values of ϱ_{31} are color coded. Since ϱ_{31}^z is expressed in terms of ϱ_{31}, Fig. 2.4 shows ϱ_{31} at $z = 0$. The graph is shown for positive values of z only to allow the x-axis to be logarithmically scaled. The negative branch of z is the reflection of the positive across the y-axis since ϱ_{31}^z is symmetric in z. It is observed that ϱ_{31}^z is virtually independent of z for $z < 1$. For $z > 1$, ϱ_{31}^z increases and eventually reaches its maximum which is one for all values of $\varrho_{31} > 0$.

With $\varrho_{31} \in [-1, 1] \subset \mathbb{R}$ and $z \in \mathbb{R}$, ϱ_{31} and z are not directly comparable. More insight gives the investigation of ϱ_{31}^z with regard to a, b, and z. To this end, assume that all connections in the network are approximately of equal strength, translating to $a = b = z$. In this case, ϱ_{31} and ϱ_{31}^z are functions of a single variable, say a, shown in Fig. 2.5 (a). For $|a| \ll 1$ and $|a| \gg 1$, both functions yield approximately equal values. Their largest relative difference is located at $a = \pm 1$, where they differ by the factor $\sqrt{3/2}$, cf., Fig. 2.5 (b). It follows that in a network in which connection strengths are reasonably balanced, the two direct links closest to the indirect one mainly determine its strength. This finding extends the applicability of Prop. 2.3.1 to three-node chains embedded in a larger network.

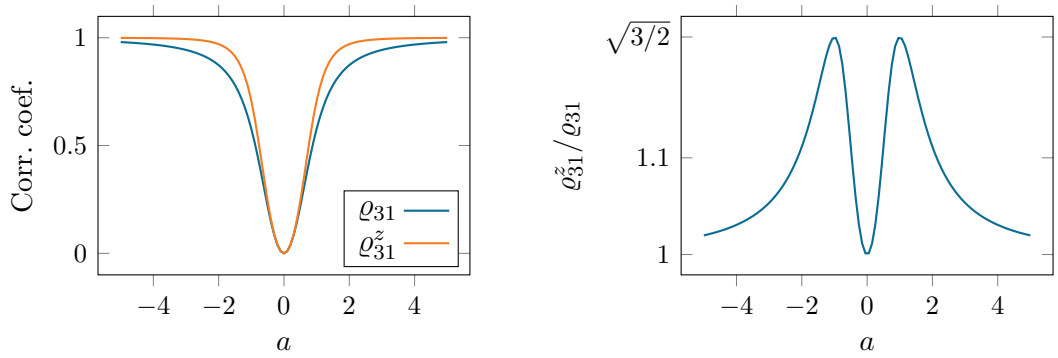

(a) ϱ_{31} and ϱ_{31}^z (b) $\varrho_{31}^z/\varrho_{31}$

Figure 2.5.: Comparison of the correlation coefficient of the indirect link in an isolated and an embedded three-node chain. For $a = b = z$, in (a) the graphs of ϱ_{31} and ϱ_{31}^z are shown in blue and orange, respectively. Their ratio is shown in (b). At $a = \pm 1$, the two functions exhibit their largest relative difference which is $\varrho_{31}^z = \sqrt{3/2} \cdot \varrho_{31}$.

2.3.2. Partialization in the non-linear domain

A non-linear, non-parametric extension of the linear regression is the generalized additive model. In this model, Eq. (2.19) is replaced by [69]

$$\mathrm{E}(Y \mid \boldsymbol{X}) = s_0 + \sum_{i=1}^{k} s_i(X_i)\,. \tag{2.44}$$

Each s_i is a smooth function mapping the realizations of X_i to Y. The approach is non-parametric as it is unnecessary to specify the functional form of s_i. Instead, s_i is estimated by smoothing the scatter plot of realizations of X_i and Y. The estimation of the s_i is carried out one after the other [69]. Transferring this approach for the conditional expected value over to the partial correlation, the two residual time series

$$\epsilon_{Y_i} = Y_i - \mathrm{E}(Y_i \mid \boldsymbol{X}), \quad i = 1, 2 \tag{2.45}$$

are now calculated using Eq. (2.44). In theory, this allows for a non-linear version of the partial correlation

$$\pi = \mathrm{corr}(\epsilon_{Y_1}, \epsilon_{Y_2})\,. \tag{2.46}$$

In application, however, results of Eq. (2.46) are unreliable. The estimated functions $s_i(X_i)$ allow for oscillations. The time scale of these oscillations is defined by the number of realizations from which s_i is estimated. This structure is thus common to all s_i and is reflected in the residuals. This results in the tendency to spurious correlations. In consequence, partialization cannot be trivially carried over to the non-linear domain.

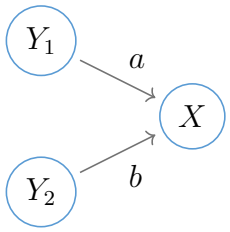

Figure 2.6.: Smallest network not satisfying the Wermuth condition.

2.3.3. Moral networks

As briefly mentioned in Sec. 2.2.6, partial correlation leads to indirect links in one specific situation. This situation is discussed in this section.

Partial correlation analysis turns the directed network of the underlying system in an undirected one. Thereby, a link between two nodes is only included in the network if it can be admitted given the information of all remaining nodes. There is one exception. Assume the directed network in Fig. 2.6: Y_1 and Y_2 are unconnected and have zero covariance, but they have a *common child* X, to which both have a nonzero covariance. A directed network is called *Wermuth* if it contains no subnetwork with this configuration [70]. In the undirected conditional independence network defined by the partial correlation, Y_2 and Y_1 have partial covariance $(-ab)$, even though Y_1 and Y_2 are independent. The joint child X marries its parents Y_1 and Y_2 in the conditional independence network. Therefore, such networks are called *moral* networks [71]. In conclusion, partial correlation analysis reports the moral network associated with the system under investigation. For a directed network, the corresponding moral network is constructed by joining unconnected parents of any joint child by an undirected link and transmuting all directed links into undirected links by simply neglecting their directional information [70].

2.4. Estimating links from data

Let the probability density function $f_X(x;\theta)$ of a random sample $\boldsymbol{X} = \{X_1, \ldots, X_m\}$ be parametrized by θ. Then, any function of $\boldsymbol{X}$

$$s(X_1, \ldots, X_m) =: T \tag{2.47}$$

is called a *statistic* [72]. The realization of the statistic

$$t = s(x_1, \ldots, x_m) \tag{2.48}$$

is a function of the realization of $\boldsymbol{X}$. If T is evaluated to infer the value of θ, T is called an *estimator*. The value t of T is then called an estimate of θ [73].

The *sample correlation coefficient*

$$r_{xy} = \frac{\sum_{i=1}^{m}(x_i - \bar{x})(y_i - \bar{y})}{\sqrt{\sum_{i=1}^{m}(x_i - \bar{x})^2 \sum_{i=1}^{m}(y_i - \bar{y})^2}} \tag{2.49}$$

is an estimate of the correlation coefficient of two random variables X and Y based on their realizations $\boldsymbol{x} = \{x_1, \ldots, x_m\}$ and $\boldsymbol{y} = \{y_1, \ldots, y_m\}$. It employs the sample mean

$$\bar{x} = \frac{1}{m} \sum_{i=1}^{m} x_i \,, \tag{2.50}$$

an estimate of the expected value. Sample correlation coefficient and sample mean are functions of x_i and y_i only and can thus be derived from observations of a system.

In case $\boldsymbol{x}$ is a k-variate set of realizations, i.e., a $k \times m$ matrix, of the random variable $\boldsymbol{X}$, an estimate of the covariance matrix of $\boldsymbol{X}$ is

$$\boldsymbol{Q} = \frac{1}{m-1} \sum_{i=1}^{m} (\boldsymbol{x}_i - \bar{\boldsymbol{x}_i})(\boldsymbol{x}_i - \bar{\boldsymbol{x}_i})^{\mathrm{T}} \,, \tag{2.51}$$

where $\boldsymbol{x}_i$ is the i-th column of $\boldsymbol{x}$. The sample correlation matrix is then

$$\boldsymbol{\mathcal{R}} = \boldsymbol{s} \cdot \boldsymbol{Q} \cdot \boldsymbol{s} \,, \quad \boldsymbol{s}_{ii} = \boldsymbol{Q}_{ii}^{-1/2} \,, \quad \boldsymbol{s}_{ij} = 0 : i \neq j \,, \quad i, j = 1, \ldots, k \,. \tag{2.52}$$

The partial correlation matrix is estimated by substituting $\boldsymbol{\mathcal{R}}$ for $\boldsymbol{\Sigma}$ in Eq. (2.21).

2.5. Quantification of links

In order to translate (partial) correlation coefficients into links, either a threshold is applied to the coefficients or hypothesis tests are performed. The discussion of both approaches assumes that the system under investigation induces a network with a single component. In case this assumption does not hold, the discussion applies to each component of the network, separately.

2.5.1. Link quantification by an arbitrary threshold

Thresholding the correlation coefficient might be considered a first approach to link quantification [11, 15, 23–26]. To this end, either a threshold can be defined directly, or the desired number of links in the network is fixed. The following example shows that both approaches fail in reconstructing the underlying connectivity.

The sample correlation matrix $\boldsymbol{\mathcal{R}}$ and the matrix $\boldsymbol{p}$ of p-values of the four-node-chain network presented in Fig. 2.2 (a) on p. 39 is

$$\boldsymbol{\mathcal{R}} = \begin{pmatrix} 1.00 & 0.47 & 0.40 & -0.02 \\ 0.47 & 1.00 & 0.81 & -0.13 \\ 0.40 & 0.81 & 1.00 & -0.17 \\ -0.02 & -0.13 & -0.17 & 1.00 \end{pmatrix} \,, \quad \boldsymbol{p} = \begin{pmatrix} 1.00 & 0.00 & 0.00 & 0.77 \\ 0.00 & 1.00 & 0.00 & 0.03 \\ 0.00 & 0.00 & 1.00 & 0.00 \\ 0.77 & 0.03 & 0.00 & 1.00 \end{pmatrix} \,. \tag{2.53}$$

By fixing the number of links to three as in the underlying network, the three largest correlation coefficients indicate the network depicted in Fig. 2.7. The physical

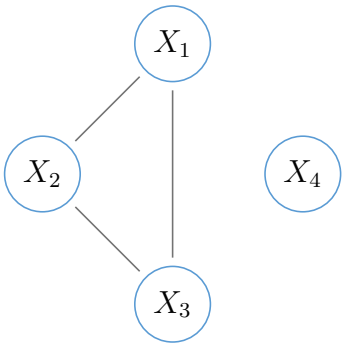

Figure 2.7.: Network reconstructed from realizations of Eq. (2.3) corresponding to Fig. 2.2 (a). Links are established by the three largest correlation coefficients given in Eq. (2.53). The reconstructed network does not correctly reflect the interaction structure of the system investigated.

connection between X_3 and X_4 is discarded in favor for the relatively strong indirect connection between X_1 and X_3. As a consequence, the wrong topology is reported in which an open triangle is closed as discussed in Sec. 2.3. This, in turn, artificially increases the average clustering coefficient to $C = 3/4$ while in the true network it is $C = 0$. The same results for a threshold at 0.4 applied to $\boldsymbol{\mathcal{R}}$ directly such that $|\mathcal{R}_{ij}| < 0.4$ is set to zero.

2.5.2. Test statistic for correlation coefficients

Instead of a threshold, either statistical tests or confidence intervals may be employed for a rigorous statistical analysis. For the sample correlation coefficient, which is an estimate of ϱ, the Fisher transformation

$$F(r_{xy}) = \frac{1}{2} \ln \left(\frac{1 + r_{xy}}{1 - r_{xy}} \right) = \operatorname{arctanh}(r_{xy}) \tag{2.54}$$

is considered. The corresponding random variable is normally distributed with mean $\mu = F(\varrho)$ and standard deviation $\sigma = \frac{1}{\sqrt{m-3}}$, where m is the sample size. The null hypothesis that ϱ equals some value ϱ_0 can be tested by finding the p-value for

$$z = \sqrt{m-3}[F(r_{xy}) - F(\varrho_0)] \tag{2.55}$$

from the standard normal distribution [74].

The hypothesis test of the partial correlation is analogous after reducing m by the dimension of $\boldsymbol{X}$, $u = \dim(\boldsymbol{X})$ [→ Sec. 2.2.6]. The test statistic for the partial correlation is thus $z = \sqrt{m-3-u}[F(r_{xy}) - F(\varrho_0)]$ [75]. In case more than one correlation is assessed statistically, the critical values must be corrected for multiple testing. The rejection of the null hypothesis refers to the significant existence of a link in the network.

2.5.3. Link quantification by the critical value of the correlation coefficient

On the one hand it is proofed in Sec. 2.3 that bivariate measures report nonzero values between nodes n_i, n_j irrespective whether or not they are joined by a physical link as long as they are connected by a path. Consequently, $F(r_{n_i n_j}) - F(0) > 0$. On the other hand, with $F(r_{n_i n_j}) - F(0) > 0$, z becomes arbitrarily large for an increasing sample size m, such that an arbitrarily small p-value can be obtained. Therefore, in the limit of an infinite amount of data, a bivariate measure always reports a complete network.

The effect can be seen by considering again Eq. (2.53) which is obtained from $m = 300$ samples. Evaluation of the p-values at the 95% significance level yields a fully connected network except for the link between X_1 and X_4. By increasing the sample size to $m = 10^6$, the sample correlation matrix becomes

$$\boldsymbol{\mathcal{R}} = \begin{pmatrix} 1.00 & 0.50 & 0.42 & -0.14 \\ 0.50 & 1.00 & 0.84 & -0.29 \\ 0.42 & 0.84 & 1.00 & -0.35 \\ -0.14 & -0.29 & -0.35 & 1.00 \end{pmatrix}, \quad \text{with} \quad p = \begin{pmatrix} 0 & 0 & 0 & 0 \\ 0 & 0 & 0 & 0 \\ 0 & 0 & 0 & 0 \\ 0 & 0 & 0 & 0 \end{pmatrix}, \tag{2.56}$$

such that a complete network must be concluded. This demonstrates that a bivariate measure reports a complete network provided a sufficient amount of data. In other words, whenever a bivariate network analysis does not lead to a complete network, the amount of data is insufficient for the statistics.

2.5.4. Quantification based on multivariate measures

The partial correlation being a multivariate measure is designed to take into account the information of the entire system. Since the interactions defined by Eq. (2.3) are strictly linear, the partial correlation coefficients and p-values estimated from $m = 10^6$ realizations

$$\boldsymbol{\mathcal{P}} = \begin{pmatrix} 1.00 & 0.30 & -0.00 & -0.00 \\ 0.30 & 1.00 & 0.79 & 0.00 \\ -0.00 & 0.79 & 1.00 & -0.20 \\ -0.00 & 0.00 & -0.20 & 1.00 \end{pmatrix}, \quad \text{with} \quad \boldsymbol{p} = \begin{pmatrix} 0.00 & 0.00 & 0.24 & 0.89 \\ 0.00 & 0.00 & 0.00 & 1.00 \\ 0.24 & 0.00 & 0.00 & 0.00 \\ 0.89 & 1.00 & 0.00 & 0.00 \end{pmatrix} \tag{2.57}$$

correctly reveal the physical connectivity of the system. Hence, there is no need to resort to an arbitrary threshold since the statistics of the measures can be readily applied.

In this chapter, the correlation coefficient is characterized with respect to the emergence of indirect links. It is argued, that multivariate measures should be used to avoid indirect links. A series of simulation studies is carried out in the following chapter in order to further analyze the correlation coefficient when used to reconstruct networks from measurements.

Chapter 3.

Network reconstruction and classification - a simulation study

The results presented in this chapter demonstrate the characteristic of the correlation coefficient as derived in the previous chapter, as well as the misclassification of random networks as small-world networks once analyzed by a correlation coefficient. The results are published in [22]: W. Mader, M. Mader, J. Timmer, M. Thiel, and B. Schelter. Networks: On the relation of bi- and multivariate measures. Scientific Reports, 5:10805, 2015 .

The purpose of this chapter is twofold. The first part of the presented simulation study aims at underpinning the theoretical argument for the emergence of indirect links developed in Sec. 2.3. Moreover, the extent of the effect on actually reconstructed networks is investigated. To this end, simulations are conducted on a regular ring network and two variations of random networks.

Due to the intuitively attractive features of the small-world model [→ Sec. 1.3.3], networks in a variety of fields are investigated for being small world. Based on bivariate interdependence measures, small-world networks are reported for brain-functional networks [23, 76–79], seismic [24, 55, 59, 80] and climate networks [15, 25, 57, 81], networks occurring in literature research [82] or computer science [83]. Motivated by the appearance of small-world networks in such diverse fields, the second part of this chapter is concerned with the question, whether the use of bivariate measures also affects the classification of empirical networks as being small world.

3.1. Simulation setup

The simulation study investigates properties of partial correlation matrices and their corresponding bivariate correlation matrices. The general scheme of the study is the following:

1. Generate a partial correlation matrix describing a complex system of interest.
2. Calculate the corresponding bivariate correlation matrix which would have resulted from a bivariate analysis of realizations of the system [→ Sec. 2.3].
3. Analyze the properties of the resulting correlation matrix. If applicable, compare the properties of the correlation and the partial correlation matrix.

In Sec. 2.2.2, an approach for finding the partial covariance matrix for a complex system is described. Therefore, the weighted adjacency matrix $\breve{\boldsymbol{A}}$ of the system has to be defined in the first place. This offers the advantage that correlation coefficients can be calculated in terms of the connection strengths defined in $\breve{\boldsymbol{A}}$. While this is necessary for the preceding discussion on the emergence of indirect links, a simpler approach is sufficient for the simulation study presented in the following. The partial correlation matrix is obtained from the adjacency or incidence matrix of the system directly. To this end, two approaches are pursued. The first is based on diagonally dominant matrices, the second exploits the incidence matrix. Both approaches generate a symmetric, positive-definite matrix matching the topology of the system. The corresponding bivariate correlation matrix is then obtained by matrix inversion [→ Eq. (2.26)].

3.1.1. Diagonally dominant matrix

Derived from Sylvester's criterion [84], a diagonally dominant, Hermitian matrix with real and non-negative diagonal elements is positive definite [85, Prop. 2.6 and Prop. 2.16]. In a diagonally dominant matrix, the sum over each row or column excluding the diagonal element must not exceed the value of the diagonal element [86]. Using this criterion, the adjacency matrix of a network is turned into a partial correlation matrix. For this purpose, the diagonal is set to one, and each nonzero entry of the off-diagonal is replaced by a partial correlation coefficient. The partial correlation coefficients are chosen such that their row-sum is smaller than one. This approach limits the range of possible partial correlation coefficients, since correlation matrices exist which are not diagonally dominant.

3.1.2. Incidence matrix

To broaden the range for partial correlation coefficients, the incidence matrix of a network is employed. The matrix square of the incidence matrix reflects the topology of the network. The matrix square of a weighted incidence matrix hence leads to

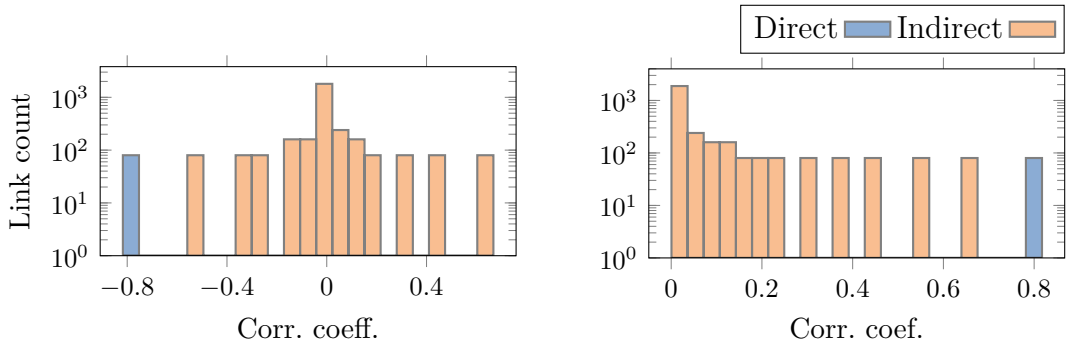

(a) Negative correlation

(b) Positive correlation

Figure 3.1.: Histogram of correlation coefficients. The correlation coefficients corresponding to direct links (blue) have the largest absolute value. Indirect links (orange) successively adopt smaller correlation coefficients with increasing path length. As the resolution of the histogram is reached for small correlation coefficients, the count per correlation value exceeds $M = 80$.

a valid covariance matrix reflecting the network's topology. By normalization, the partial correlation matrix of the system is found.

3.1.3. Considerations on the network size

The study was stimulated by a cooperation in the field of neuroscience. There, brain networks are often investigated based on electroencephalography measurements. This technique usually comprise about 80 sensors. Accordingly, simulations are carried out on networks with $N = 80$ nodes.

3.2. Regular Networks

The aim of this first simulation is to review the Taylor series which describes the emergence of indirect links for bivariate measures [→ Eq. (2.30)]. To this end, a regular ring network with $N = 80$ and $h = 1$ is investigated for the simplicity of the resulting pattern in the correlation matrix. The regular ring network is modeled by a partial correlation matrix with zero off-diagonal elements, except for the first sub- and superdiagonal and the lower left and upper right corner. All nonzero entries are set to ζ which is determined according to the diagonally dominant criterion. As the node degree is $g = 2$ for all nodes, $|\zeta| = 0.49$ is chosen such that $2\,|\zeta| < 1$ holds. A simulation is conducted for $\zeta_\mathrm{n} = -0.49$ and $\zeta_\mathrm{p} = 0.49$, respectively.

Employing the algorithm introduced in Sec. 2.3, the bivariate correlation matrix of the system is calculated. Owing to the structure of the partial correlation matrix, $\boldsymbol{P}^q$ [→ Eq. (2.30)] are symmetric and persymmetric matrices for all $q > 0 \subset \mathbb{N}$. Also,

the values of the i-th off-diagonal equal the values in the $(N+1-i)$-th off-diagonal, where $i \in [1, \lfloor N/2 \rfloor] \subset \mathbb{N}$.

Moreover, for i as above but starting at two, the i-th off-diagonal remains zero for all $\boldsymbol{P}^q$ where $q < i$. The i-th off-diagonal encodes indirect links connecting nodes of distance i. Since the absolute value of the partial correlation coefficient is smaller than one, the correlation coefficients of indirect links decrease with the distance of the indirectly connected nodes.

The correlation matrix of the ring network turns out to be fully populated, encoding direct and indirect links. The histograms of bivariate correlation coefficients are presented in Fig. 3.1. Irrespective of the sign of ζ, links cluster with respect to their constituting path length. Direct links possess the largest correlation coefficient as expected from the framework. In each cluster, 80 links are gathered. On approaching small values of the correlation coefficients, the resolution of the histogram is reached, and multiple clusters stack up in a single bin. Hence, the link count exceeds $M = 80$.

3.3. Random networks

In this section, the above simulation study is applied to random networks. Networks are obtained from the Erdős-Rényi model with $N = 80$ nodes and $M = \lceil N \log(N) \rceil = 351$ links; $N \log(N)$ links guarantee a network with only one component [39, 47].

3.3.1. Constant partial correlation coefficient

In the first simulation on random networks, ζ is the value of the partial correlation coefficients of all links. Thus, compared to the last simulation, only the topology of the network is changed. The partial correlation matrix is constructed using the diagonally dominant criterion. To this end, the maximum node degree $g_{\max}$ is determined from the adjacency matrix. Accordingly, all nonzero entries of the adjacency matrix are set to $\zeta = 0.95/g_{\max}$ and its diagonal is set to one. The correlation matrix is again derived from the partial correlation matrix. As shown in Fig. 3.2, direct links exhibit larger correlation coefficients (blue) than indirect ones (orange). This results from the fact that the correlation coefficients of indirect links are introduced by powers of $\boldsymbol{P}$ starting at $q \geq 2$ [→ Eq. (2.30)], but correlation coefficients of direct links start at $q = 1$. Thus, if all partial correlation coefficients equal ζ, direct and indirect links can be separated by applying a properly chosen threshold to the correlation coefficients.

The structure of a regular ring network is reflected in its partial correlation matrix yielding the clustering of the respective correlation coefficient. In contrast, the partial correlation matrix of a random network is randomly occupied. Hence, even though all links share the same partial correlation coefficient, the node degree varies among nodes and with it the diagonal entries of the bivariate covariance matrix. Therefore, through normalization, a range of bivariate correlation coefficients is obtained.

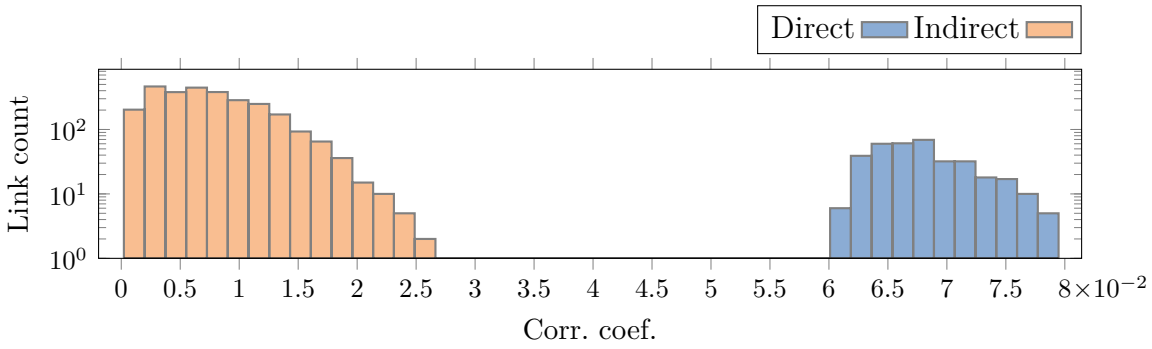

Figure 3.2.: Histogram of correlation coefficients calculated from a $N = 80$, $M = 351$ random network with a shared value of the partial correlation coefficients of all links. Direct (blue) and indirect (orange) links can be separated by a threshold.

The main finding of this simulation is the separation of the correlation coefficients of direct and indirect links in case the strength of all connections are in a narrow range. Consequently, direct and indirect links are successfully discriminated by thresholding bivariate methods. While it is a strong assumption to expect all connections strengths in a narrow range, finding a proper threshold in this situation seems feasible as the correlation coefficients of direct and indirect links fall in disjoint intervals, cf., Fig. 3.2.

3.3.2. Variation of partial correlation coefficients

When dealing with random networks that exhibit varying strengths of connectivity, a more complicated scenario emerges. For this simulation, both methods to construct the partial correlation matrix described in Sec. 3.1 are used. Firstly, in order to construct the partial correlation matrix using the diagonally dominant criterion, the maximum node degree $g_{\max}$ is obtained. Then, realizations of a uniformly distributed random variable in $[0, 0.99/g_{\max}]$ determine the values of the partial correlation coefficients.

Secondly, the partial correlation matrix is obtained by starting with the incidence matrix $\boldsymbol{B}$ of an Erdős-Rényi network with $N = 80$ and $M = 351$. The values of the nonzero entries of $\boldsymbol{B}$ are drawn from the uniform distribution over the interval $[0, 1]$. The partial correlation matrix is obtained as the normalized matrix square of this weighted incidence matrix. According to Eq. (2.42), two strong direct links induce a strong indirect one. Hence, if the strengths of connections in the system spread across a broad interval, the partial correlation coefficients also occupy a broad range. Consequently, it is likely to find a bivariate correlation coefficient of a direct connection which is smaller than the bivariate correlation coefficient of a strong indirect one. This is visualized in Fig. 3.3. Again, correlation coefficients of direct links are shown in blue, correlation coefficients of indirect ones in orange. In Fig. 3.3 (a), the histogram for the diagonally dominant construction of the partial correlation matrix is presented. The histogram for the construction based on the incidence matrix is given

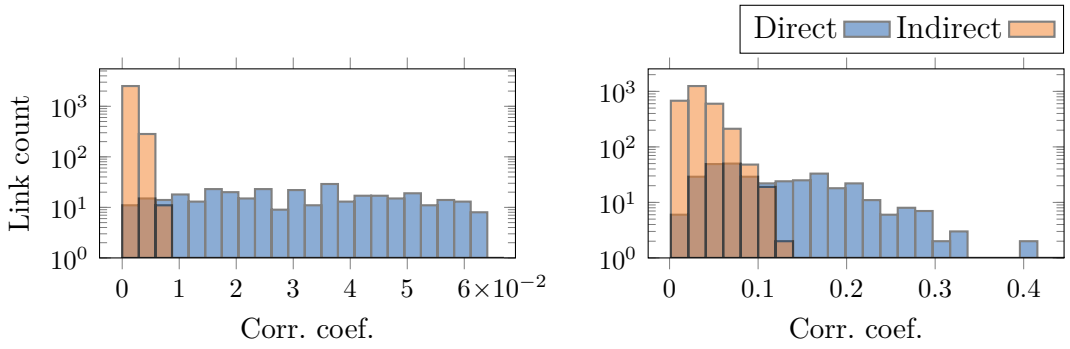

(a) Diagonally dominant property

(b) Incidence matrix square

Figure 3.3.: Histograms of correlation coefficients calculated for a $N = 80$, $M = 351$ random network with varying connection strengths. The partial correlation matrix is obtained by the diagonally dominant criteria (a) and the incidence matrix (b). The correlation coefficients of direct (blue) and indirect (orange) links overlap.

in Fig. 3.3 (b). Both histograms show the same qualitative behavior: the distribution of the correlation coefficient of direct and indirect links, respectively, overlap. Thus, any selection criterion, e.g., a threshold operating on correlation coefficients must report a mixture of direct and indirect links. Direct and indirect links are not distinguishable by the bivariate correlation coefficient.

In general, when estimating links from measurements, the underlying system is unknown. Typically, the system exhibits a non-regular topology combined with varying connection strengths. As demonstrated, bivariate interdependence measures are inept to reveal the correct network topology.

As discussed in the next section, this result has also implications for the classification of reconstructed networks.

3.4. Small-world classification in application

In Sec. 1.3.3, the small-world model is introduced. From a theoretical point of view, a network is considered small world, if $L(N)$ scales at most logarithmically with N and C is large [11, 12, 53, 87]. However, when a network G_a is analyzed in application, the scaling of $L(N)$ is often not accessible because G_a has a fixed number of nodes. To infer whether G_a complies with the small-world model, its average distance and clustering coefficient, say L_a and C_a, are compared to the respective properties L_rnd and C_rnd of a random network G_rnd; G_rnd is constructed such that is has the same number of nodes and the same average node degree as G_a [11, 88]. Now, if $L_\mathrm{a} \gtrapprox L_\mathrm{rnd}$ and $C_\mathrm{a} \gg C_\mathrm{rnd}$, G_a is considered to exhibit the small-world phenomenon [11]. Due to the nature of random networks, L_rnd and C_rnd are random variables. Hence, normalizing G_a with a single realization G_rnd is not representative. Instead, the mean values $\bar{L}_\mathrm{rnd}$ and $\bar{C}_\mathrm{rnd}$

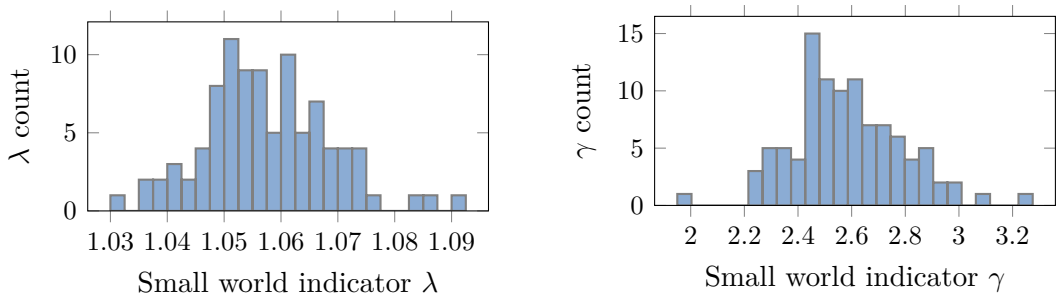

(a) Histogram of λ

(b) Histogram of γ

Figure 3.4.: Histograms of the small-world indicators λ and γ for random networks analyzed by a bivariate interdependence measure. The values of λ and γ are calculated for 100 realizations of G_a. Since $\lambda \approx 1$ and $\gamma > 1$ for all realizations, every random network observed through correlation coefficients is falsely classified as small world.

averaged over multiple realizations of the random model are used for normalization. In literature, the small-world conditions are usually formulated as

$$\lambda = L_\mathrm{a}/\bar{L}_\mathrm{rnd}\,, \tag{3.1}$$

$$\gamma = C_\mathrm{a}/\bar{C}_\mathrm{rnd}\,, \tag{3.2}$$

where $\lambda \approx 1$ and $\gamma \gg 1$ must hold in order to characterize G_a as a small-world network [11, 21].

3.5. Bivariate measures and the small-world phenomenon

The preceding sections demonstrated analytically and by simulations that in general, network reconstruction from data by bivariate measures fails. In this section, it is shown that bivariate measures also have an noteworthy impact on the classification of the reconstructed network with respect to the small-world phenomenon.

The simulation study pursuing this question has the following set-up. Firstly, λ_rnd and γ_rnd are sampled from 100 realizations of the Erdős-Rényi model $G_{N,M}$ with parameters $N = 80$ and $M = \lceil N \log(N) \rceil = 351$. From this ensemble, $\bar{L}_\mathrm{rnd}$ and $\bar{C}_\mathrm{rnd}$ is calculated to be used in Eqs. (3.1) and (3.2).

Secondly, the network G_a is generated. To this end, again, a realization of $G_{N,M}$ is drawn and its incidence matrix is used to construct a partial correlation matrix thereof. From this partial correlation matrix, the bivariate correlation matrix is calculated [→ Eq. (2.26)]. In order to obtain a network comparable to its random ancestor, a threshold is applied to the bivariate correlation matrix to select the $M = 351$ strongest links. This procedure yields the network G_a, in accordance to the strategy frequently applied in literature [11, 15, 23–26]. Using Eqs. (3.1) and (3.2), G_a is assessed for the small-world property. In order to sample the distribution of the small-world classifiers

λ and γ derived from networks of the type of G_{a}, this procedure is repeated 100 times. Because the variance of $\bar{L}_{\mathrm{rnd}}$ and $\bar{C}_{\mathrm{rnd}}$ is negligible, the same averages $\bar{L}_{\mathrm{rnd}}$ and $\bar{C}_{\mathrm{rnd}}$ are used in all repetitions.

The result of the simulation is summarized in Fig. 3.4. In Fig. 3.4 (a), the small-world indicator λ for all 100 realizations of G_{a} is presented, in Fig. 3.4 (b) the indicator γ is shown. By construction, the network underlying G_{a} is truly random as it is a realization of $G_{N,M}$. After the network has undergone a correlation analysis, it exhibits the small-world property in all 100 cases. All random networks are falsely classified as small-world ones. The explanation of the result is the transitivity property of bivariate measures for which the mathematical foundation is given in Sec. 2.3. This result applies to all networks in which links are established by a naive application of a bivariate interdependence measure irrespective of the dynamics observed, the measurement technique used, or the specific bivariate measure employed.

Summary of: Network reconstruction and classification

Complex systems such as power grids, the brain, the climate, social communities, or the interaction of different earthquake-prone areas are commonly modeled and visualized as networks.

In Chap. 1, networks are defined as a set of nodes and a set of links. Based on different properties, certain network models may be characterized. Models for regular-ring, random, and small-world networks are considered in this chapter. They are distinguished by the scaling of the average distance and the clustering coefficient with the network size. It is shown that in the regular-ring model the average distance scales linearly with the network size while the clustering coefficient is a function of the degree of nodes only. In the random model, the average distance scales logarithmically rather than linearly. The clustering coefficient depends inversely on the network size, tending to zero for increasing networks. Compared to the regular-ring model, average distances in the random model are short and clustering coefficients are low. In the small-world model, the average distance scales logarithmically as in random networks, while the clustering coefficient is comparable to that of regular networks. A realization of the small-world model is the realization of the regular-ring model in which links are randomly rewired with a certain probability. A critical rewiring probability w_{sc} is defined at which realizations of the small-world model differ from regular-ring networks. A second critical rewiring probability w_{rd} is given at which the clustering coefficient starts to decline and realizations of the small-world model become indistinguishable from realizations of the random model. For a rewiring probability $w \in [w_{\mathrm{sc}}, w_{\mathrm{rd}}] \subset \mathbb{R}$, realizations of the small-world model exhibit the small-world property. Using expressions for both critical values, it is argued that for relevant network sizes the small-world regime is included in the small-world model. In other words, the average distance always declines considerably earlier than the clustering coefficient.

In Chap. 2, the construction of the network representation of a complex system based on data measured from the complex system is addressed. Usually, the nodes in

the representing network are identified with the recording sites at which the dynamics of the complex system are observed. Network links are established by quantifying coefficients reported by an interdependence measure applied to the recorded dynamics. Interdependence measures can either be bi- or multivariate in nature. Bivariate measures quantify the relation of two nodes without taking into account third-party influences. As analytically derived, these measures induce indirect links that do not correspond to physical connections in the observed system. On the contrary, multivariate measures do take third-party influences into account, such that indirect links can be avoided. As shown, multivariate measures are obtained from bivariate measures by partialization, i.e., by removing linear influences of the remaining nodes onto the two nodes for which the linkage is established. Partialization may equivalently be achieved by linear regression or by matrix inversion. By expanding the matrix inversion in a Taylor series, the emergence of indirect links in bivariate measures is rendered explicit on an analytical footing. As an example, the correlation coefficient is considered.

In Chap. 3, a series of simulations is presented to show the effect of bivariate measures onto the reconstruction of networks and their classification oneran the example of the correlation coefficient. In a first simulation study, the effect of bivariate measures onto network reconstruction is investigated for the case that linkage strengths are the same across all connections in a truly regular-ring network. As expected from the Taylor expansion presented in Chap. 2, direct links exhibit higher values of the correlation coefficient than indirect ones. In fact, the correlation coefficients of indirect links become smaller as the path length constituting the indirect link becomes larger. In the second simulation study, the same setting is applied to truly random networks. Again, direct links exhibit higher values than indirect links. However, now the degree of indirectness is no longer determinable from the linkage strength. As of the third simulation study, direct links are indistinguishable from indirect links by their correlation coefficients when different linkage strengths prevail in the investigated network. A mixture of direct and indirect links is identified when determining relevant links by their correlation coefficients. In the fourth simulation study, the effect of bivariate measures on the network classification is explored. To this end, random networks are generated and bivariately treated for network reconstruction. Average distance and clustering coefficients are computed to determine whether the reconstructed networks are of small-world type. As expected from theory, networks reconstructed by a bivariate measure are falsely classified as small world even though they are inherently random.

Part II.

Parameter estimation in dynamic processes

Chapter 4.

Efficient parameter estimation in the state-space model

The expectation-maximization algorithm allows to construct maximum-likelihood estimators in the case of missing values in data. The computational complexity of the algorithm leads to long runtimes of the derived estimators. In this chapter, two provisions which reduce the runtime considerably are proposed and implemented. The main results of this chapter are published in [34]: W. Mader, Y. Linke, M. Mader, L. Sommerlade, J. Timmer, and B. Schelter. A numerically efficient implementation of the expectation maximization algorithm for state space models. Applied Mathematics and Computation, 241:222–232, 2014.

The preceding part treats the reconstruction of networks from observations. To this end, the partial correlation was especially highlighted which assumes independent and identically distributed (*iid*) observations from a multivariate normal distribution. However, consecutive states of a natural process are usually correlated over time. Recordings of such states are called time series [89]. The model

$$\boldsymbol{X}(t) = \boldsymbol{C}\boldsymbol{X}(t-1) + \boldsymbol{\epsilon}(t)\,, \quad \boldsymbol{\epsilon}(t) \sim \mathcal{N}(\boldsymbol{0}, \boldsymbol{Q}) \tag{4.1}$$

yields such *autocorrelated* states $\boldsymbol{X}(t)$. Let

$$\boldsymbol{C} = \begin{pmatrix} a_1 & 0 & 0 \\ b_{21} & a_2 & 0 \\ 0 & b_{32} & a_3 \end{pmatrix}\,, \quad \boldsymbol{Q} = \begin{pmatrix} q_1 & 0 & 0 \\ 0 & q_2 & 0 \\ 0 & 0 & q_3 \end{pmatrix}\,, \tag{4.2}$$

then $\boldsymbol{X} = (X_1, X_2, X_3)^{\mathrm{T}}$ and, as derived in App. B.1,

$$\begin{aligned}
\operatorname{var}(X_1) &= \frac{q_1}{1-a_1^2}\,, \\
\operatorname{cov}(X_1, X_2) &= \frac{a_1 b_{21} \operatorname{var}(X_1)}{1-a_1 a_2}\,, \\
\operatorname{var}(X_2) &= \frac{q_2 + b_{21}^2 \operatorname{var}(X_1) + 2a_2 b_{21} \operatorname{cov}(X_1, X_2)}{1-a_2^2}\,, \\
\operatorname{cov}(X_1, X_3) &= \frac{a_1 b_{32} \operatorname{cov}(X_1, X_2)}{1-a_1 a_3}\,, \\
\operatorname{cov}(X_2, X_3) &= \frac{a_2 b_{32} \operatorname{var}(X_2) + a_3 b_{21} \operatorname{cov}(X_1, X_3) + b_{21} b_{32} \operatorname{cov}(X_1, X_2)}{1-a_2 a_3}\,, \\
\operatorname{var}(X_3) &= \frac{q_3 + b_{32}^2 \operatorname{var}(X_2) + 2a_3 b_{32} \operatorname{cov}(X_2, X_3)}{1-a_3^2}\,.
\end{aligned} \tag{4.3}$$

The covariance of the first and the third process

$$\operatorname{cov}(X_1, X_3) = \frac{a_1^2 b_{21} b_{32} q_1}{(1-a_1^2)(1-a_1 a_2)(1-a_1 a_3)} \tag{4.4}$$

is in general nonzero, in contrast to their physical connectivity. While this is expected for the correlation coefficient, it also holds for the partial correlation coefficient. Up to normalization and sign, the partial correlation coefficient is obtained by inverting the correlation matrix with elements Eq. (4.3). The insufficiency of the partial correlation for autocorrelated processes is made explicit by the following numerical example. Setting $a_1 = 0.8$, $a_2 = 0.7$, $a_3 = 0.5$, $b_{21} = 0.3$, and $b_{32} = 0.6$, the partial correlation coefficient and its p-values estimated from $m = 10^5$ realizations are

$$\boldsymbol{\mathcal{P}} = \begin{pmatrix} 1.00 & 0.38 & -0.02 \\ 0.38 & 1.00 & 0.64 \\ -0.02 & 0.64 & 1.00 \end{pmatrix}, \quad \text{with} \quad \boldsymbol{p} = \begin{pmatrix} 0.00 & 0.00 & 0.21 \\ 0.00 & 0.00 & 0.00 \\ 0.21 & 0.00 & 0.00 \end{pmatrix} \times 10^{-7}\,, \tag{4.5}$$

indicating a complete network. This result holds in general.

In order to infer the correct interaction structure including directional information, the matrices $\boldsymbol{C}$ and $\boldsymbol{Q}$ need to be estimated. To this end, a powerful method is parameter estimation in the so-called state-space model (SSM) [→ Sec. 4.1] by the method of maximum-likelihood (ML) [→ Sec. 4.2]. The expectation-maximization (EM) algorithm [→ Sec. 4.3] allows to construct a maximum-likelihood estimator (MLE) for the parameters in the SSM [32]. However, the EM algorithm is a runtime intensive procedure. The work presented in this chapter aims at considerably reduce this runtime, such that the application of the EM algorithm to large data sets becomes feasible [33, 34]. Suitable strategies are presented in Sec. 4.6. In Sec. 4.7, the implementation of the optimized algorithm is applied to simulated data in order to demonstrate the decrease in runtime as well as to assess its accuracy. *

*The optimized EM algorithm can be freely obtained from https://github.com/wmader/fdmb.

Concerning the reconstruction of networks, several interdependence measures in the time and frequency domain are defined based on the parameters of the SSM [18, 29–31, 33]. Thus, once parameters are estimated, these measures are available to quantify interactions.

4.1. The state-space model

A versatile model tailored to time-series data is the state-space model (SSM) [27, 89, 90]. In the SSM, the so-called dynamic equation models the state of the process of interest, while its observation is modeled by a separate observation equation.

4.1.1. The autoregressive process

The process informally introduced by Eq. (4.1) is called multivariate or vector-autoregressive process (VAR) [91]. The most general form of a VAR[p] of order p is

$$\boldsymbol{X}(t) = \sum_{\tau=1}^{p} \boldsymbol{C}(t,\tau)\boldsymbol{X}(t-\tau) + \boldsymbol{\epsilon}(t)\,, \quad \boldsymbol{\epsilon}(t) \sim \mathcal{N}\left(\boldsymbol{0}, \boldsymbol{Q}(t)\right)\,. \tag{4.6}$$

The k-dimensional state vector $\boldsymbol{X}(t)$ of time t is obtained from the p previous state vectors and additive *driving noise* $\boldsymbol{\epsilon}(t)$ [27, 89]. Driving noise is modeled by a $k \times 1$-dimensional normal random vector with zero mean and covariance matrix $\boldsymbol{Q}(t)$. The correlation of successive states is determined by the transition matrices $\boldsymbol{C}(t,\tau)$. The matrices $\boldsymbol{C}(t,\tau)$ and $\boldsymbol{Q}(t)$ are of dimension $k \times k$. The initial value $\boldsymbol{X}(0)$ of Eq. (4.6) is drawn from the normal distribution with mean $\boldsymbol{\mu}_0$ and covariance $\boldsymbol{\Sigma}_0$. Throughout this chapter, $\boldsymbol{C}(\tau)$ and $\boldsymbol{Q}$ are assumed time constant. In that case, the normal distribution with parameters $\boldsymbol{\mu}_0 = \mathrm{E}[\boldsymbol{X}(t)] = \boldsymbol{0}$ and $\boldsymbol{\Sigma}_0 = \mathrm{E}[\boldsymbol{X}(t)\boldsymbol{X}(t)^{\mathrm{T}}]$ is the density of the process. The covariance matrix is calculated as $\mathrm{vec}[\boldsymbol{\Sigma}_0] = \mathrm{vec}[(\boldsymbol{I} - \boldsymbol{C} \otimes \boldsymbol{C})^{-1}]\,\mathrm{vec}[\boldsymbol{Q}]$, using the Kronecker product $\otimes$ and the vec operation [92]. The initial value $\boldsymbol{X}(0)$ is than drawn from this distribution.

Driving noise

Driving noise is part of the dynamics of a system. It accounts for the intrinsic stochasticity of a process, such as the movement of pollen grains in water [93]. Driving noise is also employed to model the average effect of details of the system which are unknown or too subtle to be modeled explicitly. In that case, driving noise straightens the discrepancy between the model and the modeled system. The central limit theorem justifies to model driving noise as a normal random variable. Driving noise is modeled without time correlation, such that consecutive realizations are independent.

Embedding of a vector-autoregressive process of order p

Analogous to formulating a k-dimensional differential equation of order p as a kp-dimensional equation of order one, a k-dimensional VAR[p] can be formulated as kp-dimensional VAR[1]. By embedding, ${}_{\mathrm{e}}(\cdot)$, the transition matrix, state, and noise vector, Eq. (4.6) translates to [89]

$$ {}_{\mathrm{e}}\boldsymbol{X}(t) = \underbrace{\begin{pmatrix} \boldsymbol{C}(1) & \boldsymbol{C}(2) & \dots & \boldsymbol{C}(p-1) & \boldsymbol{C}(p) \\ \boldsymbol{I} & \boldsymbol{0} & \dots & \boldsymbol{0} & \boldsymbol{0} \\ \boldsymbol{0} & \boldsymbol{I} & \dots & \boldsymbol{0} & \boldsymbol{0} \\ \vdots & \vdots & \ddots & \vdots & \vdots \\ \boldsymbol{0} & \boldsymbol{0} & \dots & \boldsymbol{I} & \boldsymbol{0} \end{pmatrix}}_{{}_{\mathrm{e}}\boldsymbol{C}} \underbrace{\begin{pmatrix} \boldsymbol{X}(t-1) \\ \boldsymbol{X}(t-2) \\ \boldsymbol{X}(t-3) \\ \vdots \\ \boldsymbol{X}(t-p) \end{pmatrix}}_{{}_{\mathrm{e}}\boldsymbol{X}(t-1)} + \underbrace{\begin{pmatrix} \boldsymbol{\epsilon}(t) \\ \boldsymbol{0} \\ \boldsymbol{0} \\ \vdots \\ \boldsymbol{0} \end{pmatrix}}_{{}_{\mathrm{e}}\boldsymbol{\epsilon}(t)} . \tag{4.7} $$

The sum over the past p states in Eq. (4.6) is rewritten as the product of the $kp \times kp$ matrix ${}_{\mathrm{e}}\boldsymbol{C}$ and the $kp \times 1$ state vector ${}_{\mathrm{e}}\boldsymbol{X}_t = (\boldsymbol{X}(t)^{\mathrm{T}}, \dots, \boldsymbol{X}(t-p+1)^{\mathrm{T}})^{\mathrm{T}}$. The $kp \times kp$ covariance matrix of the driving noise is zero except for the upper left corner which contains $\boldsymbol{Q}$. Thus, without loss of generality, the following discussion is confined to VAR[1] processes.

4.1.2. Observation of the process

Empirical signals are often obscured by a significant amount of *observational noise*. Observational noise is provoked by different sources such as temperature, stochastic movement, or fluctuations in the medium through which a system is observed: an example for the latter is the flickering of stars when observed through an atmosphere.

In the SSM, the observation of the state vector $\boldsymbol{X}(t)$ is modeled by

$$ \boldsymbol{Y}(t) = \boldsymbol{O}\boldsymbol{X}(t) + \boldsymbol{\eta}(t) , \quad \boldsymbol{\eta}(t) \sim \mathcal{N}(\boldsymbol{0}, \boldsymbol{R}) , \tag{4.8} $$

where $\boldsymbol{O}$ is the $o \times kp$ observation matrix and $\boldsymbol{\eta}(t)$ additive observational noise. The dimension of $\boldsymbol{Y}(t)$ and $\boldsymbol{\eta}(t)$ is $o \times 1$. Due to the central limit theorem, observational noise can be assumed normally distributed with zero mean and $o \times o$ covariance matrix $\boldsymbol{R}$. As some components of $\boldsymbol{X}(t)$ may go unobserved while others may contribute to more than one component of $\boldsymbol{Y}(t)$, $o \neq kp$ is allowed. This applies in particular when formulating a VAR[p] process as a VAR[1] process, where only the first k states are observed. Since $\boldsymbol{X}(t)$ is not directly observable, it is referred to as *hidden state*. The dynamic and observation equation assemble the SSM

$$ \begin{aligned} \boldsymbol{X}(t) &= \boldsymbol{C}\boldsymbol{X}(t-1) + \boldsymbol{\epsilon}(t) , & \boldsymbol{\epsilon}(t) &\sim \mathcal{N}(\boldsymbol{0}, \boldsymbol{Q}) , \\ \boldsymbol{Y}(t) &= \boldsymbol{O}\boldsymbol{X}(t) + \boldsymbol{\eta}(t) , & \boldsymbol{\eta}(t) &\sim \mathcal{N}(\boldsymbol{0}, \boldsymbol{R}) . \end{aligned} \tag{4.9} $$

4.1.3. Gauge invariance and the uniqueness of parameters

Identical observations $\boldsymbol{Y}(t)$ can be obtained from an infinite number of combinations of matrices $\boldsymbol{C}$, $\boldsymbol{O}$, and $\boldsymbol{Q}$, since the SSM is invariant under a continuous transformation with an invertible matrix $\boldsymbol{L}$. Consider the substitution

$$\boldsymbol{X}(t) \to \tilde{\boldsymbol{X}}(t) = \boldsymbol{L}\boldsymbol{X}(t)\,, \tag{4.10}$$

and the accordingly transformed SSM

$$\begin{aligned} \boldsymbol{L}\boldsymbol{X}(t) &= \boldsymbol{L}\boldsymbol{C}\boldsymbol{L}^{-1}\boldsymbol{L}\boldsymbol{X}(t-1) + \boldsymbol{L}\boldsymbol{\epsilon}(t)\,, \\ \boldsymbol{Y}(t) &= \boldsymbol{O}\boldsymbol{L}^{-1}\boldsymbol{L}\boldsymbol{X}(t) + \boldsymbol{\eta}(t)\,. \end{aligned} \tag{4.11}$$

By renaming the variables in Eq. (4.11)

$$\begin{aligned} \tilde{\boldsymbol{X}}(t) &= \tilde{\boldsymbol{C}}\tilde{\boldsymbol{X}}_{t-1} + \tilde{\boldsymbol{\epsilon}}(t)\,, \quad \tilde{\boldsymbol{\epsilon}} \sim \mathcal{N}\left(\boldsymbol{0}, \boldsymbol{L}\boldsymbol{Q}\boldsymbol{L}^{-1}\right)\,, \\ \boldsymbol{Y}(t) &= \tilde{\boldsymbol{O}}\tilde{\boldsymbol{X}}(t) + \boldsymbol{\eta}(t)\,, \quad \boldsymbol{\eta} \sim \mathcal{N}\left(\boldsymbol{0}, \boldsymbol{R}\right)\,, \end{aligned} \tag{4.12}$$

the observation $\boldsymbol{Y}(t)$ of the original SSM is retained from a SSM with transformed parameters $\tilde{\boldsymbol{C}}$, $\tilde{\boldsymbol{O}}$, and $\tilde{\boldsymbol{Q}}$. In order to determine the parameters of the SSM from observations $\boldsymbol{Y}(t)$, this ambiguity has to be resolved. This can e.g., be achieved by setting $\boldsymbol{O} = \boldsymbol{I}$. In consequence, the observation of linear combinations of $\boldsymbol{X}(t)$ is removed from the model. However, the linear combination of observations can be interpreted as instantaneous interactions, which are just as well encoded by correlated driving noise. Consequently, $\boldsymbol{Q}$ may gain nonzero off-diagonal entries for $\boldsymbol{O} = \boldsymbol{I}$. By this choice, the parameters $\boldsymbol{\Theta} = \{\boldsymbol{C}, \boldsymbol{Q}, \boldsymbol{R}\}$ remain to be estimated.

4.2. Maximum-likelihood estimation

For parameter fitting, the *method of maximum likelihood* [94, 95] is by far the most general and powerful option [96]. Suppose a distribution with probability density function $f(Y; \boldsymbol{\Theta})$ parametrized by $\boldsymbol{\Theta}$. Let $\boldsymbol{Y} = (Y_1, \ldots, Y_m)$ be *iid* observations from that distribution with realizations $\boldsymbol{y} = (y_1, \ldots, y_m)$. Since $\mathrm{cov}(Y_i, Y_j) = 0$ for all $i, j \in \{1, \ldots, m\}, i \neq j$, their joint probability density function is

$$f(\boldsymbol{y}; \boldsymbol{\Theta}) = \prod_{i=1}^{m} f(y_i; \boldsymbol{\Theta})\,, \tag{4.13}$$

and

$$\int \cdots \int_{-\infty}^{\infty} f(\boldsymbol{y}; \boldsymbol{\Theta})\, \mathrm{d}y_1 \cdot \ldots \cdot \mathrm{d}y_m = 1\,. \tag{4.14}$$

For a fixed value of $\boldsymbol{\Theta}$, $f(\boldsymbol{y}; \boldsymbol{\Theta})$ in Eq. (4.13) is the probability of a realization $\boldsymbol{y}$ of $\boldsymbol{Y}$. In this view, $f(\boldsymbol{y}; \boldsymbol{\Theta})$ is a function of $\boldsymbol{y}$. Considered as a function of unknown parameters $\boldsymbol{\Theta}$ but with fixed observations $\boldsymbol{y}$,

$$L(\boldsymbol{y} \,|\, \boldsymbol{\Theta}) = \prod_{i=1}^{m} f(y_i; \boldsymbol{\Theta}) \tag{4.15}$$

is called the *likelihood* function. Note that this is not a probability density function, since

$$\int_{-\infty}^{\infty} f(\boldsymbol{y};\boldsymbol{\Theta})\,\mathrm{d}\boldsymbol{\Theta} \neq 1\,. \tag{4.16}$$

The value maximizing Eq. (4.16) is the most plausible for $\boldsymbol{\Theta}$ given the observed data. Therefore,

$$\hat{\boldsymbol{\Theta}} = \arg\max_{\boldsymbol{\Theta}} L(\boldsymbol{y}\,|\,\boldsymbol{\Theta}) \tag{4.17}$$

is the *maximum-likelihood estimate* of $\boldsymbol{\Theta}$. It is often convenient to consider the log-likelihood function

$$\mathcal{L}(\boldsymbol{y}\,|\,\boldsymbol{\Theta}) = \ln L(\boldsymbol{y}\,|\,\boldsymbol{\Theta})\,, \tag{4.18}$$

which can equally well be maximized to obtain $\hat{\boldsymbol{\Theta}}$.

The method of maximum likelihood allows to construct estimators in a generic way. An estimator for $\boldsymbol{\Theta}$ which is unbiased and a fully sufficient statistic for $\boldsymbol{\Theta}$ is termed *fully efficient* [96]. A maximum-likelihood estimator (MLE) is asymptotically fully efficient.

4.3. The expectation-maximization algorithm

In the case of the SSM, the likelihood function as given in Eq. (4.15) depends on the realization of the observation $\boldsymbol{y}$ but also on the realization of the hidden state $\boldsymbol{x}$. As $\boldsymbol{x}$ is unobserved, the method of maximum likelihood cannot be employed directly.

The expectation-maximization (EM) algorithm [→ Fig. 4.1] is a generic algorithm to obtain an iterative ML estimate of parameters from incomplete data, e.g., $\boldsymbol{y}$ in the SSM [89, 97]. To this end, the joint probability density function of the complete data, the union of $\boldsymbol{x}$ and $\boldsymbol{y}$, is required. Let $f(\boldsymbol{x},\boldsymbol{y};\boldsymbol{\Theta})$ be this joint probability density function. Establishing a MLE based on the EM algorithm for a specific model is a two-stage process. Firstly, by assuming some parameter value $\boldsymbol{\Theta}^{\varsigma}$ for $\boldsymbol{\Theta}$, the expected value of the log-likelihood function

$$\mathrm{E}[\mathcal{L}(\boldsymbol{X},\boldsymbol{y}\,|\,\boldsymbol{\Theta})\,|\,\boldsymbol{y},\boldsymbol{\Theta}^{\varsigma}] = \tilde{\mathcal{L}}(\mathrm{E}[\boldsymbol{X}\,|\,\boldsymbol{y},\boldsymbol{\Theta}^{\varsigma}],\boldsymbol{y}\,|\,\boldsymbol{\Theta}) \tag{4.19}$$

must be derived. The expected value $\mathrm{E}(\boldsymbol{X}\,|\,\boldsymbol{y},\boldsymbol{\Theta}^{\varsigma})$ is conditioned on the observation $\boldsymbol{y}$ and $\boldsymbol{\Theta}^{\varsigma}$. It is important to note that Eq. (4.19) is still a function of $\boldsymbol{\Theta}$. In the second step, Eq. (4.19) is maximized with respect to each parameter Θ_i by solving

$$\frac{\partial\tilde{\mathcal{L}}(\mathrm{E}[\boldsymbol{X}\,|\,\boldsymbol{y},\boldsymbol{\Theta}^{\varsigma}],\boldsymbol{y}\,|\,\boldsymbol{\Theta})}{\partial\Theta_i} = 0\,. \tag{4.20}$$

For each Θ_i, an update equation of the form

$$\Theta^{\varsigma+1} = g[\mathrm{E}(\boldsymbol{X}\,|\,\boldsymbol{y},\boldsymbol{\Theta}^{\varsigma})]\,, \tag{4.21}$$

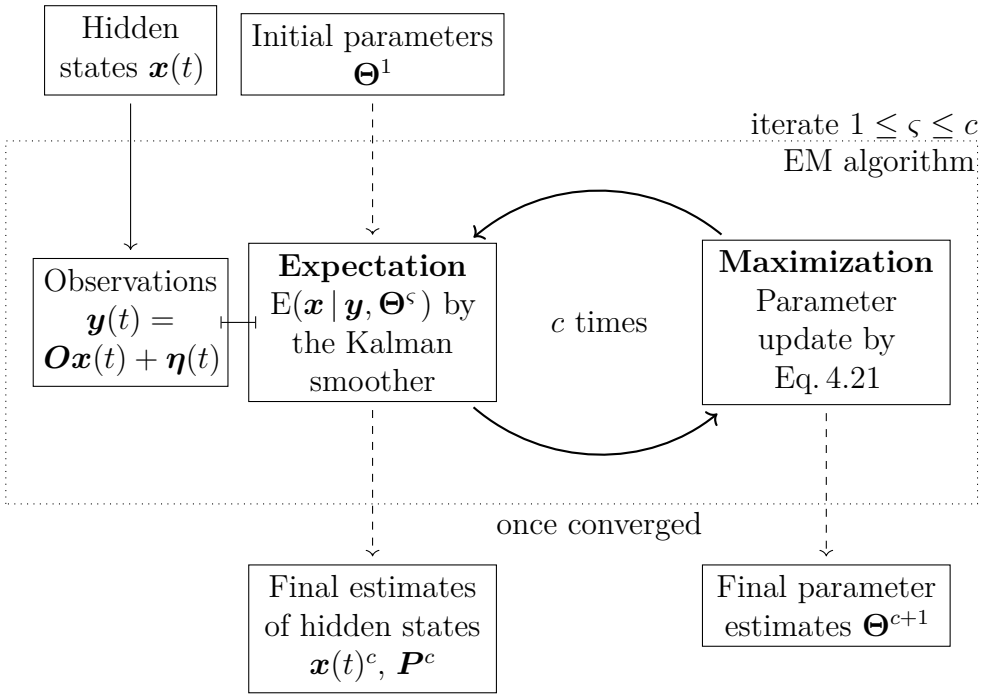

Figure 4.1.: Expectation-maximization procedure for the state-space model. The Kalman smoother provides the conditional expected values appearing in Eq. (4.19). With these at hand, parameter updates as sketched in Eq. (4.21) yield an updated parameter vector. The EM algorithm is initialized with parameters $\boldsymbol{\Theta}^1$, which have the sole constraint to define a stationary SSM. At convergence after c iterations, $\boldsymbol{\Theta}^{c+1}$ is the ML estimate of $\boldsymbol{\Theta}$.

results, i.e., $\Theta^{\varsigma+1}$ is some function g of $\mathrm{E}(\boldsymbol{X} \mid \boldsymbol{y}, \boldsymbol{\Theta}^\varsigma)$.

As implied by Eqs. (4.19) and (4.21), the EM algorithm is iterative involving two steps. In the first step, $\mathrm{E}(\boldsymbol{X} \mid \boldsymbol{y}, \boldsymbol{\Theta}^\varsigma)$ is attained. If the value of $\tilde{\mathcal{L}}$ is of interest, Eq. (4.19) can be evaluated. This step is commonly termed the *expectation step*. In the second step, the update equations are evaluated evolving the parameter values from $\boldsymbol{\Theta}^\varsigma$ to $\boldsymbol{\Theta}^{\varsigma+1}$. This is known as the *maximization step*. These two steps are iterated until some convergence criterion is reached. This criterion is either the difference of the incomplete-data likelihood of consecutive iterations [89, 98], or some measure of parameter change of consecutive iterations [34]. Unfortunately, a small variation in one does not imply a small variation in the other or even global optimality of parameter estimates. Since the objective is to estimate parameters, it remains advisable to define convergence by parameter change. When converged after, say, c iterations, $\boldsymbol{\Theta}^{c+1}$ is a ML estimate of $\boldsymbol{\Theta}$.

In the SSM, the conditional expected value $\mathrm{E}(\boldsymbol{X} \mid \boldsymbol{y}, \boldsymbol{\Theta}^\varsigma)$ is provided by the Kalman smoother which itself is based on the Kalman filter.

4.4. Kalman filter and smoother

Let a noisy time series $\boldsymbol{y}(t)$ be recorded up to time t. Then, for time s, some statement is to be made about $\boldsymbol{y}(s)$. For $s < t$, the problem is called *smoothing*, for $s = t$ *filtering*, and for $s > t$ *prediction*.

In 1960, Rudolf E. Kalman introduced a formalism to obtain an estimate $\hat{\boldsymbol{x}}$ of the hidden states $\boldsymbol{X}$ in the SSM based on the observations $\boldsymbol{y}$ [27]. According to this formalism, the average mean squared error

$$\mathrm{E}[(\boldsymbol{X}_t - \hat{\boldsymbol{x}}_t)^2 \,|\, \boldsymbol{y}_1, \ldots, \boldsymbol{y}_t] \tag{4.22}$$

is to be minimized. In order to allow for a tight notation, time is given as subscript $(\cdot)_t$ for the rest of this chapter. The formalism of minimizing Eq. (4.22) is nowadays well known as *Kalman filter*. Despite its name, it includes filtering and prediction of $\boldsymbol{X}$ as well as the reconstruction of unobserved dimensions of $\boldsymbol{X}$ in case of $o < k$ [27].

The conditional expected values introduced now use the notation, that the subscript t denotes the estimation time point and the superscript s up to which measurement it is conditioned on. Thus, the conditional expected value of the state vector $\boldsymbol{X}$ is [32, 89]

$$\hat{\boldsymbol{x}}_t^s = \mathrm{E}[\boldsymbol{X}_t \,|\, \boldsymbol{y}_1, \ldots, \boldsymbol{y}_s]\,, \tag{4.23}$$

and its conditional error covariance is

$$\begin{aligned} \boldsymbol{P}_{t_1,t_2}^s &= \mathrm{E}[(\boldsymbol{X}_{t_1} - \hat{\boldsymbol{x}}_{t_1}^s)(\boldsymbol{X}_{t_2} - \hat{\boldsymbol{x}}_{t_2}^s)^{\mathrm{T}}] \\ &\overset{g}{=} \mathrm{E}[(\boldsymbol{X}_{t_1} - \hat{\boldsymbol{x}}_{t_1}^s)(\boldsymbol{X}_{t_2} - \hat{\boldsymbol{x}}_{t_2}^s)^{\mathrm{T}} \,|\, \boldsymbol{y}_1, \ldots, \boldsymbol{y}_s] \\ &= \mathrm{cov}(\boldsymbol{X}_{t_1}, \boldsymbol{X}_{t_2} \,|\, \boldsymbol{y}_1, \ldots, \boldsymbol{y}_s)\,. \end{aligned} \tag{4.24}$$

The relation $\overset{g}{=}$ only holds if $\boldsymbol{X}_t$ is Gaussian [89]. For $t_1 = t_2 = t$, the shorthand $\boldsymbol{P}_t^s$ is used.

4.4.1. Kalman filter

The Kalman filter is an iterative algorithm to estimate the hidden state $\boldsymbol{X}$ in the SSM with minimal mean-squared error [→ Eq. (4.22)] [27]. The equations of the Kalman filter are [32, 89, 99]

$$\hat{\boldsymbol{x}}_t^{t-1} = \boldsymbol{C}\hat{\boldsymbol{x}}_{t-1}^{t-1}\,, \tag{4.25}$$

$$\boldsymbol{P}_t^{t-1} = \boldsymbol{C}\boldsymbol{P}_{t-1}^{t-1}\boldsymbol{C}^{\mathrm{T}} + \boldsymbol{Q}\,, \tag{4.26}$$

$$\hat{\boldsymbol{x}}_t^t = \hat{\boldsymbol{x}}_t^{t-1} + \boldsymbol{K}_t\left(\boldsymbol{y}_t - \boldsymbol{O}\hat{\boldsymbol{x}}_t^{t-1}\right)\,, \tag{4.27}$$

$$\boldsymbol{P}_t^t = \boldsymbol{P}_t^{t-1} - \boldsymbol{K}_t\boldsymbol{O}\boldsymbol{P}_t^{t-1}\,, \tag{4.28}$$

$$\boldsymbol{K}_t = \boldsymbol{P}_t^{t-1}\boldsymbol{O}^{\mathrm{T}}\left(\boldsymbol{O}\boldsymbol{P}_t^{t-1}\boldsymbol{O}^{\mathrm{T}} + \boldsymbol{R}\right)^{-1}\,. \tag{4.29}$$

The filter is initialized at $t = 0$ with initial state $\hat{\boldsymbol{x}}_0^0 = \boldsymbol{\mu}_0$ and error covariance $\boldsymbol{P}_0^0 = \boldsymbol{\Sigma}_0$. The initial values $\boldsymbol{\mu}_0$ and $\boldsymbol{\Sigma}_0$ must be provided by external knowledge in the same way as, e.g., $\boldsymbol{C}$ or $\boldsymbol{O}$. Hence, $\hat{\boldsymbol{x}}_0^0$ and $\boldsymbol{P}_0^0$ are considered as parameters of the SSM and are to be estimated in the EM algorithm. The explicit initial values of these parameters are noncritical as long as they yield a stationary SSM.

Based on the predicted state $\hat{\boldsymbol{x}}_t^{t-1}$, the expected observation at time t

$$\hat{\boldsymbol{y}}_t = \mathrm{E}(\boldsymbol{Y}_t \,|\, \boldsymbol{y}_1, \ldots, \boldsymbol{y}_{t-1}) = \boldsymbol{O}\hat{\boldsymbol{x}}_t^{t-1} \tag{4.30}$$

can be calculated. As the realization of $\boldsymbol{Y}_t$ is observed, the particular value

$$\tilde{\boldsymbol{\delta}}_t = \boldsymbol{y}_t - \boldsymbol{O}\hat{\boldsymbol{x}}_t^{t-1} \tag{4.31}$$

of the prediction error or *innovation* [98]

$$\boldsymbol{\delta}_t = \boldsymbol{Y}_t - \boldsymbol{O}\hat{\boldsymbol{x}}_t^{t-1} \tag{4.32}$$

is accessible [89]. Its variance evaluates to

$$\boldsymbol{\Sigma}_t = \mathrm{var}[\boldsymbol{\delta}_t] = \mathrm{var}[\boldsymbol{O}(\boldsymbol{X}_t - \hat{\boldsymbol{x}}_t^{t-1}) + \boldsymbol{\epsilon}_t] = \boldsymbol{O}\boldsymbol{P}_t^{t-1}\boldsymbol{O}^{\mathrm{T}} + \boldsymbol{R}\,. \tag{4.33}$$

The filter involves a time-update and a measurement-update step. The *time update*, Eqs. (4.25) and (4.26), is a one-step ahead model-based prediction of state $\hat{\boldsymbol{x}}_t^{t-1}$ and error covariance $\boldsymbol{P}_t^{t-1}$. It is important to note that the time update does not consider the observation at time t.

The *measurement update*, Eqs. (4.27) and (4.28), integrates the information of the current measurement $\boldsymbol{y}_t$. In order to derive Eq. (4.27), the joint probability density function of $\boldsymbol{X}_t$ and $\boldsymbol{\delta}_t$ conditioned on the observations $\{\boldsymbol{y}_1, \ldots, \boldsymbol{y}_t\}$ is needed. The corresponding covariance is [89, Eq. (6.26)]

$$\begin{aligned}
\mathrm{cov}(\boldsymbol{X}_t, \boldsymbol{\delta}_t \,|\, \boldsymbol{y}_1, \ldots, \boldsymbol{y}_t) &= \mathrm{cov}(\boldsymbol{X}_t, \boldsymbol{Y}_t - \boldsymbol{C}\hat{\boldsymbol{x}}_t^{t-1} \,|\, \boldsymbol{y}_1, \ldots, \boldsymbol{y}_t) \\
&= \mathrm{cov}(\boldsymbol{X}_t - \hat{\boldsymbol{x}}_t^{t-1}, \boldsymbol{Y}_t - \boldsymbol{C}\hat{\boldsymbol{x}}_t^{t-1} \,|\, \boldsymbol{y}_1, \ldots, \boldsymbol{y}_t) \\
&= \mathrm{cov}(\boldsymbol{X}_t - \hat{\boldsymbol{x}}_t^{t-1}, \boldsymbol{C}(\boldsymbol{X}_t - \hat{\boldsymbol{x}}_t^{t-1}) + \boldsymbol{\eta}_t \,|\, \boldsymbol{y}_1, \ldots, \boldsymbol{y}_t) \\
&= \mathrm{cov}(\boldsymbol{X}_t - \hat{\boldsymbol{x}}_t^{t-1}, \boldsymbol{X}_t - \hat{\boldsymbol{x}}_t^{t-1} \,|\, \boldsymbol{y}_1, \ldots, \boldsymbol{y}_t)\boldsymbol{C}^{\mathrm{T}} \\
&= \boldsymbol{P}_t^{t-1}\boldsymbol{C}^{\mathrm{T}}\,.
\end{aligned} \tag{4.34}$$

With the variance terms, Eqs. (4.26) and (4.33),

$$\begin{pmatrix} \boldsymbol{X}_t \\ \boldsymbol{\delta}_t \end{pmatrix} \Bigg| \boldsymbol{y}_1, \ldots, \boldsymbol{y}_t = \begin{pmatrix} \boldsymbol{X}_t \\ \boldsymbol{\delta}_t \end{pmatrix} \Bigg| \boldsymbol{y}_1, \ldots, \boldsymbol{y}_{t-1}, \boldsymbol{\delta}_t \tag{4.35}$$

$$\sim \mathcal{N}\left(\begin{bmatrix} \hat{\boldsymbol{x}}_t^{t-1} \\ \boldsymbol{0} \end{bmatrix}, \begin{bmatrix} \boldsymbol{P}_t^{t-1} & \boldsymbol{P}_t^{t-1}\boldsymbol{O}^{\mathrm{T}} \\ \boldsymbol{O}\boldsymbol{P}_t^{t-1} & \boldsymbol{\Sigma}_t \end{bmatrix} \right) \tag{4.36}$$

is the desired joint probability density function [89, Eq. (6.27)]. Equation (4.35) holds, since $\boldsymbol{\delta}_t$ contains all information of $\boldsymbol{y}_t$ not yet contained in $\hat{\boldsymbol{x}}_t^{t-1}$, cf., Eq. (4.32). Recalling Eq. (2.19), the expected value of $\boldsymbol{X}_t$ conditioned on $\tilde{\boldsymbol{\delta}}_t$, i.e., $\hat{\boldsymbol{x}}_t^t$, is

$$\begin{aligned}\hat{\boldsymbol{x}}_t^t &= \hat{\boldsymbol{x}}_t^{t-1} + \boldsymbol{P}_t^{t-1}\boldsymbol{O}^{\mathrm{T}}\boldsymbol{\Sigma}_t^{-1}\tilde{\boldsymbol{\delta}}_t \\ &= \hat{\boldsymbol{x}}_t^{t-1} + \boldsymbol{P}_t^{t-1}\boldsymbol{O}^{\mathrm{T}}\left(\boldsymbol{O}\boldsymbol{P}_t^{t-1}\boldsymbol{O}^{\mathrm{T}} + \boldsymbol{R}\right)^{-1}\tilde{\boldsymbol{\delta}}_t \\ &= \hat{\boldsymbol{x}}_t^{t-1} + \boldsymbol{K}_t\tilde{\boldsymbol{\delta}}_t\,.\end{aligned} \tag{4.37}$$

Thus, the Kalman gain $\boldsymbol{K}_t$ transforms the time-updated state estimate in its expected value conditioned on all observations including the newly acquired $\boldsymbol{y}_t$. Using Eqs. (2.21) and (4.24), the measurement update for the conditional error covariance

$$\begin{aligned}\boldsymbol{P}_t^t &= \mathrm{var}(\boldsymbol{X}_t \,|\, \boldsymbol{y}_1, \ldots, \boldsymbol{y}_t) \\ &= \mathrm{E}[(\boldsymbol{X}_t - \hat{\boldsymbol{x}}_t^t)(\boldsymbol{X}_t - \hat{\boldsymbol{x}}_t^t)^{\mathrm{T}} \,|\, \boldsymbol{y}_1, \ldots, \boldsymbol{y}_t] \\ &= \boldsymbol{P}_t^{t-1} - \boldsymbol{P}_t^{t-1}\boldsymbol{O}^{\mathrm{T}}\boldsymbol{\Sigma}_t^{-1}\boldsymbol{O}\boldsymbol{P}_t^{t-1} \\ &= \boldsymbol{P}_t^{t-1} - \boldsymbol{P}_t^{t-1}\boldsymbol{O}^{\mathrm{T}}(\boldsymbol{O}\boldsymbol{P}_t^{t-1}\boldsymbol{O}^{\mathrm{T}} + \boldsymbol{R})^{-1}\boldsymbol{O}\boldsymbol{P}_t^{t-1} \\ &= \boldsymbol{P}_t^{t-1} - \boldsymbol{K}_t\boldsymbol{O}\boldsymbol{P}_t^{t-1}\end{aligned} \tag{4.38}$$

is derived.

The Kalman filter is a forward recursion, which is independent of future observations and thus allows for online application. Another property of the filter is that Eqs. (4.26), (4.28), (4.29) do not involve observations, such that the (lag one) error covariance $\boldsymbol{P}_t^t$ and $\boldsymbol{P}_t^{t-1}$ and the Kalman gain $\boldsymbol{K}_t$ can be calculated before the filtering starts. With the computational power of contemporary computers, preparing $\boldsymbol{P}_t^{t-1}$, $\boldsymbol{P}_t^t$, and $\boldsymbol{K}_t$ beforehand is not of great interest anymore. However, for the application of the Kalman filter in the Apollo mission to the Moon in 1969, this was a nice advantage [100].

Prediction State and error covariance predictions are obtained by iterating Eqs. (4.25) and (4.26) until the desired time $\tilde{t} > t$ is reached using $\hat{\boldsymbol{x}}_t^t$ and $\boldsymbol{P}_t^t$ as initials.

4.4.2. Kalman smoother

The smoother is a recursion moving backwards in time. Thus, it is only applicable to a fully recorded time series containing, say, m samples. The *Kalman smoother* equations for $t = m, m-1, \ldots, 1$ are [32, 89, 99, 101]

$$\boldsymbol{J}_{t-1} = \boldsymbol{P}_{t-1}^{t-1}\boldsymbol{C}^{\mathrm{T}}\left(\boldsymbol{P}_t^{t-1}\right)^{-1}\,, \tag{4.39}$$

$$\hat{\boldsymbol{x}}_{t-1}^m = \hat{\boldsymbol{x}}_{t-1}^{t-1} + \boldsymbol{J}_{t-1}\left(\hat{\boldsymbol{x}}_t^m - \boldsymbol{C}\hat{\boldsymbol{x}}_{t-1}^{t-1}\right)\,, \tag{4.40}$$

$$\boldsymbol{P}_{t-1}^m = \boldsymbol{P}_{t-1}^{t-1} + \boldsymbol{J}_{t-1}\left(\boldsymbol{P}_t^m - \boldsymbol{P}_t^{t-1}\right)\boldsymbol{J}_{t-1}^{\mathrm{T}}\,. \tag{4.41}$$

In analogy to $\boldsymbol{K}_t$ [→ Eq. (4.29)], $\boldsymbol{J}_t$ is the smoother gain. The final estimate $\hat{\boldsymbol{x}}_m^m$ and its covariance $\boldsymbol{P}_m^m$ provide the initial values for the smoother. The recursion

$$\boldsymbol{P}_{t-1,t-2}^m = \boldsymbol{P}_{t-1}^{t-1}\boldsymbol{J}_{t-2}^{\mathrm{T}} + \boldsymbol{J}_{t-1}\left(\boldsymbol{P}_{t,t-1}^m - \boldsymbol{C}\boldsymbol{P}_{t-1}^{t-1}\right)\boldsymbol{J}_{t-2}^{\mathrm{T}}, \quad t = m, m-1, \ldots, 2 \tag{4.42}$$

with initial value

$$\boldsymbol{P}_{m,m-1}^m = (\boldsymbol{I} - \boldsymbol{K}_m\boldsymbol{O})\,\boldsymbol{C}_m\boldsymbol{P}_{m-1}^{m-1} \tag{4.43}$$

is the so-called *lag-one covariance smoother* [32, 89].

4.5. Maximum-likelihood estimation of state-space model parameters by the expectation-maximization algorithm

The parameters in the SSM can be estimated in an iterative manner by an MLE which is constructed using the EM algorithm. Since the observation matrix $\boldsymbol{O}$ is fixed to the identity in order to resolve the gauge invariance in the SSM [→ Sec. 4.1.3], the parameter vector $\boldsymbol{\Theta} = (\boldsymbol{\mu}_0, \boldsymbol{\Sigma}_0, \boldsymbol{C}, \boldsymbol{R}, \boldsymbol{Q})$ remains for estimation. The discussion follows [32].

The joint probability density function of m samples from the SSM is

$$f[(\boldsymbol{x}, \boldsymbol{y}), \boldsymbol{\Theta}] = f[\boldsymbol{x}_0, (\boldsymbol{\mu}_0, \boldsymbol{\Sigma}_0)] \prod_{t=1}^{m} f[\boldsymbol{x}_t, (\boldsymbol{C}, \boldsymbol{Q})] \prod_{t=1}^{m} f[\boldsymbol{y}_t, (\boldsymbol{O}, \boldsymbol{R})]\,. \tag{4.44}$$

Since the driving and observational noise in the SSM is Gaussian, the log-likelihood function considered as a function of $\boldsymbol{\Theta}$ reads

$$\begin{aligned}
\mathcal{L}(\boldsymbol{\Theta}) = &-\frac{1}{2}\log|\boldsymbol{\Sigma}_0| - \frac{1}{2}(\boldsymbol{x}_0 - \boldsymbol{\mu}_0)^{\mathrm{T}}\boldsymbol{\Sigma}_0^{-1}(\boldsymbol{x}_0 - \boldsymbol{\mu}_0) \\
&-\frac{m}{2}\log|\boldsymbol{Q}| - \frac{1}{2}\sum_{t=1}^{m}(\boldsymbol{x}_t - \boldsymbol{C}\boldsymbol{x}_{t-1})^{\mathrm{T}}\boldsymbol{Q}^{-1}(\boldsymbol{x}_t - \boldsymbol{C}\boldsymbol{x}_{t-1}) \\
&-\frac{m}{2}\log|\boldsymbol{R}| - \frac{1}{2}\sum_{t=1}^{m}(\boldsymbol{y}_t - \boldsymbol{O}\boldsymbol{x}_t)^{\mathrm{T}}\boldsymbol{R}^{-1}(\boldsymbol{y}_t - \boldsymbol{O}\boldsymbol{x}_t)\,.
\end{aligned} \tag{4.45}$$

Thus, by denoting the trace of a matrix by $\mathrm{tr}(\cdot)$, the conditional expected value [→ Eq. (4.19)] of the likelihood function

$$\begin{aligned}
\tilde{\mathcal{L}}(\boldsymbol{\Theta}) = &-\frac{1}{2}\log|\boldsymbol{\Sigma}_0| - \frac{1}{2}\,\mathrm{tr}\left\{\boldsymbol{\Sigma}_0^{-1}\left[\boldsymbol{P}_t^m + (\hat{\boldsymbol{x}}_0^m - \boldsymbol{\mu})\,(\hat{\boldsymbol{x}}_0^m - \boldsymbol{\mu})^{\mathrm{T}}\right]\right\} \\
&-\frac{m}{2}\log|\boldsymbol{Q}| - \frac{1}{2}\,\mathrm{tr}\left\{\boldsymbol{Q}^{-1}\left[\boldsymbol{\gamma} - \boldsymbol{\beta}\boldsymbol{C}^{\mathrm{T}} - \boldsymbol{C}\boldsymbol{\beta}^{\mathrm{T}} + \boldsymbol{C}\boldsymbol{\alpha}\boldsymbol{C}^{\mathrm{T}}\right]\right\} \\
&-\frac{m}{2}\log|\boldsymbol{R}| \\
&-\frac{1}{2}\,\mathrm{tr}\left\{\boldsymbol{R}^{-1}\sum_{t=1}^{m}\left[(\boldsymbol{y}_t - \boldsymbol{O}\hat{\boldsymbol{x}}_t^m)\,(\boldsymbol{y}_t - \boldsymbol{O}\hat{\boldsymbol{x}}_t^m)^{\mathrm{T}} + \boldsymbol{O}\boldsymbol{P}_t^m\boldsymbol{O}^{\mathrm{T}}\right]\right\},
\end{aligned} \tag{4.46}$$

with

$$\boldsymbol{\alpha} = \sum_{t=1}^{m} \left[\boldsymbol{P}_{t-1}^{m} + \hat{\boldsymbol{x}}_{t-1}^{m} (\hat{\boldsymbol{x}}_{t-1}^{m})^{\mathrm{T}} \right] , \tag{4.47}$$

$$\boldsymbol{\beta} = \sum_{t=1}^{m} \left[\boldsymbol{P}_{t,t-1}^{m} + \hat{\boldsymbol{x}}_{t}^{m} (\hat{\boldsymbol{x}}_{t-1}^{m})^{\mathrm{T}} \right] , \tag{4.48}$$

$$\boldsymbol{\gamma} = \sum_{t=1}^{m} \left[\boldsymbol{P}_{t}^{m} + \hat{\boldsymbol{x}}_{t}^{m} (\hat{\boldsymbol{x}}_{t}^{m})^{\mathrm{T}} \right] , \tag{4.49}$$

is derived. Based on $\boldsymbol{\Theta}^{\varsigma}$, the quantities $\hat{\boldsymbol{x}}_{t}^{m}$, $\boldsymbol{P}_{t}^{m}$, and $\boldsymbol{P}_{t,t-1}^{m}$ are obtained from the Kalman smoother [→ Eqs. (4.40) and (4.41)] and lag-one covariance smoother [→ Eq. (4.42)]. Advantage is taken of the fact that covariance matrices are symmetric and thus self-adjoint. The parameter update equations are obtained using partial derivatives of Eq. (4.46) with respect to each parameter. The calculation is recapped in App. B.2. The update equations are derived as

$$\boldsymbol{C}^{(\varsigma+1)} = \boldsymbol{\beta}\boldsymbol{\alpha}^{-1} , \tag{4.50}$$

$$\boldsymbol{Q}^{(\varsigma+1)} = \frac{1}{m} \left(\boldsymbol{\gamma} - \boldsymbol{\beta}\boldsymbol{\alpha}^{-1}\boldsymbol{\beta}^{\mathrm{T}} \right) , \tag{4.51}$$

$$\boldsymbol{R}^{(\varsigma+1)} = \frac{1}{m} \sum_{t=1}^{m} \left[(\boldsymbol{y}_t - \boldsymbol{O}\hat{\boldsymbol{x}}_{t}^{m}) (\boldsymbol{y}_t - \boldsymbol{O}\hat{\boldsymbol{x}}_{t}^{m})^{\mathrm{T}} + \boldsymbol{O}\boldsymbol{P}_{t}^{m}\boldsymbol{O}^{\mathrm{T}} \right] . \tag{4.52}$$

Mean and covariance of the initial value $\boldsymbol{x}_0$ are updated as $\boldsymbol{\mu}_0^{\varsigma+1} = \hat{\boldsymbol{x}}_0^m$ and $\boldsymbol{\Sigma}_0^{\varsigma+1} = \boldsymbol{P}_0^m$.

4.5.1. Initialization and convergence

For the first iteration of the EM algorithm, the SSM is initialized as follows. The mean of the time series $\boldsymbol{y}_t$ defines $\boldsymbol{\mu}_0^1$, whereas $\boldsymbol{\Sigma}_0^1$ can be set to a reasonable baseline value [32]. The remaining parameters $\boldsymbol{C}$, $\boldsymbol{Q}$, and $\boldsymbol{R}$ can be initialized unrestricted, as long as they yield a stationary SSM. As discussed in Sec. 4.3, convergence is determined by the relative change of $\boldsymbol{C}$ [→ Eq. (4.50)], quantified by

$$\kappa = \max_{i,j} \left[\frac{(\boldsymbol{C}^{\varsigma})_{ij} - (\boldsymbol{C}^{\varsigma-1})_{ij}}{(\boldsymbol{C}^{\varsigma})_{ij}} \right] , \quad i,j = 1, \ldots, kp . \tag{4.53}$$

4.5.2. Constrained update equations for the embedded VAR process

The Kalman filter and smoother base on the VAR[1] model. As the Kalman filter provides the conditional expected values needed in the EM algorithm, a VAR[p] model must be reformulated as VAR[1] in order to estimate its parameters. According to Sec. 4.1.1, this is unproblematic in general. However, this reformulation implies a certain structure of $\boldsymbol{C}$ and $\boldsymbol{Q}$. With the next proposition, it is proven, that this structure is maintained by the update equations of the EM algorithm.

Proposition 4.5.1. *The structure of* $\boldsymbol{C}$ *and* $\boldsymbol{Q}$ *resulting from the reformulation of a VAR[p] as a VAR[1] is maintained by the parameter update equations of the EM algorithm as given in Eqs.* (4.50) *and* (4.51)*.*

Proof. Constrained optimization is carried out by the use of Lagrangian multipliers. The Lagrangian multipliers of the elements of the transition matrix C_{ij} are denoted λ_{ij}, the multipliers for the elements of the covariance matrix Q_{ij} are denoted ω_{ij}, with $i, j = 1, \ldots, kp$. In case C_{ij} or Q_{ij} refers to an unconstrained element, λ_{ij} or ω_{ij}, respectively, are set to zero. Constraints are formulated as $C_{ij} - \phi_{ij} = 0$ and $Q_{ij} - \psi_{ij} = 0$. The constrained elements of $\boldsymbol{C}$ are either zero or one, the constrained elements of $\boldsymbol{Q}$ are all zero. Thus, ϕ_{ij} and ψ_{ij} are also either zero or one, according to the desired value of C_{ij} and Q_{ij}. From the unconstrained expected value of the log-likelihood function as given in Eq. (4.46), the expected value of the constrained log-likelihood function

$$\tilde{\mathcal{L}}_{\mathrm{n}} = \tilde{\mathcal{L}} + \sum_{i,j=1}^{kp} \lambda_{ij}(C_{ij} - \phi_{ij}) + \sum_{i,j=1}^{kp} \omega_{ij}(Q_{ij} - \psi_{ij}) \tag{4.54}$$

is derived. Its partial derivative with respect to $\boldsymbol{Q}$ is

$$\begin{aligned} \frac{\partial \tilde{\mathcal{L}}_{\mathrm{n}}}{\partial \boldsymbol{Q}} &= \frac{\partial \tilde{\mathcal{L}}}{\partial \boldsymbol{Q}} + \frac{\partial}{\partial \boldsymbol{Q}} \sum_{i,j} \omega_{ij}(Q_{ij} - \psi_{ij}) \\ &= \frac{\partial \tilde{\mathcal{L}}}{\partial \boldsymbol{Q}} + \sum_{i,j} \omega_{ij} \hat{\boldsymbol{e}}_{ij} \\ &= \frac{\partial \tilde{\mathcal{L}}}{\partial \boldsymbol{Q}} + \boldsymbol{\Omega} \\ &\stackrel{!}{=} 0\,. \end{aligned} \tag{4.55}$$

It is shown in App. B.2.2, Eq. (B.31) that

$$\frac{\partial \tilde{\mathcal{L}}}{\partial \boldsymbol{Q}} = -\frac{1}{2}\left(m\boldsymbol{Q}^{-1} - \boldsymbol{Q}^{-1}\boldsymbol{F}^{\mathrm{T}}\boldsymbol{Q}^{-1}\right), \tag{4.56}$$

where $\boldsymbol{F}$ is defined as

$$\boldsymbol{F} = \boldsymbol{\gamma} - \boldsymbol{\beta}\boldsymbol{C}^{\mathrm{T}} - \boldsymbol{C}\boldsymbol{\beta}^{\mathrm{T}} + \boldsymbol{C}\boldsymbol{\alpha}\boldsymbol{C}^{\mathrm{T}}\,. \tag{4.57}$$

By the use of Eq. (4.56), Eq. (4.55) becomes

$$-\frac{1}{2}\left(m\boldsymbol{Q}^{-1} - \boldsymbol{Q}^{-1}\boldsymbol{F}^{\mathrm{T}}\boldsymbol{Q}^{-1}\right) + \boldsymbol{\Omega} = 0\,. \tag{4.58}$$

Multiplication by $2\boldsymbol{Q}$ from the left and by $\boldsymbol{Q}$ from the right yields

$$-\left(m\boldsymbol{Q} - \boldsymbol{F}\right) + 2\boldsymbol{Q}\boldsymbol{\Omega}\boldsymbol{Q} = 0\,. \tag{4.59}$$

The first term arises from the unconstrained case, such that equating coefficients with the unconstrained parameter update equation stated in Eq. (4.51) leads to the constrained update equation

$$\begin{aligned}\boldsymbol{Q}_{\mathrm{n}}^{\varsigma+1} &= \frac{1}{m}\left(\boldsymbol{\gamma} - \boldsymbol{\beta}\boldsymbol{\alpha}^{-1}\boldsymbol{\beta}^{\mathrm{T}}\right) + \frac{2}{m}\boldsymbol{Q}\boldsymbol{\Omega}\boldsymbol{Q} \\ &= \boldsymbol{Q}^{\varsigma+1} + \frac{2}{m}\boldsymbol{Q}\boldsymbol{\Omega}\boldsymbol{Q}\,.\end{aligned} \tag{4.60}$$

The derivatives

$$\frac{\partial\tilde{\mathcal{L}}_{\mathrm{n}}}{\partial\omega_{ij}} = 0\,, \quad \text{for } i,j = 1,\ldots,kp \tag{4.61}$$

determine the constrained elements of $\boldsymbol{Q}$ to zero, such that

$$\boldsymbol{Q} = \begin{pmatrix}\boxtimes & \mathbf{0}\\ \mathbf{0} & \mathbf{0}\end{pmatrix} \tag{4.62}$$

results, where $\boxtimes$ indicates nonzero elements. By virtue of the form of $\boldsymbol{Q}$

$$\boldsymbol{Q}\boldsymbol{\Omega}\boldsymbol{Q} = \begin{pmatrix}\boxtimes & \mathbf{0}\\ \mathbf{0} & \mathbf{0}\end{pmatrix}\cdot\begin{pmatrix}\mathbf{0} & \boxtimes\\ \boxtimes & \boxtimes\end{pmatrix}\cdot\begin{pmatrix}\boxtimes & \mathbf{0}\\ \mathbf{0} & \mathbf{0}\end{pmatrix} = \mathbf{0}\,. \tag{4.63}$$

Thus, Eq. (4.51) and Eq. (4.60) are equivalent, such that the unconstrained update equation already maintains the structure of $\boldsymbol{Q}$. The same argument applies to the update equation for $\boldsymbol{C}$. □

Due to numerical inaccuracy, the constrained parts of $\boldsymbol{C}$ and $\boldsymbol{Q}$ might nevertheless differ from their desired values. It is therefore advisable to reset these elements after each parameter update.

4.6. Reducing the computational complexity of the EM algorithm

As proposed in this thesis, the runtime of the EM algorithm is reduced by parallelization as well as by exploiting fixed-point equations for the Kalman filter and smoother gain. Both approaches are presented in the following.

4.6.1. Parallelization

The parameter update equations stated by Eqs. (4.50) – (4.52) only depend on the sum of $\boldsymbol{x}_t^m$ and $\boldsymbol{P}_t^m$ either directly or through Eqs. (4.47) – (4.49). Each sum occurring in Eqs. (4.47) – (4.49) can be divided in, say, u sub-sums. For each sub-sum i, an individual Kalman filter and smoother can obtain $\boldsymbol{x}_{t,i}^{m/u}$ and $\boldsymbol{P}_{t,i}^{m/u}$ in parallel, where

the index $i = 1, \ldots, u$ referes to the i-th sub-sum. From the intermediate results $\boldsymbol{\alpha}_i$, $\boldsymbol{\beta}_i$, $\boldsymbol{\gamma}_i$, the corresponding full-data quantities

$$\boldsymbol{\alpha} = \sum_{i=1}^{u} \boldsymbol{\alpha}_i \,, \quad \boldsymbol{\beta} = \sum_{i=1}^{u} \boldsymbol{\beta}_i \,, \quad \boldsymbol{\gamma} = \sum_{i=1}^{u} \boldsymbol{\gamma}_i \tag{4.64}$$

are rapidly calculated. The same argument applies to Eq. (4.52), directly. Most of the runtime of the EM algorithm is spent in the Kalman filter and smoother. Thus, executing them in parallel on a computer system with v cores decreases the runtime of the entire algorithm by the factor $\min(u, v)$.

The data processed by a sub-sum is called *panel* in the following. Repeated measurements are a natural candidate for panels. In that case, repetitions can be analyzed in parallel and collated afterwards in order to obtain the parameter estimates, which fit the entire data set.

Splitting a long time series in u shorter ones which are then processed in parallel offers an additional approach to take advantage of parallelization. The Kalman filter, however, needs some time to converge for each of the u panels. Thus, some of the information present in early recordings of each panel is wasted. Fortunately, as an afterthought of the second optimization, this drawback is eliminated as soon as the panels are long enough for the filter to converge at all [34].

4.6.2. Fixed points of the Kalman gains

As matrix inversion is computational complex, this optimization approach aims at avoiding matrix inversions in the Kalman filter and smoother gain

$$\boldsymbol{K}_t = \boldsymbol{P}_t^{t-1} \boldsymbol{O}^{\mathrm{T}} \left(\boldsymbol{O} \boldsymbol{P}_t^{t-1} \boldsymbol{O}^{\mathrm{T}} + \boldsymbol{R} \right)^{-1} , \tag{4.65}$$

$$\boldsymbol{J}_{t-1} = \boldsymbol{P}_{t-1}^{t-1} \boldsymbol{C}^{\mathrm{T}} \left(\boldsymbol{P}_t^{t-1} \right)^{-1} . \tag{4.66}$$

Both gains depend on time by $\boldsymbol{P}_t^{t-1}$ and $\boldsymbol{P}_t^t$. However, for a stationary process, the (lag-one) error covariance does not change with time, making their update equations (4.26) and (4.28) fixed-point equations. In literature, this property is used e.g., to establish the asymptotic distribution of the maximum-likelihood estimator [89]. In this section, the fixed-point equations are exploited to reduce the computational complexity of the EM algorithm. After engaging the Kalman filter, the (lag-one) error covariance changes its value with each time step until its fixed-point is reached, such that $\boldsymbol{P}_t^t = \boldsymbol{P}_{t-1}^{t-1}$ and $\boldsymbol{P}_t^m = \boldsymbol{P}_{t-1}^m$ holds.

Since the smoother gain is a function of the error covariance of the filter, it is at this point fully determined as

$$\boldsymbol{J} = \boldsymbol{P}_t^t \boldsymbol{C}^{\mathrm{T}} (\boldsymbol{P}_t^{t-1})^{-1} . \tag{4.67}$$

The update equation for the error covariance of the smoother than reads

$$\boldsymbol{P}_t^m = \boldsymbol{P}_t^t + \boldsymbol{J} (\boldsymbol{P}_t^m - \boldsymbol{P}_t^{t-1}) \boldsymbol{J}^{\mathrm{T}} . \tag{4.68}$$

Using the Kronecker product $\otimes$ and the vec operation [92], Eq. (4.68) is rearranged to

$$\boldsymbol{P}_t^m - \boldsymbol{J}\boldsymbol{P}_t^m\boldsymbol{J}^{\mathrm{T}} = \boldsymbol{P}_t^t - \boldsymbol{J}\boldsymbol{P}_t^{t-1}\boldsymbol{J}^{\mathrm{T}} \tag{4.69}$$

$$(\boldsymbol{I} - \boldsymbol{J}\otimes\boldsymbol{J})\,\mathrm{vec}(\boldsymbol{P}_t^m) = \mathrm{vec}(\boldsymbol{P}_t^t - \boldsymbol{J}\boldsymbol{P}_t^{t-1}\boldsymbol{J}^{\mathrm{T}})\,, \tag{4.70}$$

such that the explicit expression

$$\mathrm{vec}(\boldsymbol{P}_t^m) = (\boldsymbol{I} - \boldsymbol{J}\otimes\boldsymbol{J})^{-1}\,\mathrm{vec}(\boldsymbol{P}_t^t - \boldsymbol{J}\boldsymbol{P}_t^{t-1}\boldsymbol{J}^{\mathrm{T}})\,. \tag{4.71}$$

is found. Along the same line, the explicit expression

$$\mathrm{vec}(\boldsymbol{P}_{t,t-1}^m) = (\boldsymbol{I} - \boldsymbol{J}\otimes\boldsymbol{J})^{-1}\,\mathrm{vec}\left[(\boldsymbol{I} - \boldsymbol{J}\boldsymbol{C})\boldsymbol{P}_t^t\boldsymbol{J}^{\mathrm{T}}\right] \tag{4.72}$$

for the lag-one error covariance is obtained [34].

4.6.3. Optimized expectation-maximization algorithm

The following sequence constitutes the EM algorithm taking advantage of the run time optimization introduced in the last two sections [34].

0. Initialize the Kalman filter.

1. Iterate

$$\begin{aligned}\boldsymbol{P}_t^{t-1} &= \boldsymbol{C}\boldsymbol{P}_{t-1}^{t-1}\boldsymbol{C}^{\mathrm{T}} + \boldsymbol{Q}\,,\\ \boldsymbol{P}_t^t &= \boldsymbol{P}_t^{t-1} - \boldsymbol{K}_t\boldsymbol{O}\boldsymbol{P}_t^{t-1}\,,\\ \boldsymbol{K}_t &= \boldsymbol{P}_t^{t-1}\boldsymbol{O}^{\mathrm{T}}\left(\boldsymbol{O}\boldsymbol{P}_t^{t-1}\boldsymbol{O}^{\mathrm{T}} + \boldsymbol{R}\right)^{-1}\,.\end{aligned} \tag{4.73}$$

   until convergence starting from $\boldsymbol{P}_0^0 = \boldsymbol{P}_0^n$ as of the last EM iteration.

2. Calculate the smoother gain and the error covariance of the smoother by Eqs. (4.67), (4.71), (4.72). As they are data independent, their results apply to all panels.

3. Filter the observations, possibly for all panels in parallel, by calculating

$$\hat{\boldsymbol{x}}_t^t = \boldsymbol{K}\boldsymbol{y}_t + (\boldsymbol{I} - \boldsymbol{K}\boldsymbol{O})\boldsymbol{C}\hat{\boldsymbol{x}}_{t-1}^{t-1}\,,\quad t = 1\ldots n\,, \tag{4.74}$$

$$\hat{\boldsymbol{x}}_{t-1}^m = \boldsymbol{J}\hat{\boldsymbol{x}}_t^m + (\boldsymbol{I} - \boldsymbol{J}\boldsymbol{O})\hat{\boldsymbol{x}}_{t-1}^{t-1}\,,\quad t = n\ldots 1\,. \tag{4.75}$$

   Initialize $\hat{\boldsymbol{x}}_0^0$ to $\hat{\boldsymbol{x}}_0^n$ from the last EM iteration.

4. Evaluate

$$\boldsymbol{\alpha} = m\boldsymbol{P}_{t-1}^m + \sum_{t=1}^{m}\left[\hat{\boldsymbol{x}}_{t-1}^m(\hat{\boldsymbol{x}}_{t-1}^m)^{\mathrm{T}}\right]\,, \tag{4.76}$$

$$\boldsymbol{\beta} = m\boldsymbol{P}_{t,t-1}^m + \sum_{t=1}^{m}\left[\hat{\boldsymbol{x}}_t^m(\hat{\boldsymbol{x}}_{t-1}^m)^{\mathrm{T}}\right]\,, \tag{4.77}$$

$$\boldsymbol{\gamma} = m\boldsymbol{P}_t^m + \sum_{t=1}^{m}\left[\hat{\boldsymbol{x}}_t^m(\hat{\boldsymbol{x}}_t^m)^{\mathrm{T}}\right]\,, \tag{4.78}$$

and Eq. (4.64) if applicable, in order to finally update $\boldsymbol{C}$, $\boldsymbol{Q}$, and $\boldsymbol{R}$ through Eqs. (4.50) – (4.52).

5. Repeat 1. to 4. until convergence.

4.7. Application to simulated data

In this section, the performance of the optimized EM algorithm is demonstrated. To this end, the conventional algorithm [32, 89] as well as the algorithm with the here proposed optimizations are implemented [34].† The runtimes of both algorithms are than compared.

The accuracy of parameter estimates of the optimized algorithm is assessed by means of their spectral representation as well as by repeated estimations. Calculation of confidence bounds for parameter estimates would also be possible using the second derivative of the complete-data likelihood. However, this is already reported elsewhere [33, 102]. The overall view yields that the implementation is fast, accurate, and correct.

4.7.1. Runtime improvements

In a first simulation study, the runtime of three different implementations of the EM algorithm is compared. Firstly, the conventional EM algorithm is implemented in Matlab, secondly in C++. Thirdly, the optimized EM algorithm is implemented in C++. That way, the effect of the different programming languages as well as of the proposed optimizations on the runtime can be studied separately.

Three time series are used to benchmark the runtime which are realizations of a three-dimensional VAR[2] with transients discarded. The time series have 1000, 5000, and 30 000 data points, respectively. To each time series, a SSM is fitted. Each SSM includes a three-dimensional VAR of order 3, 5, and 10, respectively. All calculations are performed on two 2.93 GHz Quad-Core Intel Xeon CPUs with 32 GiB of computer memory in total. Algorithms are rated by the average time spent for one EM iteration.

Runtimes of conventional and optimized EM algorithm In Fig. 4.2, the average runtimes of all EM implementations are plotted against the number of data points of the analyzed time series. The performance of the conventional EM algorithm is comparable for the two programming languages. Thus, the effect of the programming language on the runtime can be considered negligible. Yet, the conventional algorithm is outperformed by the optimized algorithm by a runtime that is reduced by two orders of magnitude. This is a major improvement, which allows to analyze data sets which hence have been too large [33].

†The optimized EM algorithm can be freely obtained from https://github.com/wmader/fdmb.

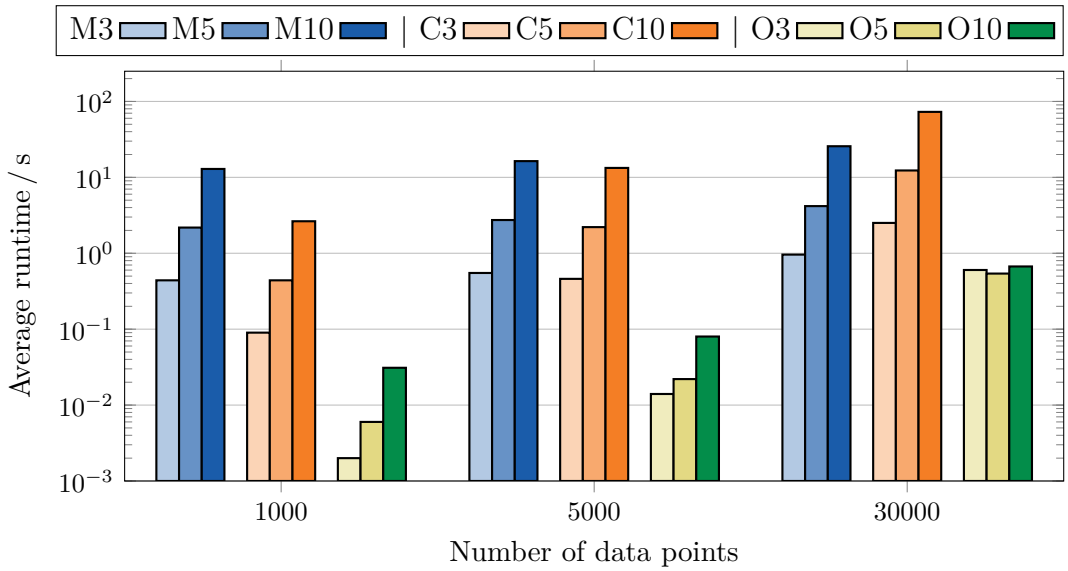

Figure 4.2.: Overview of the runtime of the different EM implementations. The results of the Matlab implementation are shown in shades of blue, the results of the C++ implementation of the conventional EM algorithm in shades of orange, and in shades of green, the results of the optimized C++ implementation are presented. The shades of colors encode from light to dark the process order 3, 5, and 10 of the fitted SSM.

4.7.2. Accuracy of parameter estimates

Two simulation studies addressing the quality of the parameter estimates obtained by the implementation of the optimized EM algorithm are carried out. In the first study, the power spectral density function calculated from both the true VAR parameters and the VAR parameters estimated in the SSM are compared. In the second study, the accuracy of the actually estimated parameter values is investigated by means of repeated estimations.

Power spectral density function of the VAR process

The power spectral density function, or simply power spectrum, $\boldsymbol{H}(\omega)$ describes the distribution of frequencies contained in a stationary random process. In particular, $\boldsymbol{H}(\omega)\,\mathrm{d}\omega$ denotes the power of the process in the infinitesimal frequency bin $[\omega, \omega + \mathrm{d}\omega]$ [103]. The power spectrum of a VAR process

$$\boldsymbol{H}(\omega) = \frac{1}{2\pi}\boldsymbol{c}\cdot\boldsymbol{Q}\cdot\boldsymbol{c}^*, \quad \text{widh} \quad \boldsymbol{c} = \left(\boldsymbol{I} - \sum_{\tau=1}^{p}\boldsymbol{C}(\tau)e^{-iw\tau}\right)^{-1}, \tag{4.79}$$

is determined by its transition matrices $\boldsymbol{C}(\tau)$ and the covariance matrix of the driving noise $\boldsymbol{Q}$ [91]. The conjugate transposed matrix of $\boldsymbol{c}$ is denoted $\boldsymbol{c}^*$. In the simulation study, the true values of $\boldsymbol{C}$ and $\boldsymbol{Q}$ are known. Thus, the true spectrum and the

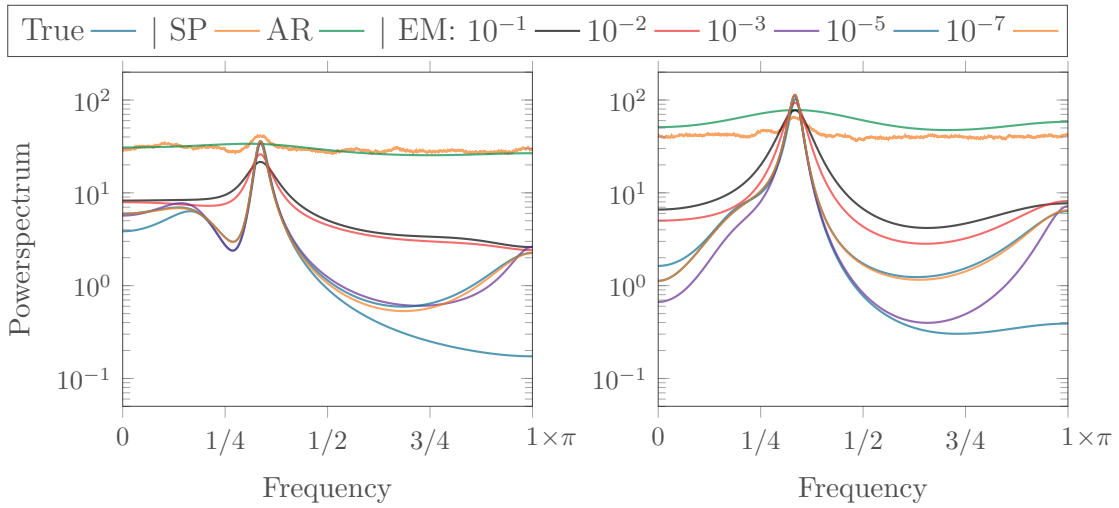

(a) First process component

(b) Second process component

Figure 4.3.: True and estimated power spectra. Shown in blue is the true spectrum. The smoothed periodogram is shown in orange. The spectrum shown in green is calculated from the parameters of a fitted VAR model. The remaining spectra are calculated from parameters estimated in the SSM by the optimized EM algorithm for value $\{10^{-1}, 10^{-2}, 10^{-3}, 10^{-5}, 10^{-7}\}$ of the convergence criterion κ.

spectrum calculated from estimated parameters can be compared. For this study, a two-dimensional VAR[3]

$$\begin{aligned} \boldsymbol{C}(1) &= \begin{pmatrix} 0.9 & 0 \\ 0.35 & 0.7 \end{pmatrix}, & \boldsymbol{C}(2) &= \begin{pmatrix} -0.5 & 0.1 \\ 0.2 & -0.3 \end{pmatrix}, \\ \boldsymbol{C}(3) &= \begin{pmatrix} 0 & 0.15 \\ -0.25 & -0.4 \end{pmatrix}, & \boldsymbol{Q} &= \begin{pmatrix} 1 & 0 \\ 0 & 1 \end{pmatrix} \end{aligned} \tag{4.80}$$

is considered. After discarding 10^4 data points from a realization of the process in order to avoid transient effects, a time series with $m = 10^3$ data points is obtained. Gaussian noise is added to the time series in order model additive observational noise. The variance of the observational noise is chosen such that the signal-to-noise ratio (SNR) is 1/8 for both process components.

In Fig. 4.3, the true and estimated spectra of both process components are compared. The true (True) spectra without observational noise are calculated from the true process parameters and are used as reference for the estimates. A model-free estimator of the spectrum is the smoothed periodogram. Since this estimator does not take into account observation noise, its estimates (AR) are mostly flat due to the large amount of observational noise. As the VAR model does also not include observation noise, the spectrum calculated from fitted VAR parameters (AR) is also mostly flat. For an increasingly strict convergence criterion $\kappa \in \{10^{-1}, 10^{-2}, 10^{-3}, 10^{-5}, 10^{-7}\}$, cf.,

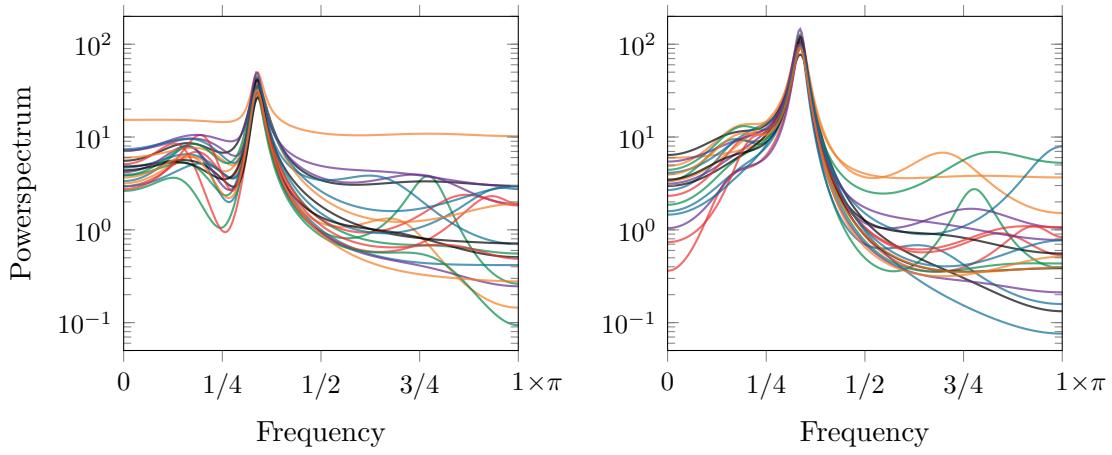

(a) First process component

(b) Second process component

Figure 4.4.: Repeated spectral estimation from different realizations of a single process.

Eq. (4.53), the spectra of both process components calculated from maximum-likelihood SSM parameter estimates converge to the true spectrum. The peaks, the most informed regions in a spectrum, are well recovered for all values of κ.

Parameter estimates depend on the realization of the process. In a second study, for each of 20 different realizations of the process defined by Eq. (4.80), the spectrum is estimated in the SSM at $\kappa = 10^{-5}$. Estimated spectra are shown in Fig. 4.4. Frequency regions with large power are well determined by the data and are invariant under process realizations. Estimated parameters are mostly determined by the contributions of these frequencies to the time series. Thus, parameter estimates are such that the estimated and true spectrum match well in these frequency regions. Consequently, for all process realizations, the peaks of the spectrum are correctly identified, but especially at high frequencies, the estimated spectra depend on the realization.

Repeated estimation with varying initial conditions

The accuracy of the optimized EM implementation is studied by estimating parameters multiple times from one time series starting from random parameter values. To this end, the parameter vector $\boldsymbol{\Theta} = \{\boldsymbol{\mu}_0, \boldsymbol{\Sigma}_0, \boldsymbol{C}, \boldsymbol{R}, \boldsymbol{Q}\}$ of a two dimensional SSM with process order two is estimated from a realization of the same model. Thus, the model is the correct one for the fitted data such that true and estimated parameter values are directly comparable. The first 500 samples of the time-series which is used for fitting is depicted in Fig. 4.5. The SNR is one for both components. Convergence is defined by $\kappa \in \{10^{-5}, 10^{-7}\}$. For both value of κ, 100 fits are performed.

For $\kappa = 10^{-7}$, the estimated values of $\boldsymbol{C}$ are shown in Fig. 4.6 (a). The 100 repeated fits yield two distinct sets of parameter estimates. The first is on spot with the true parameter values. This solution is termed *correct* in the figure legend and is

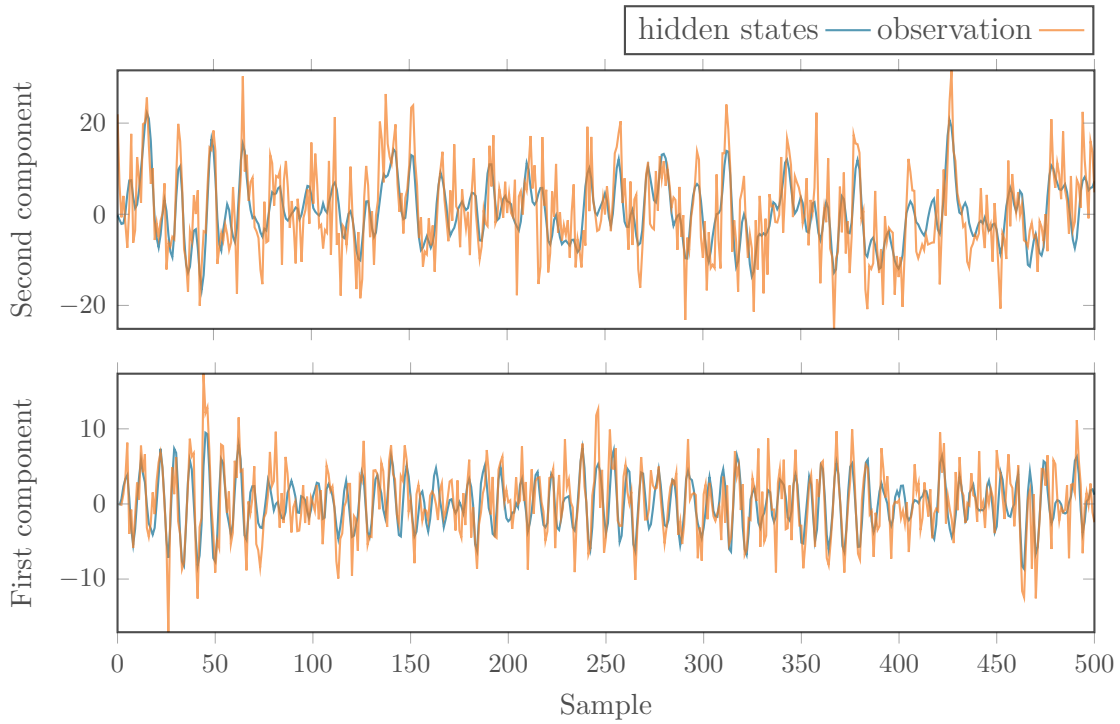

Figure 4.5.: Realization of the SSM from which the parameter estimates presented in Fig. 4.6 are obtained. The hidden states are depicted in blue. Parameters are estimated from their noisy observations plotted in orange.

plotted as blue circles. The estimates of the second set are incompatible with the true parameter values. This solution is referred to as *concurrent* shown by orange squares. Analogously, the results for $\boldsymbol{Q}$ are presented in Fig. 4.6 (b), those for $\boldsymbol{R}$ are presented in Fig. 4.6 (c). The concurrent solution for q_{11} is much larger than its true value in order to meet the variance of the data.

Even though the estimates of the concurrent solution are incompatible with the true values, the associated spectrum resembles the main features of the true one. At $\kappa = 10^{-5}$, the correct solution is found in about 75 % of all fits. This percentage increases with decreasing κ, such that at $\kappa = 10^{-7}$ the correct solution is found in 90 % of all fits. As with all optimization problems, the convergence criterion is a trade-off between time and accuracy. The EM algorithm is no exception.

The EM algorithm guarantees to increase the likelihood of the parameter estimates with each iteration until a fixed-point of the likelihood function is reached. However, the EM algorithm is not guaranteed to converge to the global maximum of the likelihood function [104]. By a multi-start approach, the parameter space is sampled, such that local maxima and at best the global maximum are found. The maximum with largest likelihood repeatedly found by multi-start fitting can be assumed to be the global maximization, yielding an estimate of the true parameter values [105]. In this regard, the algorithm achieves accurate parameter estimates.

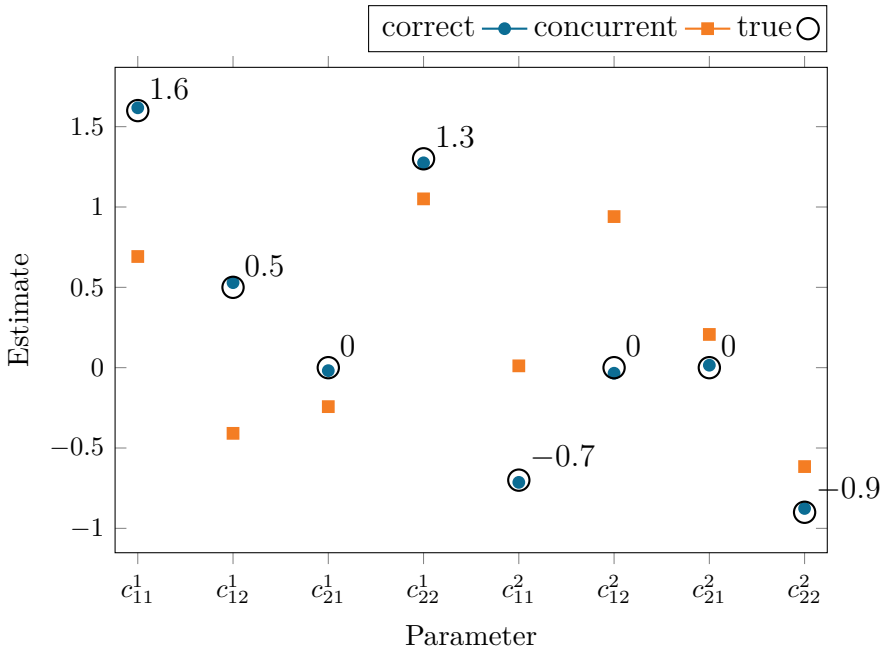

(a) Estimates of $\boldsymbol{C}(1)$ and $\boldsymbol{C}(2)$

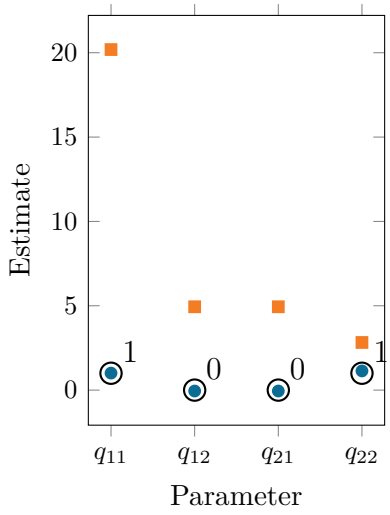

(b) Estimate of $\boldsymbol{Q}$

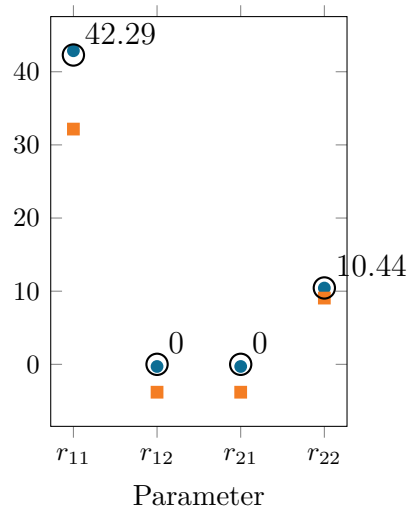

(c) Estimate of $\boldsymbol{R}$

Figure 4.6.: Average parameter estimates from 100 repetitions at $\kappa = 10^{-7}$. Standard errors are smaller than plot marks. The elements of the transition matrix $\boldsymbol{C}$ are shown in (a) with the time lag given as superscript. The true parameter values are denoted by black circles. The fits yield two solutions. The estimates of the *correct* solution are on spot with the true values. The estimates of the *concurrent* solution are incompatible with the true values. In (b) and (c), analogous results are shown for $\boldsymbol{Q}$ and $\boldsymbol{R}$, respectively.

Summary of: Parameter estimation in dynamic processes

Typical for empirical data is the presence of both driving and observational noise. Driving noise belongs to the process and influences its dynamics. Observational noise prevents the direct observation of the state of the underlying process. Depending on the signal-to-noise ratio, the variance of the observation may be dominated by the dynamics of the process or by the observational noise. The state-space model (SSM) is a linear model tailored to such data. It models the dynamics of a system by an autoregressive process together with a linear and stochastic observation equation.

A maximum-likelihood estimator for the parameters of the SSM can be derived using the expectation-maximization (EM) algorithm. While this procedure is well established, its long runtime is a major drawback in application. In this chapter, two optimization strategies are developed which allow to reduce the runtime of the algorithm substantially.

The first optimization exploits the fact that the parameter update is based on the sum of the contributions of all time points in the time series under investigation. This sum can be divided into sub-sums, which allow to run multiple Kalman filters and smoothers, say u, in parallel and combine their results afterwards. Thus, the runtime can be reduced by the factor u.

The second optimization relies on the fixed-point equations for the Kalman filter and smoother gain. In the conventional EM algorithm, these gains must be calculated for each time point of the filtered time series. In the optimized EM algorithm, both gains are calculate only once before each EM iteration and are then applied to the entire time series. In effect, the dependence of the runtime on the number of filtered data points is reduced. This optimization is most efficient for large time series.

The chapter concludes with a simulation study comparing the performance of the conventional and optimized EM algorithm. It is demonstrated, that the optimized algorithm outperforms the conventional one by two orders of magnitude with respect to runtime, and that the parameter estimates of the optimized algorithm are accurate. The optimized algorithm is freely available under https://github.com/wmader/fdmb.

Part III.

PANG: An advanced preamplifier for ECG signals recorded in the MRI environment

Chapter 5.

Reconstruction of the cardiac ECG signal in the MRI environment

For medical applications, a high quality electrocardiogram would be desirable for patients which are under magnetic resonance imaging examination. To date, this is an unsolved filtering problem. In this chapter, an possible solution based on the extended Kalman filter is developed. The material presented is in preparation for publication as W. Mader, W. Buchenberg, M. Mader, B. Schelter, and J. Timmer. Reconstruction of the cardiac ECG signal in a MRI environment. Insights in Medical Physics, in preparation .

Magnetic resonance imaging (MRI) is a medical imaging modality routinely used to image the structure and function of tissue and organs of the human body. Magnetic resonance imaging operates with an external magnetic field in the range of 1.5 T to 3.0 T provided by a superconducting solenoid. Compared to computer tomography or fluoroscopy, which rely on X-ray images, MRI does not involve ionizing radiation. Moreover, MRI allows for different imaging schemes by which contrast recovery can be adapted to the tissue of interest. For some medical interventions, such as cardiac catheterization, the patient's heart must be monitored by means of the electrocardiogram (ECG). The MRI environment however, induces noise into the recording of the ECG, because ions dissolved in the bloodstream get deflected in the presence of a magnetic field by the magnetic part of the Lorentz force. Thus, an ECG recorded in a MRI environment is the superposition of the electrical activity of the heart and the voltage evoked by the Lorentz force.

The endeavor of the work presented in the following is to recover the electrical activity of the heart from the ECG recorded in a MRI environment in order to establish MRI in the catheterization laboratory (cath lab). A cath lab is an examination room in a hospital designed to examine the arteries of the heart as well as the heart chambers and to treat possible abnormalities thereof. The intervention involves inducting one

or several catheters into the patients vessels or chambers. Catheters are used for diagnosis, i.e., an electrophysiology study testing the electrical activity and conduction pathways of the heart, or for intervention, e.g., catheter ablation. Catheter ablation allows to treat arrhythmia that cannot be treated otherwise. Such arrhythmia arise when the conduction pathways of the heart are faulty. By local heating or freezing of the catheter, abnormal tissue causing the arrhythmia is removed. In state of the art cath labs, fluoroscopy is used for catheter guidance and position control. In order to asses the progress and success of ablation, the electrical activity of the heart must be monitored reliably, i.e., a high-quality ECG must be available. The advantage of MRI compared to fluoroscopy in the cath lab would be better visibility of catheters by optimized imaging schemes, which are impossible by fluoroscopy, and avoidance of ionizing radiation, to which patient and staff are exposed.

In the following, an approach to recover the electrical activity of the heart from an ECG recorded in the MRI environment is presented. It employs a non-linear model for the ECG signal of the heart, and the extended Kalman filter to estimate this ECG signal.

In Sec. 5.1, the ECG is introduced, followed by the theory on the induced signal in the presence of a magnetic field in Sec. 5.2. The data available in this project is presented in Sec. 5.3. Section 5.4 ties together the theory of the extended Kalman filter, the model for the cardiac ECG as well as the proposed filtering scheme with associated discussion. Also, the procedure to retrieve parameter values needed for the Kalman filter is presented. Finally, in Sec. 5.5, the filter is applied to ECG measurements and the results of the project are discussed.

5.1. Electrocardiography

The contraction of the heart in the course of a heartbeat is orchestrated by an electrical signal generated by the sinoatrial node and propagated by the electrical conduction system of the heart. It is built up from specialized cardiac muscle cells, not from neurons, making ablation possible. As the electrical signal travels along the heart, the heart muscle depolarizes and contracts. Depolarization causes a change of the electrical potential in cardiac muscle cells. A 12-lead electrocardiogram (ECG) records the time course of 12 standardized projections of the heart's electrical activity from 10 electrodes placed on chest and limbs. Lead I, for example, measures the voltage between the electrodes placed on the left and right wrist. The electrode on the left ankle provides ground. A prototypical lead I time course of one cardiac cycle is shown in Fig. 5.1. Time is normalized and given in radian. The ECG of a healthy heart shows distinct features commonly labeled P, Q, R, S, and T. The ECG conveys information about the operability of the electrical conduction system of the heart. Moreover, mechanical properties of the heart can be inferred from the ECG.

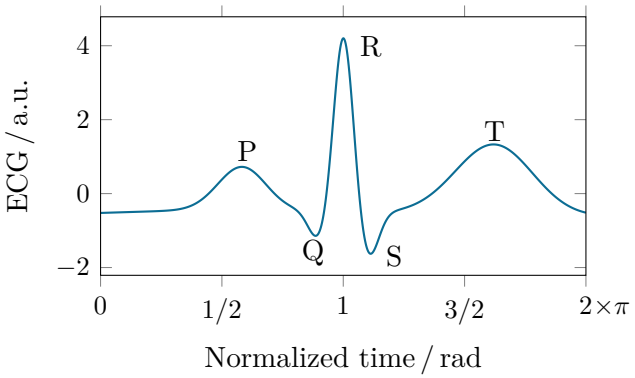

Figure 5.1.: A prototypical lead I trace of one cardiac cycle. The ECG of a healthy heart exhibits distinct features labeled P, Q, R, S, and T. Time is normalized as it has been transformed to angle in radian.

5.2. Blood flow contribution to the ECG in a MRI environment

In this section, the physical background of the voltage induction registered by the ECG in a MRI environment is summarized. This induced voltage is referred to as the magnetohydrodynamic effect [106]. The ECG describing the electrical activity of the heart only is referred to as *cardiac ECG*, the combined recording of the hearts activity and the MHD signal is referred to as *MHD-ECG*.

A theory describing the dynamics of an electrically conducting fluid when interacting with electromagnetic fields is magnetohydrodynamics (MHD) [107]. The general idea is to couple the Navier-Stokes equation with Maxwell's equations by adding the Lorentz force to the set of external forces of the Navier-Stokes equation [108]. While MHD describes a range of dynamic phenomena [109], here only the voltage induced by the flow of blood through an external magnetic field $\boldsymbol{B}$ is of relevance.

In this simplified situation, all observed effects can be explained by the magnetic part of the Lorentz force

$$\boldsymbol{F}_{\mathrm{L}} = q\,(\boldsymbol{v} \times \boldsymbol{B}) \tag{5.1}$$

acting on an ion of charge q dissolved in blood. As depicted in Fig. 5.2 (a), the blood flow velocity $\boldsymbol{v}$ is oriented along the z-axis and the magnetic field $\boldsymbol{B}$ along the x-axis. Consequently, positively charged ions are deflected in positive y-direction while negatively charged ions are deflected in negative y-direction. The separation of ions results in the electrical field

$$\boldsymbol{E} = \boldsymbol{v} \times \boldsymbol{B}\,, \tag{5.2}$$

as depicted in Fig. 5.2 (b). This process corresponds to the Hall effect in electrical conductors.

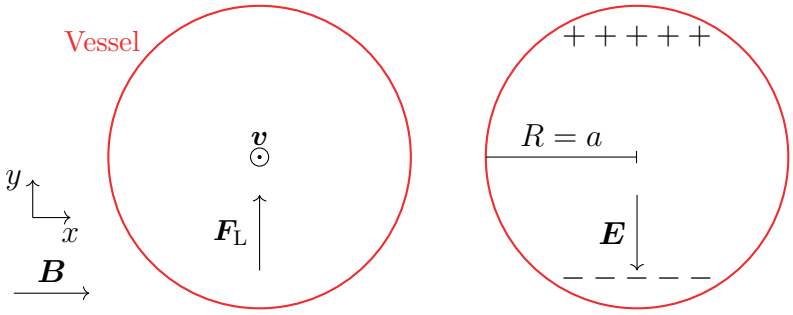

(a) Lorentz force acting on ions.

(b) Charge separation and induced electrical field.

Figure 5.2.: Schematics of forces and fields in the plain of the cross section of a blood vessel. In (a), the blood flow velocity $\boldsymbol{v}$ and the resulting Lorentz force acting on ions dissolved in blood is depicted. The external magnetic field $\boldsymbol{B}$ is oriented along the x-axis. The Lorentz force separates positively and negatively charged ions. The separated charges and the resulting electric field are shown in (b).

By integrating $\boldsymbol{E}$ over the diameter $2a$ of the vessel along the y-axis, the induced voltage

$$\begin{aligned} -U &= \int_a^a \boldsymbol{E}(r) \cdot \boldsymbol{e}_y \, \mathrm{d}r \\ &= \int_a^a |\boldsymbol{E}(r)| \, \mathrm{d}r \end{aligned} \tag{5.3}$$

is obtained. Under established conditions, Eq. (5.3) simplifies to

$$-U = 2aB\bar{v}\,, \tag{5.4}$$

where $\bar{v}$ is the mean velocity of the blood across the vessel and $B = |\boldsymbol{B}|$ [108, 110]. Equation (5.4) describes the voltage contribution of an infinitesimally short segment of the vessel that is perpendicular to $\boldsymbol{B}$. While the largest portion of U is induced in the aortic arch [111, 112], where Eq. (5.4) is approximately valid, the overall induced voltage also comprises contributions from smaller vessels, and the complex flow of blood in the heart [113]. Since in medical applications, the velocity field of the blood is unknown, the overall induced voltage cannot be determined and accordingly subtracted from the MHD-ECG in order to reconstruct the cardiac ECG. Consequently, data-analysis-based approaches are more feasible than modeling from first principles [106, 114].

5.3. The electrocardiogram data

From a healthy volunteer, a 12-lead ECG is recorded at 1000 Hz by standard equipment* used in clinical routine. The ECG is recorded outside and inside a MRI scanner†. The static magnetic field of the scanner is 1.5 T. For image acquisition, magnetic field gradients and radio waves are generated by the imaging unit of the scanner. Since the ECG equipment can not be used in the presence of alternating electromagnetic fields, the imaging unit is turned off during ECG acquisition.

Ten seconds of pristine cardiac ECG recorded at $B = 0\,\mathrm{T}$ are shown in Fig. 5.3. Across all leads, a clear ECG of the heart's electrical activity is traced. Figure 5.4 shows the same amount of data recorded from the same volunteer inside the MRI scanner at $B = 1.5\,\mathrm{T}$. The aim of the project is to resurrect the cardiac ECG as shown in Fig. 5.3 from recordings of the MHD-ECG as shown in Fig. 5.4 in real time.

Judging by the eye from Fig. 5.4, the electric signal of the heart vanishes in the first six leads. Not even the most prominent event in lead I, the R-peak, remains detectable. Since the MHD contribution to the ECG is caused by the blood flow, it is expected to be on the same time scale as the cardiac ECG. Surprisingly, the additional noise in the ECG is not only on this but also on a much faster time scale. The observational noise seems to be amplified by the presence of the magnetic field. One might thus speculate that the standard ECG equipment used is not appropriate for the MRI environment. For example, specially shielded cables might be required in order to prevent interference with the magnetic field.

The lead that contains the highest amplitudes and best visible QRS-complexes is lead V2. It is thus the best candidate to recover the ECG. The remaining discussion will concentrate on this lead.

5.3.1. Average time course of the cardiac cycle

The largest impact of the MHD effect is expected to occur at the time of the T-wave, when the blood is ejected from the left ventricle [111]. To see this, the mean of subsequent cardiac cycles is considered. In order to calculate average time courses, the ECG recordings are segmented into single cardiac cycles aligned at their R-peaks. Since individual cardiac cycles differ in their length, their recording time must be normalized such that the same sample point is comparable across different cycles. To this end, the cardiac cycles are resampled, such that each cycle spans 200 sample points. The average cardiac cycle and its standard deviation is estimated from the ensemble of segmented cardiac cycles.

In order to characterize the effect of an external magnetic field onto the ECG, an ECG is recorded at varying strengths of the magnetic field. In Fig. 5.5, means and standard deviations of cardiac cycles, estimated from approximately 80 single

*EP-Tracer, CardioTek, Maastricht
†Symphony, Siemens, Germany

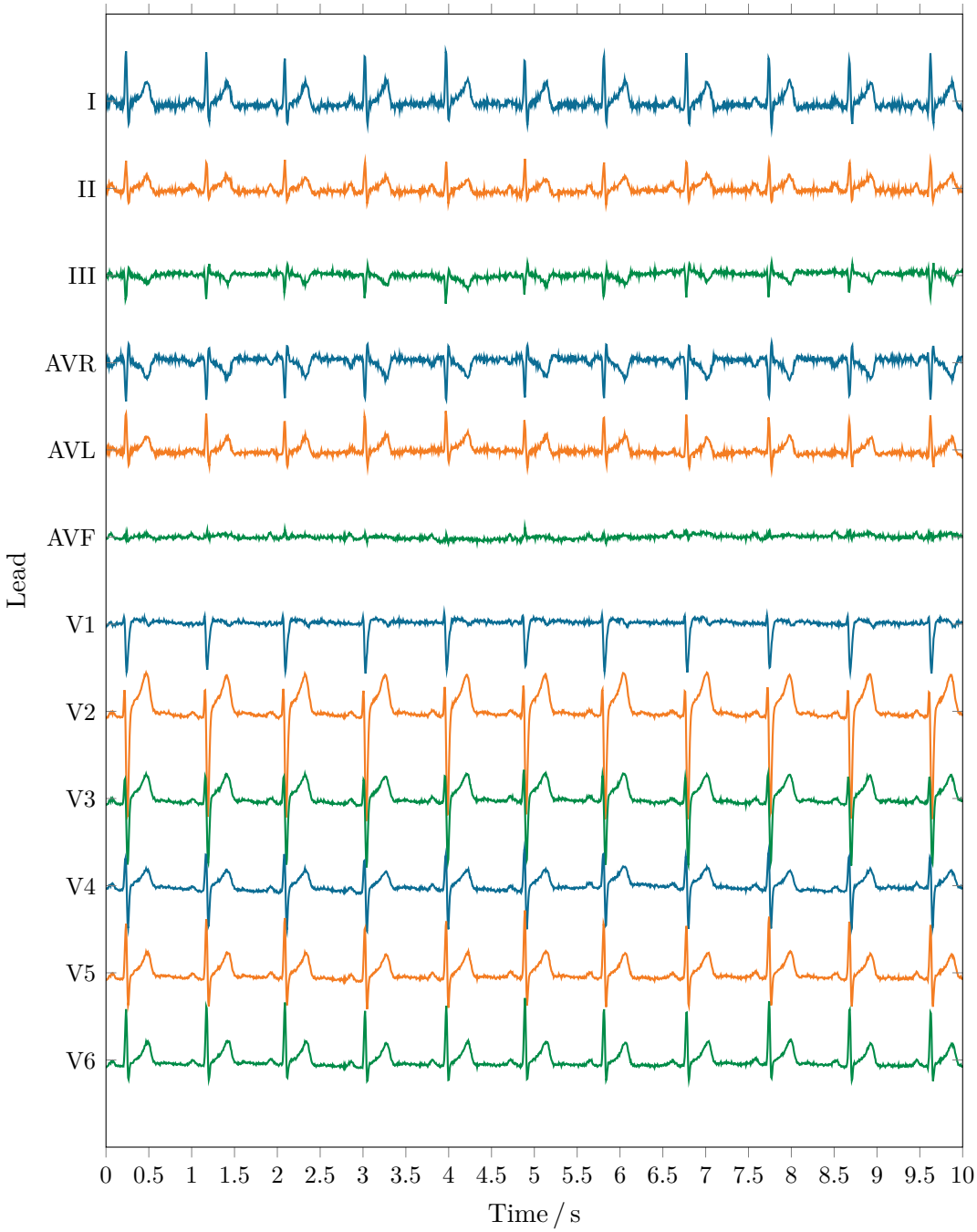

Figure 5.3.: A 12-lead ECG recorded outside the MRI scanner at $B = 0\,\mathrm{T}$. Each lead show a clean signal originating from the electrical activity of the heart. The lead AVF projects along an isopotential, such that the ECG signal almost vanishes.

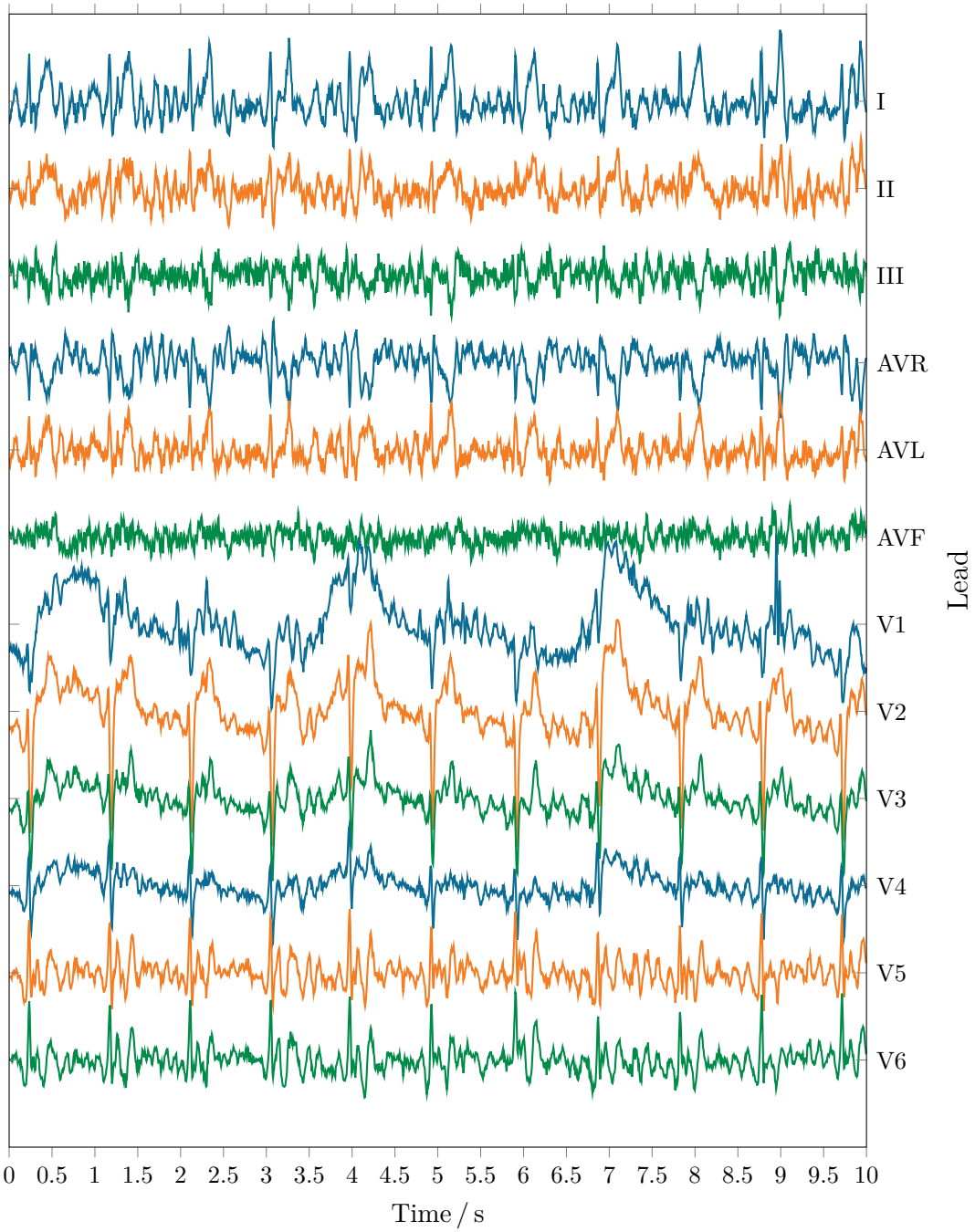

Figure 5.4.: A 12-lead ECG recorded inside the MRI scanner at $B = 1.5\,\mathrm{T}$. All leads are heavily contaminated with observational noise. The observation noise is on the time scale of the ECG as well as on a much faster time scale.

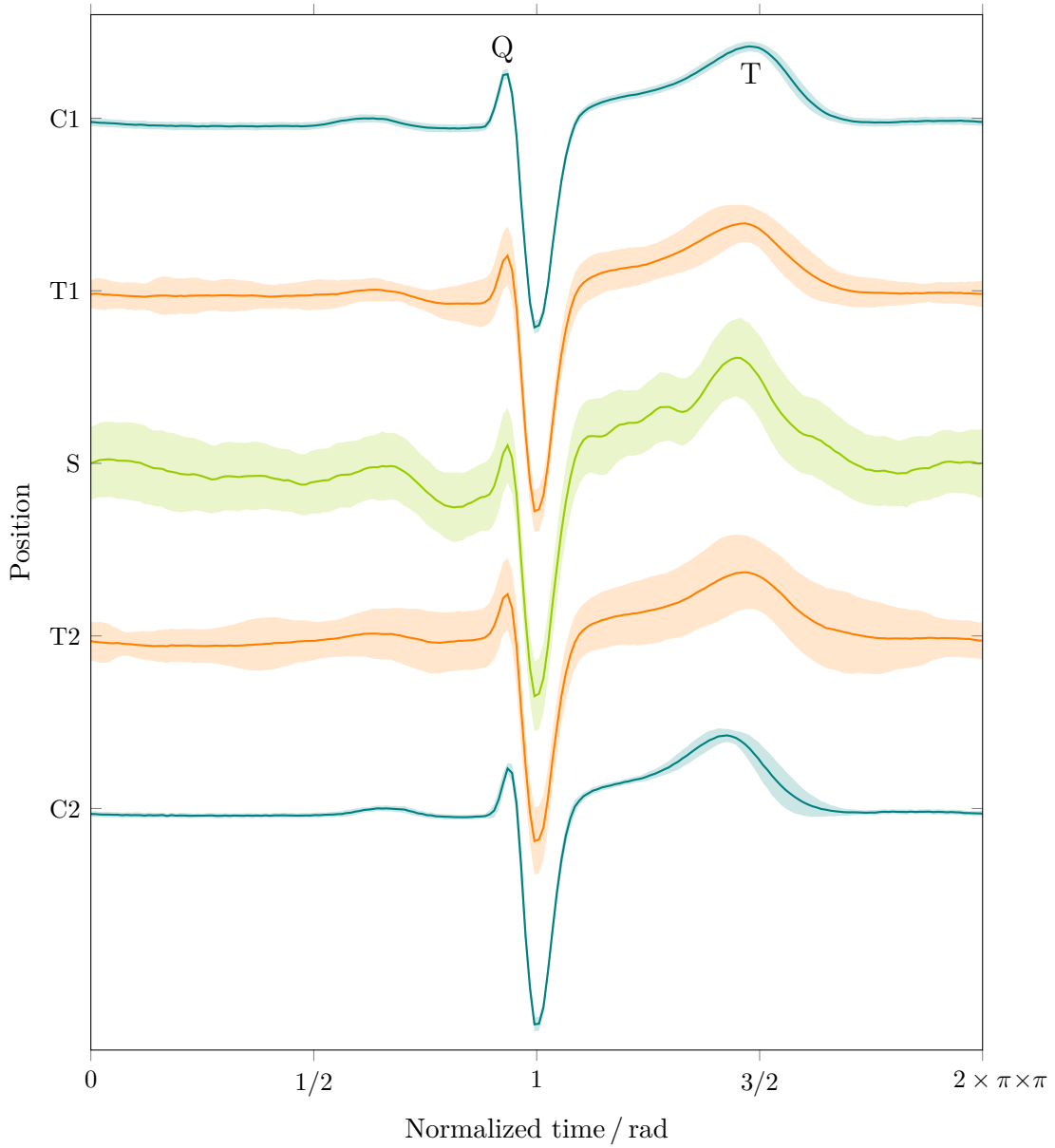

Figure 5.5.: Mean ECG cardiac cycles of one volunteer recorded at different magnetic field strengths B. To investigate hysteresis effects, the ECG was firstly recorded outside of the MRI scanner (C1), secondly on the examination table outside of the scanner (T1), thirdly inside the scanner (S), and than in revered order presented as T2 and C2, respectively. The recordings C1 and C2 show a typical V2 lead dynamics. At the intermediate position corresponding to T1 and T2, the morphology remains almost unchanged, but the standard deviation of the signal given as ribbon is considerably increased. Inside the scanner a large amount of observational noise is present, and the variance of the signal is further increased.

cycles each, are shown. The respective ECG time series are consecutively recorded as ordered from top to bottom. The plots labeled C1 and C2, respectively, are calculated from an ECG recorded outside the MRI examination room at $B = 0\,\mathrm{T}$. The cardiac ECG is well resembled. The ribbon denotes the standard deviation of the considered cardiac cycles. The average traces T1 and T2 correspond to recordings for which the volunteer is positioned on the MRI examination table, with the table extended out of the scanner. At this intermediate field strength, the morphology of the signal remains largely unchained compared to C1 or C2. However, the variance has already increased considerably. Inside the scanner (S), the variance has further increased, and even the overall shape of the ECG has changed. The T-wave is now approximately three times as large as the Q-wave. This is due to the MHD effect. Also, additional fluctuations are present in the previously flat part as of C1. It is unclear if this can be solely attributed to the MHD effect or whether other sources like cable-noise caused by the magnetic field play also a role. The comparison of C1 to C2 and T1 to T2 reveals no hysteresis in the signal.

5.3.2. Filter requirements

The MHD signal and the cardiac ECG overlap both in the time and frequency domain [115]. Therefore, a classical filter in either of the domains would be ineffective. If applied to a given time or frequency range, both the electrical activity of the heart and the MHD effect would be filtered out to the same extent. Moreover, it is the aim of this project, to be able to capture temporal changes in the ECG as well as single events such as a premature ventricular contraction. Therefore, averaging is an inappropriate option. In order to meet the requirements for the reconstruction of the cardiac ECG, an approach using the extended Kalman filter together with a non-linear model for the cardiac ECG is pursued in this thesis. In contrast to methodologically comparable approaches [106, 114, 116], here, data recorded by standard equipment already established in medical routine is used. Thus, MRI compatibility would come as an update of the currently used EP-Tracer software.

5.4. Extended Kalman filter and ECG model

The Kalman filter is optimal for estimating the hidden states $\boldsymbol{X}$ of the linear SSM in the sense that $\mathrm{E}[(\boldsymbol{X}_t - \hat{\boldsymbol{x}}_t)^2 \,|\, \boldsymbol{y}_1, \ldots, \boldsymbol{y}_t]$ is minimized, cf., Sec. 4.4. The model for the cardiac ECG is however non-linear. Two methods to extend the Kalman filter to the non-linear domain are available. For the *extended* Kalman filter, the dynamic model used is linearized such that the usual Kalman filter equations can be employed with only small adaptions. The *unscented* Kalman filter avoids the linearization of the model. Instead, a set of points are obtained, such that their sample mean and covariance reflect the mean and covariance of the state. These points are termed sigma points. In contrast to Monte-Carlo-type particle filters, sigma points are not drawn

from a probability distribution, but they are constructed by a deterministic algorithm. That way, the first two moments of the state are characterized by the least possible number of sample points. The sigma points are propagated by the non-linear model to predict future mean and covariance of the state [117]. Both filters were implemented and tested in this project. However, the unscented Kalman filter proved to be unstable because the model used for the MHD-ECG does not capture all effects present in the data. Therefore, only results from the extended Kalman filter are discussed. In the following, the extended Kalman filter and afterwards the model for the ECG of the heart is discussed.

5.4.1. The extended Kalman filter

The state-space model (SSM) in its conventional linear form is introduced in Sec. 4.1. Now, the SSM

$$\boldsymbol{X}(t) = f(\boldsymbol{X}(t-1), \boldsymbol{\epsilon}(t)), \quad \boldsymbol{\epsilon}(t) \sim \mathcal{N}(\boldsymbol{0}, \boldsymbol{Q}) , \tag{5.5}$$

$$\boldsymbol{Y}(t) = g(\boldsymbol{X}(t), \boldsymbol{\eta}(t)), \qquad \boldsymbol{\eta}(t) \sim \mathcal{N}(\boldsymbol{0}, \boldsymbol{R}) \tag{5.6}$$

is considered, in which the equation $f : \mathbb{R}^k \to \mathbb{R}^k$ governing the process is possibly non-linear, as is the observation equation $g : \mathbb{R}^k \to \mathbb{R}^o$. In application, the state vector $\boldsymbol{X}(t)$ as well as the realizations of the random variables $\boldsymbol{\epsilon}$ and $\boldsymbol{\eta}$ modeling driving and observational noise are unknown. However, given an estimate of the state vector at time $t-1$, say $\hat{\boldsymbol{x}}_{t-1}^{t-1}$, predictions of the state and observation vectors at time t are

$$\hat{\boldsymbol{x}}_t^{t-1} = f\left(\hat{\boldsymbol{x}}_{t-1}^{t-1}, \boldsymbol{0}\right) , \tag{5.7}$$

$$\hat{\boldsymbol{y}}_t^{t-1} = g\left(\hat{\boldsymbol{x}}_t^{t-1}, \boldsymbol{0}\right) , \quad \text{with } \mathrm{E}(\boldsymbol{\epsilon}) = \mathrm{E}(\boldsymbol{\eta}) = \boldsymbol{0} . \tag{5.8}$$

The notation of time as sub- and superscript is as introduced in Sec. 4.4. While Eqs. (5.7) and (5.8) are appropriate to predict the state and its observation, f and g must be linearized in order to propagate covariance matrices. To this end, the time-dependent Jacobian matrices $\boldsymbol{C}_t$, $\boldsymbol{V}_t$, $\boldsymbol{O}_t$, and $\boldsymbol{W}_t$, with entries

$$C_{ij} = \frac{\partial f_i}{\partial x_j}(\hat{x}_t^t, 0) , \quad V_{ij} = \frac{\partial f_i}{\partial \epsilon_j}(\hat{x}_t^t, 0) , \quad O_{ij} = \frac{\partial h_i}{\partial x_j}(\hat{x}_t^t, 0) , \quad W_{ij} = \frac{\partial h_i}{\partial \eta_j}(\hat{x}_t^t, 0) \tag{5.9}$$

are calculated. With the established notation, the extended Kalman filter takes the form [118]

$$\hat{\boldsymbol{x}}_t^{t-1} = f\left(\hat{\boldsymbol{x}}_{t-1}^{t-1}, 0\right) , \tag{5.10}$$

$$\boldsymbol{P}_t^{t-1} = \boldsymbol{C}_t \boldsymbol{P}_{t-1}^{t-1} \boldsymbol{C}_t^{\mathrm{T}} + \boldsymbol{V}_t \boldsymbol{Q}_t \boldsymbol{V}_t^{\mathrm{T}} , \tag{5.11}$$

$$\hat{\boldsymbol{x}}_t^t = \hat{\boldsymbol{x}}_t^{t-1} + \boldsymbol{K}_t \left[\boldsymbol{y}_t - g\left(\hat{\boldsymbol{x}}_t^{t-1}, 0\right)\right] , \tag{5.12}$$

$$\boldsymbol{P}_t^t = \boldsymbol{P}_t^{t-1} - \boldsymbol{K}_t \boldsymbol{O}_t \boldsymbol{P}_t^{t-1} , \tag{5.13}$$

$$\boldsymbol{K}_t = \boldsymbol{P}_t^{t-1} \boldsymbol{O}_t^{\mathrm{T}} \left(\boldsymbol{O}_t \boldsymbol{P}_t^{t-1} \boldsymbol{O}_t^{\mathrm{T}} + \boldsymbol{W}_t \boldsymbol{R}_t \boldsymbol{W}_t^{\mathrm{T}}\right)^{-1} . \tag{5.14}$$

As with the conventional Kalman filter, model parameters must be known or estimated.

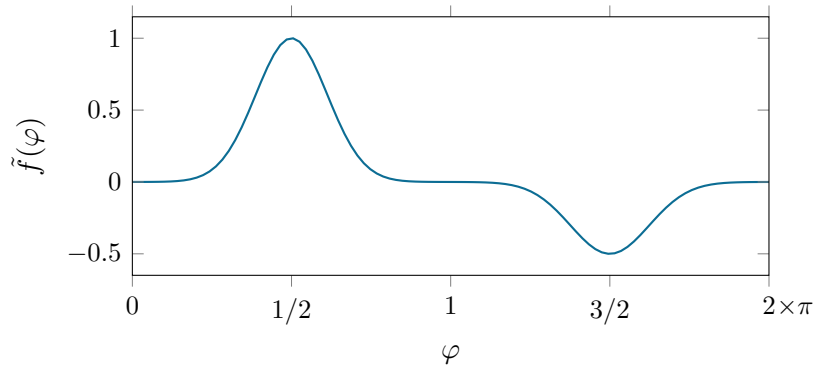

Figure 5.6.: Trajectory of $\tilde{f}(\varphi)$, cf., Eq. (5.16), exemplifying how events in the ECG are modeled.

5.4.2. A model for the cardiac ECG

In the model for the cardiac ECG, the events P, Q, R, S, and T are modeled by [119]

$$f_i(\varphi) = a_i \exp\left[-\frac{(\varphi-\varphi_i)^2}{2\sigma_i^2}\right], \quad i \in \Omega = \{\mathrm{P},\, \mathrm{Q},\, \mathrm{R},\, \mathrm{S},\, \mathrm{T}\}\,. \tag{5.15}$$

Since the ECG is a quasi-periodic signal, f is considered a function of angle $\varphi \in [0, 2\pi] \subset \mathbb{R}$. The position of the i-th event is defined by φ_i, its amplitude and width by a_i and σ_i, respectively. To exemplify the shape of $f_i(\varphi)$, the graph of

$$\begin{aligned} \tilde{f}(\varphi) = \sum_{i=2}^{2} f_i(\varphi) \quad \text{with} \quad & a_1 = 1\,, \qquad \phi_1 = \frac{1}{2}\pi\,, \quad \sigma_1^2 = 0.5\,, \\ & a_2 = -0.5\,, \quad \phi_2 = \frac{3}{2}\pi\,, \quad \sigma_2^2 = 0.3 \end{aligned} \tag{5.16}$$

is shown in Fig. 5.6. In the extended Kalman filter, the state $\boldsymbol{X}(t)$ must be iterated to $\boldsymbol{X}(t+\delta)$. Thus, the time derivative of Eq. (5.15) is needed. With the angular frequency ω

$$\frac{\mathrm{d}\varphi}{\mathrm{d}t} = \omega, \tag{5.17}$$

$$\frac{\partial f_i}{\partial \varphi}\frac{\mathrm{d}\varphi}{\mathrm{d}t} = -\omega\frac{\varphi-\varphi_i}{\sigma_i^2} f_i(\varphi) \tag{5.18}$$

is derived. Integration of Eqs. (5.17) and (5.18) from time t to $t+\delta$ can be accomplished, e.g., by the Euler method. The cardiac ECG $X(t)$ is then described by

$$\varphi(t+\delta) = (\varphi(t) + \delta\omega) \bmod 2\pi\,, \tag{5.19}$$

$$X(t+\delta) = X(t) - \delta\omega \sum_{i\in\Omega} \frac{\Delta\varphi_i}{\sigma_i^2} f_i(\varphi) + \nu(t+\delta) \tag{5.20}$$

$$= X(t) - \delta\omega \sum_{i\in\Omega} \frac{\Delta\varphi_i}{\sigma_i^2} a_i \exp\left(-\frac{\Delta\varphi_i^2}{2\sigma_i^2}\right) + \nu(t+\delta)\,. \tag{5.21}$$

Discrepancies between model and data are accounted for by the Gaussian driving noise term $\nu(t)$ [119, 120]. In Fig. 5.1 on p. 93, one cardiac cycle of the model is shown in lead I projection for $\nu = 0$. The model is 2π periodic.

The duration of a human cardiac cycle is approximately one second. By adapting ω in Eqs. (5.19) and (5.21), the duration of actually measured individual cycles can be mapped to $[0, 2\pi] \subset \mathbb{R}$. By this normalization of time the model can be applied to data with different cardiac cycle duration.

Defining $\boldsymbol{X}(t) = (\varphi(t), X(t))^{\mathrm{T}}$, the observation of $\boldsymbol{X}(t)$ is modeled as

$$\boldsymbol{Y}(t) = \boldsymbol{I}\boldsymbol{X}(t) + \boldsymbol{\eta}(t)\,, \quad \boldsymbol{\eta}(t) \sim \mathcal{N}\left(\boldsymbol{0}, \boldsymbol{I} \cdot \begin{pmatrix} \sigma_\varphi^2(t) \\ \sigma_X^2(t) \end{pmatrix}\right)\,, \tag{5.22}$$

with $\sigma_\varphi(t)$ the standard deviation of the position $\varphi(t)$ and $\sigma_X(t)$ the standard deviation of the ECG $X(t)$.

5.4.3. Linearization of the model

In the model of the cardiac ECG, $\varphi(t)$ and $X(t)$ define the state, while ω, a_i, φ_i, and σ_i are considered *iid* Gaussian random variables. They are thus attributed to the process noise of Eq. (5.5), such that

$$\boldsymbol{\epsilon} = (\omega, a_i, \varphi_i, \sigma_i, \nu)^{\mathrm{T}}\,, \quad i \in \Omega\,, \tag{5.23}$$

results. The two-dimensional state transition matrix

$$\boldsymbol{C}_t = \begin{pmatrix} \dfrac{\partial \varphi_t}{\partial \varphi_t} & \dfrac{\partial \varphi_t}{\partial X_t} \\ \dfrac{\partial X_t}{\partial \varphi_t} & \dfrac{\partial X_t}{\partial X_t} \end{pmatrix} = \begin{pmatrix} 1 & 0 \\ a_{21} & 1 \end{pmatrix}\,, \quad \text{with} \tag{5.24}$$

$$a_{21} = -\delta\omega \sum_{i \in \Omega} \frac{a_i}{\sigma_i^2} \left(1 - \frac{\Delta\varphi_i^2}{\sigma_i^2}\right) \exp\left(-\frac{\Delta\varphi_i^2}{2\sigma_i^2}\right) \tag{5.25}$$

is obtained by linearization of the dynamic equations (5.19) and (5.21) as formulated in Eq. (5.9). The transition matrix for the driving noise covariance matrix $\boldsymbol{V}$ is derived analogously. The respective partial derivatives can be found in [120, Eq. 11]. The observation equation (5.22) is linear such that

$$\boldsymbol{O} = \boldsymbol{W} = \begin{pmatrix} 1 & 0 \\ 0 & 1 \end{pmatrix}\,. \tag{5.26}$$

5.4.4. Modeling the cardiac ECG in a scanner

Models of ECG recordings from inside the MRI scanner have to comprise not only the cardiac ECG, denoted $\mathcal{E}$, but also the MHD effect, say $\mathcal{M}$. Here, the model

$$\begin{aligned} X(t) &= \mathcal{E}(t)\,, \\ Y(t) &= X(t) + \mathcal{M}(t) + \eta(t)\,, \end{aligned} \tag{5.27}$$

which can be collated to

$$Y(t) = \mathcal{E}(t) + \mathcal{M}(t) + \eta(t) \tag{5.28}$$

is used. The MHD effect is part of the observation equation as it does not interact with the dynamics of the heart. Together with $\eta(t)$ it forms the observational noise. Since $\mathcal{M}(t)$ is not *iid* as it exhibits temporal correlations, it cannot be combined with $\eta(t)$. Based on the model given by (5.28) three ways to recover $\mathcal{E}(t)$ are conceivable.

MHD effect modeled from first principles Using a model from first principles for $\mathcal{M}$ and accompanying measurements, the expected value of the ECG

$$\mathrm{E}\left[\mathcal{E}(t)\right] = Y(t) - \mathcal{M}(t) \tag{5.29}$$

is easily accessible using $\mathrm{E}(\eta) = 0$. The field of blood velocity causing the MHD effect is complex and unknown in application. Firstly, this is due to the pulsative nature of the blood flow. Even more important though is the fact that the orientation of the flow with respect to $\boldsymbol{B}$ cannot be determined on a per-patient basis. Primarily, the position of blood vessels are unknown since these anatomic details vary between humans. Furthermore, the exact placement of the patient on the examination table cannot be controlled precisely. For these reasons, this approach, while elegant, is not feasible.

Effective model combining the cardiac ECG and the MHD effect A second possibility of establishing $Y(t)$ is to describe $\mathcal{M}(t)$ by a similar model as $\mathcal{E}(t)$. Instead of parameters that fit the dynamics of $\mathcal{E}(t)$, parameters that correspond to the average MHD effect need to be specified. This approach would combine two models of the form given in Eq. (5.21) in an additive manner. As each single model consists of summations only, the two effective models are equivalent to a single effective one with respectively many terms and adjusted driving noise. Since the signals from the heart and the MHD effect overlap in time and frequency domain [114], a single effective model cannot help in discriminating the two sources. In consequence, a deviation from, e.g., the usual T-wave could indistinguishably be caused by a change in the electrical activity of the heart or a change in the velocity field of the blood and thus by the MHD effect. In order to make $\mathcal{E}(t)$ identifiable in this approach, the model for $\mathcal{M}(t)$ needs to be fixed for the entire examination time, implying a MHD signal which does not change between cardiac cycles. As this assumption does not hold for cath lab interventions, this approach is inappropriate for the problem at hand.

Model the cardiac ECG directly This is the approach proposed and developed in this thesis. Therefore, first the mean MHD effect $\bar{\mathcal{M}}(t)$ is derived from the difference of the ECG signal recorded inside and outside of the scanner. Then the observed cardiac ECG is assumed to be given by

$$\tilde{\mathcal{E}}(t) = Y(t) - \bar{\mathcal{M}}(t)\,. \tag{5.30}$$

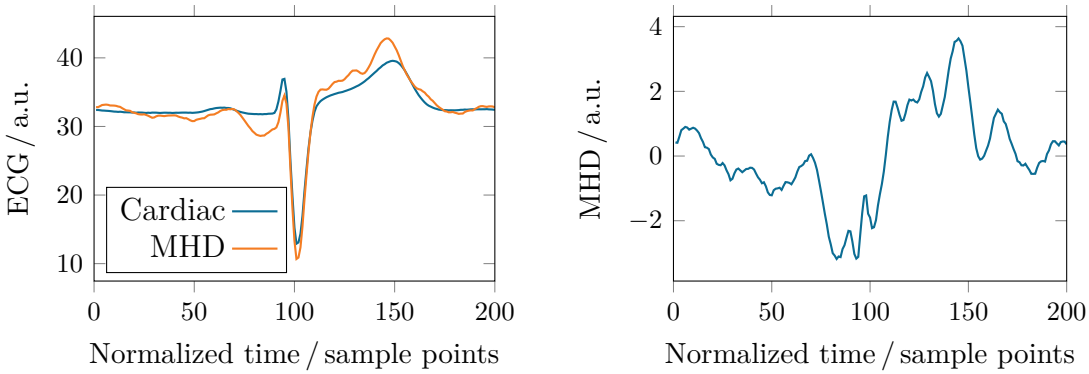

(a) Average cardiac- and MHD-ECG

(b) Average MHD signal

Figure 5.7.: Average time courses and their difference for lead V2. Figure (a) shows in blue the average of the cardiac ECG calculated from 101 cardiac cycles, and in orange the MHD-ECG calculated from 77 cardiac cycles. The most prominent differences are located at the P- and the T-wave. In (b), the average MHD signal is presented. It is defined as the difference of the average cardiac ECG and the average MHD-ECG.

From $\tilde{\mathcal{E}}(t)$, the true underlying cardiac ECG state is estimated by the extended Kalman filter. The drawback of this approach is that the MHD effect is assumed to stay constant during the examination time. However, since $\tilde{\mathcal{E}}(t)$ complies with the model of the cardiac ECG in the best possible way, and the Kalman filter is known to be optimal for estimating hidden states, this approach is promising.

5.4.5. Estimating the mean MHD effect

From the resampled ensemble of single cardiac cycles, cf., Sec. 5.3.1, the average cycle of the cardiac and the MHD-ECG is calculated. Both average time courses of lead V2 are presented in Fig. 5.7 (a). The difference of the two time courses shown in Fig. 5.7 (b) is the mean MHD effect registered in lead V2. The mean MHD effect of other leads is estimated accordingly.

5.4.6. Kalman filter preliminaries

The Kalman filter estimates hidden states by the support of a model. The observations based on which the hidden states are estimated are assumed to be a realization of that model observed by a known observation function. Additive normally *iid* observational noise may be introduced by the observation function. By considering the MHD signal as part of the observational noise, the observational noise is not anymore distributed as assumed. Even if the average MHD signal is removed from the MHD-ECG, observations cannot be fully described by the model of the cardiac ECG, because the inter-cycle variation of the MHD signal is too large. This makes

adaptions of the filter necessary to which end the covariance matrices of the driving and the observational noise $\boldsymbol{Q}$ and $\boldsymbol{R}$ are adjusted.

In the Kalman filter, the correction of the observed state by the model takes into account the difference between the observed state and its prediction by the model. The effect of the model onto the final estimate is stronger the more reliable the prediction is compared to the observation. In other words, if $\boldsymbol{R}$ is large compared to $\boldsymbol{Q}$, the model prediction dominates the state estimate and the other way around.

5.4.7. Noise covariance matrices in the extended Kalman filter

The interplay of $\boldsymbol{Q}$ and $\boldsymbol{R}$ in the extended Kalman filter is as follows. The predicted state for time t based on all information up to $t-1$, $\hat{\boldsymbol{x}}_t^{t-1}$, is corrected by the prediction mismatch and the Kalman gain as

$$\hat{\boldsymbol{x}}_t^t = \hat{\boldsymbol{x}}_t^{t-1} + \boldsymbol{K}_t \left[\boldsymbol{y}_t - g\left(\hat{\boldsymbol{x}}_t^{t-1}, 0 \right) \right] . \tag{5.31}$$

Thus, the Kalman gain determines the amount of correction applied to the predicted state. The Kalman gain is a function of the state covariance $\boldsymbol{P}$ and the observational noise covariance $\boldsymbol{R}$. On the one hand, if the driving noise covariance $\boldsymbol{Q}$ is large, the model output is dominated by driving noise. In consequence, the modeled dynamics vanish leading to an uninformative model prediction. Accordingly, $\boldsymbol{P}$ also is large [$\rightarrow$ cf. Eq. (5.11)] such that the filter tends to rely on the observation. On the other hand, if $\boldsymbol{R}$ is large, observations are uninformative or unreliable such that the state estimate is mostly based on the model prediction.

In conclusion, the final estimate depends both on the model and on the observation. The extent to which it is influenced by either of the two factors depends on the relation of $\boldsymbol{Q}$ and $\boldsymbol{R}$. By tuning this relation, it is thus possible to adjust the degree of model-guided smoothing to derive the final estimate of the underlying cardiac ECG, $\hat{\boldsymbol{x}}_t^t$. This idea is pursued in the following.

5.4.8. Determining parameter values

The free parameters of the Kalman filter are the parameters of the cardiac ECG model, cf., Eq. (5.21), and the elements of the covariance matrices of the driving and observational noise, $\boldsymbol{Q}$ and $\boldsymbol{R}$, respectively.

Parameters of the ECG model

The parameters of the model of the cardiac ECG are fitted to the mean time course of the cardiac ECG by the Levenberg-Marquardt algorithm as implemented in Matlab 2013a. Fitted parameters are a_i, φ_i, and σ_i with $i \in \Omega = \{P, Q, R, S, T\}$. The angular frequency ω is fixed, as each cardiac cycle is resampled to span 200 sample points such that time is already normalized. For lead V2, the fit result is shown in Fig. 5.8 in orange. The mean time course of the cardiac ECG is presented in green. Since exactly

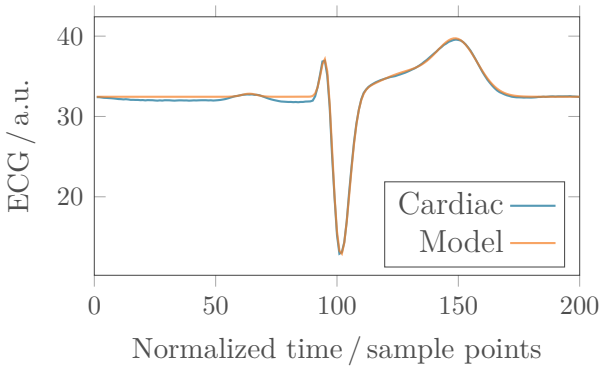

Figure 5.8.: Mean cardiac ECG and model fit. The mean time course of the cardiac ECG of lead V2 is shown in blue. To this time course, the model of the cardiac ECG is fitted. The model output with fit parameters is given in orange.

five events are modeled, the cardiac ECG model can only fit to these events, while to other trends in the signal it remains unfitted. Therefore, the first 50 sample points are a flat line in the fit. The parameter values of this fit are used in all results presented in the following.

Covariance $\boldsymbol{R}$ of the observational noise

In general, the covariance of the driving and observational noise are not free parameters but determined by the dynamics and the measurement device, respectively. However, in this application, the Kalman filter is used to provide an operator with the possibility to select the amount of model-based smoothing applied to observations by adjusting the driving and observational noise covariance matrices, accordingly.

For all results presented, the covariance of the observational noise is

$$\boldsymbol{R} = \begin{pmatrix} 0 & 0 \\ 0 & 5.6 \end{pmatrix} \times 10^6 \,. \tag{5.32}$$

The first dimension corresponds to time. Each cardiac cycle is normalized, and for each cycle, the model and data are aligned with respect to the R-peak. Therefore, the position in time is well determined, represented by the variance $R_{11} = 0$. The second dimension corresponds to the observational noise of the ECG for which the variance is estimated from measurements. To this end, first $\tilde{\mathcal{E}}(t)$ [$\rightarrow$ Eq. (5.30)] is calculated for each cardiac cycle. Then, the difference of $\tilde{\mathcal{E}}(t)$ and the mean cardiac ECG is obtained. This time series specifies the MHD signal $\Delta\mathcal{M}_i(t)$ of each individual cardiac cycle i. The MHD effect is assumed to cause the major part of the observational noise. Therefore, the variance of the observational noise is identified with the variance of $\Delta\mathcal{M}_j(t)$, which is 5.6×10^6 for this recording.

Covariance $\boldsymbol{Q}$ of the driving noise

The uncertainty of the parameters of the model ω, a_i, φ_i, and σ_i with $i \in \Omega$ together with the variance of ν, cf., Eq. (5.21), are combined in the diagonal covariance matrix of the driving noise. The diagonal of $\boldsymbol{Q}$ contains thus the variances

$$\left\{\sigma_\omega^2, \sigma_{a_i}^2, \sigma_{\varphi_i}^2, \sigma_{\sigma_i}^2, \sigma_\nu^2\right\}, \quad i \in \Omega\,. \tag{5.33}$$

Since time is well determined as elaborated in the previous paragraph, σ_ω^2 is zero. The amplitudes a_i and widths σ_i of ECG events are likely to vary with different cardiac cycles. Therefore, the variance of the corresponding driving noise

$$\sigma_{a_i}^2 = a_i \times 10^{-1}\,, \quad \sigma_{\sigma_i}^2 = \sigma_i \times 10^{-1}\,, \quad \forall i \in \Omega \tag{5.34}$$

is chosen to 10 % of the respective parameter value. Assuming the activity of the heart as regular, it is reasonable to fix the positions φ_i of ECG events in the model by setting $\sigma_{\varphi_i}^2$ to zero. The variance of the driving noise ν of the model for the cardiac ECG

$$\sigma_\nu^2 = R_{22} \times 10^{-3} \tag{5.35}$$

is determined relative to the variance of the observational noise of the ECG, R_{22}. That way, the ratio of the two quantities is fixed and reflects the degree to which the prediction is determined by model and observation.

As discussed in Sec. 5.4.7, the Kalman filter is supposed to operate with a manually tuned ratio of $\boldsymbol{Q}$ and $\boldsymbol{R}$. For this to facilitate easily, a proportionality factor γ is introduced for each diagonal element of $\boldsymbol{Q}$. The filter ultimately operates with $\boldsymbol{Q}$ multiplied by the diagonal matrix of proportionality factors. The diagonal of this matrix is denoted $\boldsymbol{\gamma}$. In the following, filtering results are presented for different values of $\boldsymbol{\gamma}$. Initially,

$$\gamma_\omega = \gamma_\nu = \gamma_{\varphi_i} = \gamma_{a_i} = \gamma_{\sigma_i} = 1\,. \tag{5.36}$$

Apart from the argumentation given for the values of the covariance matrices, parameter values are determined by experience.

5.4.9. Proposed filter procedure

The proposed procedure to reconstruct the cardiac ECG from the ECG recorded in a MRI scanner is as follows.

1. Record 30 s of cardiac ECG at $B = 0\,\mathrm{T}$.
2. Record 30 s of MHD-ECG inside the MRI scanner at $B > 0\,\mathrm{T}$
3. Process the recordings obtained in step 1 and 2 as follows

a) Segment each time series into single cardiac cycles and align each cycle at its R-peak.

b) Remove the respective median from each cycle.

c) Calculate the mean cardiac and mean MHD cycle by averaging over the ensemble of respective cycles.

d) Calculate the average MHD effect, $\bar{\mathcal{M}}(t)$, as the difference of the mean cardiac cycle and mean MHD cycle obtained in the last step.

e) Subtract the average MHD effect from each cardiac cycle of the MHD-ECG. The resulting time series is denoted $\breve{\mathcal{E}}(t)$.

4. Estimate the variance of the observational noise R_{22}. To this end, subtract the mean cardiac cycle from each cardiac cycle of $\breve{\mathcal{E}}(t)$ and join the resulting data in a new time series. The variance of this joint time series determines R_{22}.

5. Fit the model of the cardiac ECG to the mean cardiac cycle.

6. Initialize the proportionality factors γ for example to one and adjust them once the filter is running.

After these steps are completed, the parameters of the non-linear state-space model used in the extended Kalman filter are determined. The filter operates on a per-cycle basis, since the duration of a cardiac cycle must be known beforehand. A separate Kalman filter is needed for each lead of the ECG.

The procedure described above is applied to an MHD-ECG time series of lead V2 with varying values of $\boldsymbol{\gamma}$. The results are discussed in the next section.

5.5. Application to ECG recordings

The aim of the filtering approach is to reconstruct the cardiac ECG in the time domain such that a clinician can read the status of the heart from the reconstructed ECG. Therefore, the performance of the filter is assessed by comparing time series of final estimates derived from the MHD-ECG to time series of the cardiac ECG recorded in the absence of an external magnetic field. By doing so, results with a varying amount of model-based smoothing controlled by $\boldsymbol{\gamma}$ are obtained and discussed.

In Fig. 5.9, the preprocessed MHD-ECG signal $\breve{\mathcal{E}}(t)$ is shown in blue. This signal is the observation for the extended Kalman filter. The ECG reconstructed by the proposed Kalman procedure is plotted in green. The target of reconstruction, the cardiac ECG, is shown in red.

Results for $\gamma_\omega = \gamma_\nu = \gamma_{\varphi_i} = \gamma_{a_i} = \gamma_{\sigma_i} = 1$ are shown in Fig. 5.9 (a). Much emphasis is placed on the observation, such that the state estimate follows the trend of the observation. Still, the heavy fluctuations of the observation occurring between the T-wave and the P-wave of the successive cycle is reduced.

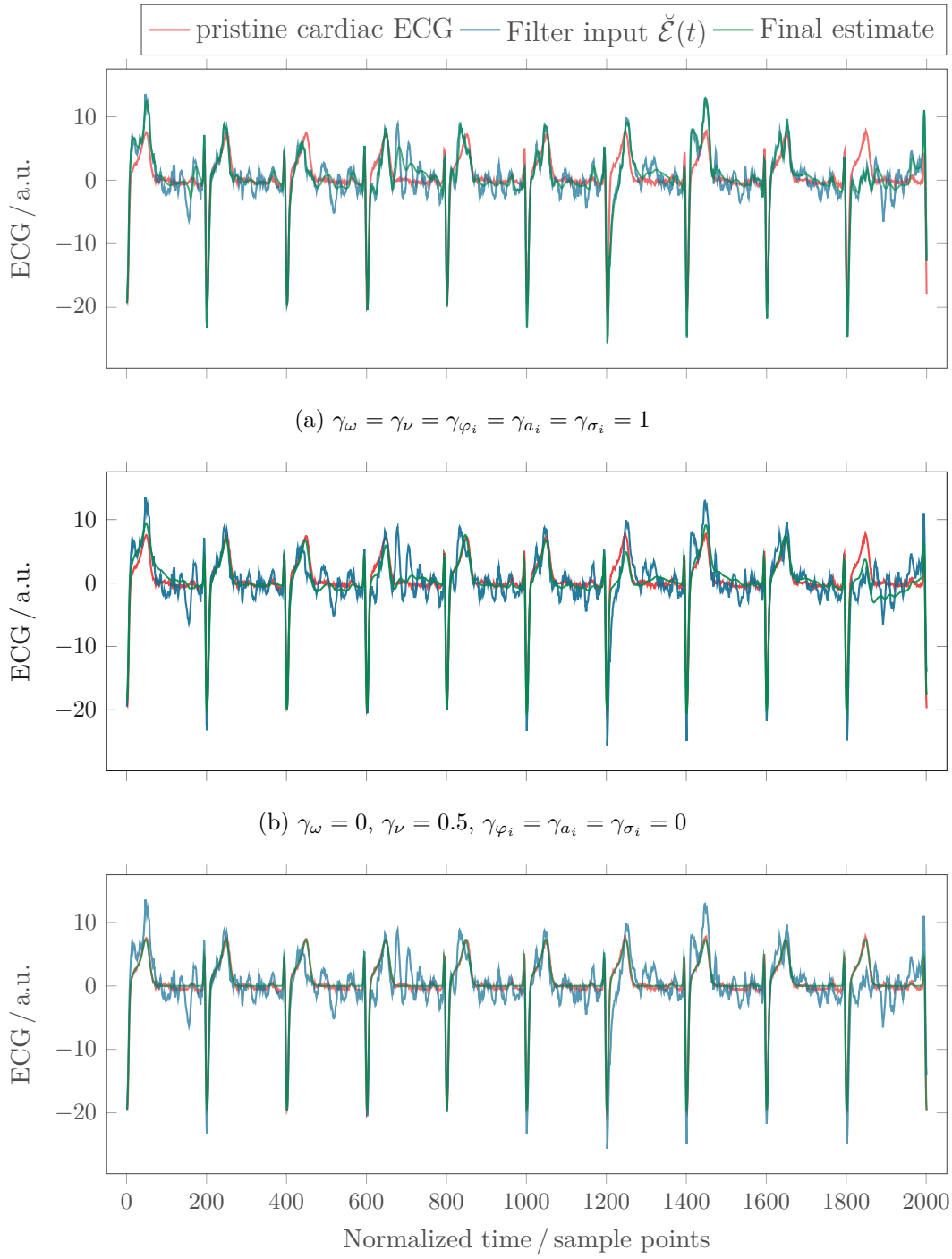

(a) $\gamma_\omega = \gamma_\nu = \gamma_{\varphi_i} = \gamma_{a_i} = \gamma_{\sigma_i} = 1$

(b) $\gamma_\omega = 0$, $\gamma_\nu = 0.5$, $\gamma_{\varphi_i} = \gamma_{a_i} = \gamma_{\sigma_i} = 0$

(c) $\gamma_\omega = \gamma_\nu = \gamma_{\varphi_i} = \gamma_{a_i} = \gamma_{\sigma_i} = 0$

Figure 5.9.: Results obtained from the Kalman filter. The input to the filter, $\breve{\mathcal{E}}(t)$, is depicted in blue. As reference, the cardiac ECG is plotted in red. The final estimate obtained from the filter is given in green. From top to bottom, $\boldsymbol{\gamma}$ varies such that the MHD-ECG is dominant in the top row and basically neglected in the bottom row.

By the choice of $\gamma_\omega = 0$, $\gamma_\nu = 0.5$, $\gamma_{\varphi_i} = \gamma_{a_i} = \gamma_{\sigma_i} = 0$, the impact of the observation onto the state estimates is reduced, as shown in Fig. 5.9 (b). The driving noise in the model of the cardiac ECG remains the only source of uncertainty, such that the estimates follow the cardiac ECG much closer than in the first setting. Still, strong deviations of the observation from the model drive the reconstructed ECG away from the model prediction. This can be seen, e.g., at the T-wave of the first, seventh, and eighth cycle, or the T-P segment starting at the first, third, and fourth cycle. The capability of the estimate to deviate from the model prediction is essential, since otherwise the estimate becomes independent of the measurement. This would render the reconstructed ECG uninformative as it would contain no information about the patient's medical status. Therefore, this setting is a good candidate for application.

In Fig. 5.9 (c), the setting in which the filter output is independent of the measurement is depicted. To this end, $\gamma_\omega = \gamma_\nu = \gamma_{\varphi_i} = \gamma_{a_i} = \gamma_{\sigma_i} = 0$ is chosen. Since the filter is now forced to obey entirely to the model, the reconstructed ECG matches the model output precisely. Even though the ECG seems well reconstructed, this is not a sensible regime of the Kalman filter, since the status of the patient cannot be reflected.

Summary of: PANG: An advanced preamplifier for ECG signals recorded in the MRI environment

The electrocardiogram (ECG) recorded in the presence of a magnetic field as in a magnetic resonance imaging (MRI) scanner is the superposition of the electrical activity of the heart and the magnetohydrodynamic (MHD) effect. The MHD signal can be attributed to the observational noise. Unlike conventional observational noise, the MHD signal is not normal *iid* distributed. Moreover, the MHD effect overlaps with the electrical activity of the heart both in time and frequency domain. Therefore, reconstruction of the cardiac ECG from the MHD-ECG is not a straightforward filtering problem.

In this chapter, a filtering scheme employing the extended Kalman filter is proposed. The Kalman filter is adjusted such that it becomes possible for an operator to specify the amount of model-based smoothing applied to the state estimate. To this end, the ratio between the driving noise and the observational noise covariance is made adjustable. In application, this mechanism can be used to tune the filter towards the quality of measurement. This is demonstrated by the application of the filter to an ECG recorded by standard medical equipment inside a MRI scanner. As the equipment is not designed for the MRI environment, the amount of observational noise consisting of the MHD effect and conventional observational noise, is large. As shown, under certain conditions, the proposed filtering procedure is yet capable of reconstructing the cardiac ECG. With more specialized ECG equipment, it is expected that the reconstruction quality can be improved by placing more emphasis on the measurement.

Summary

Summary

The human brain, the stock-market, or the internet are systems built from entirely different single entities, yet sharing the characteristic, that their respective units exhibit a collective behavior which is fundamentally different to the behavior observed when the respective units are studies in isolation. The appearance of such a collective behavior is termed emergence, and systems showing emergent phenomenon are termed complex systems. Thus, the study of complex systems is the study of the interaction of individual units. This makes network theory a natural tool for visualizing, quantifying, and characterizing complex systems. A network describing entities and their interaction can be constructed from measurements of a complex system. To this end, the recording sites are commonly translated into network nodes, and an interdependence measure is applied to the measurements to infer the network links. The first part of the present thesis deals with the creation of such a network. Therefore, the notation and definition of networks, network models, and network classes is given in Chap. 1.

When constructing and exploring an interaction network, the main challenge is to avoid spurious links, such as indirect links, which do not correspond to a physical connection in the observed system. Bivariate measures establish a link between two nodes exclusively based on measurements from these nodes. In contrast, multivariate measures establish links while accounting for the information present in the entire set of measurements. Networks which are reconstructed by a bivariate measure contain indirect links. The general theoretical argument for the existence of indirect links in such networks is yet missing. In Chap. 2, this argument is developed by exploring the generic relation between bi- and multivariate interdependence measures. Moreover, by expanding the relation of bi- and multivariate measures in a Taylor series, the formation of indirect links is made explicit. The derived argument is independent of the system under investigation. Thus, bivariate measures in general are proven inappropriate for establishing network links.

In Chap. 3, a series of simulations employing the theory derived in Chap. 2 is conducted. The results show the effect of bivariate measures onto the reconstruction of networks on the example of the correlation coefficient. It is demonstrated that, indeed, bivariate measures indicate indirect links. Moreover, network classification

also fails due to effects caused by indirect links. This is demonstrated by a simulation study revealing that random networks are indistinguishable from small-world networks when analyzed by a bivariate interdependence measure.

In the context of dynamic complex systems, interdependence measures assuming independent identically normally distributed states, such as the partial correlation coefficient, become unreliable. Commonly, measurements also contain observational noise. The state-space model is a linear model tailored to measured states which are correlated and impaired by observational noise. States are modeled by an autoregressive process and observational noise is accounted for by a linear stochastic observation equation. By means of the expectation-maximization algorithm, a maximum-likelihood estimator for the parameters of the SSM was constructed. The major drawback of the EM algorithm is its computational complexity resulting in long runtimes. Two optimization strategies that reduce the runtime by about two orders of magnitude are presented in Chap. 4. This major improvement is shown in a simulation study demonstrating the efficiency and accuracy of the implementation.

Based on the parameters of the SSM, interaction measures have been proposed allowing to reliably establish network links from measurements. It is also possible to estimate the underlying state which is not observed directly due to observational noise. To this end, the Kalman filter is the optimal procedure.

Filtering the electrical activity of the heart from an electrocardiogram recorded in the presence of a magnetic field as in a magnetic resonance imaging scanner poses such a state estimation problem. The ECG recorded inside a MRI scanner is the superposition of the electrical activity of the heart and a Hall voltage. The recording of the electrical activity of the heart is termed cardiac ECG, the signal of the Hall voltage magnetohydrodynamic signal, and the recording of the superposition of both signals MHD-ECG. The Hall voltage is evoked by the external magnetic field that results in a Lorentz force acting on ions dissolved in blood. For medical applications it would be desirable to reliably estimate the cardiac ECG from the MHD-ECG. Unfortunately, the MHD signal overlaps with the electrical activity of the heart both in the time and frequency domain. In the SSM, the MHD signal can be treated as observational noise. Then, however, the observational noise can no longer be modeled by a *iid* random variable.

In Chap. 5, a possible solution to this filtering problem is proposed. It employs the extended Kalman filter, which is adjusted to enable an operator to manually specify the amount of model-based smoothing applied to the estimate of the underlying state. The tuning of the filter with regard to the quality of the measurement is demonstrated in an application, in which an ECG is recorded by standard medical equipment inside a MRI scanner. As the equipment is not designed for the MRI environment, the amount of observational noise consisting of the MHD signal and conventional observational noise, is large. Under certain conditions, the proposed filtering procedure is yet capable of reconstructing the cardiac ECG. With more specialized ECG equipment, it is expected that the reconstruction quality of the proposed procedure can be further improved by placing more emphasis on the measurement.

The two topics of this thesis, exploration of the interaction in complex systems as well as state estimation in the context of ECG recordings, are connected by the need to model empirical data by the SSM. Apart from the discussed application, the proposed optimized EM algorithm is useful for all areas of research in need to estimate parameters in the SSM. For example researchers from the financial science have shown interest in this tool.

By modeling the MHD-ECG by the SSM, the SSM is driven out of its area of application supported by theory. Hence, the proposed procedure can only be a phenomenological one. However, with more advanced recording equipment, and thus a better SNR, the design of the procedure allows to expect more reliable state estimates. Thus, it seems well possible to introduce MRI vision to the cath lab in the coming years.

Glossary

Abbreviations

C++	The C++ programming language.
cath lab	Catheterization laboratory.
ECG	Electrocardiogram.
EM	Expectation-maximization.
iid	Independent and identically distributed.
Matlab	A programming language and a trade mark of Mathworks.
MHD	Magnetohydrodynamics.
ML	Maximum-likelihood.
MLE	Maximum-likelihood estimator.
MRI	Magnetic resonance imaging.
SNR	Signal-to-noise ratio.
SSM	State-space model.
VAR	Vector-autoregressive process.

Nomenclature

$\mathfrak{L}$	Set of links in a network.
$\mathfrak{N}$	Set of nodes in a network.
$\boldsymbol{A}$, A	Adjacency matrix and its element.
$\boldsymbol{B}$, B	Incidence matrix and its element.

$\boldsymbol{C}$, C	Transition matrix of a VAR process and its element.
c, C	Local and (average) clustering coefficient.
$\boldsymbol{D}$, D	Distance matrix and its element.
E	Efficiency.
e	Diameter of a network.
f	A probability density function.
G, $G_{N,h}$, $G_{N,M}$	A general network, a regular-ring, or a Erdős-Rényi network.
G_k	The subnetwork containing all direct neighbors of node n_k.
g	Degree of a node, i.e., the number of links connected to a node.
$\boldsymbol{H}$	Power spectral density function.
h	Number of left-hand neighbors of a node.
$\boldsymbol{J}$	Kalman smoother gain.
$\boldsymbol{K}$	Kalman filter gain.
L	Average distance in a network.
$\mathcal{L}$	Log-likelihood function.
l_k, l_{ij}	The k-th link or the link connecting nodes n_i and n_j.
M	Number of links in a network.
m	Number of samples, upper limit of a sum.
N	Number of nodes in a network.
n	A node in a network
$\boldsymbol{O}$, O	Observation matrix in the SSM model and its element.
$\boldsymbol{P}$	Conditional error covariance in the Kalman filter.
$\boldsymbol{\mathcal{P}}$	Sample partial correlation matrix.
p	Order of a VAR process.
$\boldsymbol{Q}$, Q	Covariance matrix of the driving noise of a VAR process and its element.
$\boldsymbol{R}$, R	Covariance matrix of the observational noise in the SSM and its element.
$\boldsymbol{\mathcal{R}}$, $\mathcal{R}$	Sample correlation matrix and its element.
r	Sample correlation coefficient.
$\boldsymbol{X}$, $\boldsymbol{x}$	Some random variable and its realization.
$\boldsymbol{\epsilon}$	Driving noise in the VAR process.
ς	Variable enumerating the iterations in the EM algorithm.
$\boldsymbol{\eta}$	Observational noise in the SSM model.
$\boldsymbol{\Theta}$	The parameter vector usually to be estimated.
λ, γ	Parameters indicative for the small-world property of empirical networks.
$\boldsymbol{\pi}$, π	Partial correlation matrix and its element.
$\boldsymbol{\varrho}$, ϱ	Correlation matrix and its element.
τ	Time-lag variable of the VAR process.
w	A probability.

Bibliography

[1] M. Kollmann, L. Løvdok, K. Bartholomé, J. Timmer, and V. Sourjik. Design principles of a bacterial signalling network. *Nature*, 438(7067):504–507, 2005.

[2] R. Nazmutdinov, M. Bronshtein, T. Zinkicheva, and D. Glukhov. Modeling of electron transfer across electrochemical interfaces: State-of-the art and challenges for quantum and computational chemistry. *Int. J. Quantum Chem.*, 116(3): 189–201, 2016.

[3] G. Aad et al. Observation of a new particle in the search for the Standard Model Higgs boson with the ATLAS detector at the LHC. *Phys. Lett. B*, 716(1):1–29, 2012.

[4] S. Chatrchyan et al. Observation of a new boson at a mass of 125 GeV with the CMS experiment at the LHC. *Phys. Lett. B*, 716(1):30–61, 2012.

[5] P. Anderson. More Is Different. *Science*, 177(4047):393–396, 1972.

[6] Y. Bar-Yam. General features of complex systems. *EOLSS*, 2002.

[7] M. Newman. Resource Letter CS–1: Complex Systems. *Am. J. Phys.*, 79(8): 800–810, 2011.

[8] O. Sporns, D. Chialvo, M. Kaiser, and C. Hilgetag. Organization, development and function of complex brain networks. *Trends. Cogn. Sci.*, 8(9):418–425, 2004.

[9] E. Bullmore and O. Sporns. Complex brain networks: graph theoretical analysis of structural and functional systems. *Nat. Rev. Neurosci.*, 10(3):186–198, 2009.

[10] I. Swameye, T. Müller, J. Timmer, O. Sandra, and U. Klingmüller. Identification of nucleocytoplasmic cycling as a remote sensor in cellular signaling by databased modeling. *Proc. Nat. Acad. Sci.*, 100(3):1028–1033, 2003.

[11] S. Bialonski, M. Horstmann, and K. Lehnertz. From brain to earth and climate systems: Small-world interaction networks or not? *Chaos*, 20(1):013134, 2010.

[12] D. Watts and S. Strogatz. Collective dynamics of 'small-world' networks. *Nature*, 393(6684):440–2, 1998.

[13] G. Liu, J. He, and X. Zhang. Compression approach of street networks considering the structural and functional features of streets. *Int. J. Mod. Phys. B*, 29(31): 1550227, 2015.

[14] K.-C. Pien, K. Han, W. Shang, A. Majumdar, and W. Ochieng. Robustness analysis of the European air traffic network. *Transportmetrica A*, 11(9):772–792, 2015.

[15] A. Tsonis and P. Roebber. The architecture of the climate network. *Physica A*, 333:497–504, 2004.

[16] M. Kazemilari and M. Djauhari. Correlation network analysis for multi-dimensional data in stocks market. *Physica A*, 429:62–75, 2015.

[17] J. Brida, D. Matesanz, and M. Seijas. Network analysis of returns and volume trading in stock markets: The Euro Stoxx case. *Physica A*, 444:751–764, 2016.

[18] W. Mader, D. Feess, R. Lange, D. Saur, V. Glauche, C. Weiller, J. Timmer, and B. Schelter. On the Detection of Direct Directed Information Flow in fMRI. *IEEE J. Sel. Top. Signal Process.*, 2(6):965–974, 2008.

[19] D. Saur, B. Schelter, S. Schnell, D. Kratochvil, H. Küpper, P. Kellmeyer, D. Kümmerer, S. Klöppel, V. Glauche, R. Lange, W. Mader, D. Feess, J. Timmer, and C. Weiller. Combining functional and anatomical connectivity reveals brain networks for auditory language comprehension. *Neuroimage*, 49(4):3187–3197, 2010.

[20] D.-B. den Ouden, D. Saur, W. Mader, B. Schelter, S. Lukic, E. Wali, J. Timmer, and C. Thompson. Network modulation during complex syntactic processing. *Neuroimage*, 59(1):815–823, 2012.

[21] J. Hlinka, D. Hartman, and M. Palus. Small-world topology of functional connectivity in randomly connected dynamical systems. *Chaos*, 22(3):033107, 2012.

[22] W. Mader, M. Mader, J. Timmer, M. Thiel, and B. Schelter. Networks: On the relation of bi-and multivariate measures. *Sci. Rep.*, 5:10805, 2015.

[23] J. Reijneveld, S. Ponten, H. Berendse, and C. Stam. The application of graph theoretical analysis to complex networks in the brain. *Clin. Neurophysiol.*, 118 (11):2317–2331, 2007.

[24] A. Jiménez, K. Tiampo, and A. Posadas. Small world in a seismic network: the California case. *Nonlin. Processes Geophys.*, 15(3):389–395, 2008.

[25] J. Donges, Y. Zou, N. Marwan, and J. Kurths. Complex networks in climate dynamics. *Eur. Phys. J. Special Topics*, 174(1):157, 2009.

[26] F. Salleh, S. Arif, S. Zainudin, and M. Firdaus-Raih. Reconstructing gene regulatory networks from knock-out data using Gaussian Noise Model and Pearson Correlation Coefficient. *Comput. Biol. Chem.*, 59:3–14, 2015.

[27] R. Kalman. A New Approach to Linear Filtering and Prediction Problems. *Trans. ASME J. Basic Eng.*, 82(Series D):35–45, 1960.

[28] M. Eichler. Graphical Modelling of Dynamic Relationships in Multivariate Time Series. In B. Schelter, M. Winterhalder, and J. Timmer, editors, *Handbook of Time Series Analysis,*, chapter 14, pages 335–372. Wiley, 2006.

[29] M. Eichler. A graphical approach for evaluating effective connectivity in neural systems. *Phil. Trans. R. Soc. B*, 360(1457):953, 2005.

[30] B. Schelter, J. Timmer, and M. Eichler. Assessing the strength of directed influences among neural signals using renormalized partial directed coherence. *J. Neurosci. Methods*, 179(1):121–130, 2009.

[31] L. Baccala and K. Sameshima. Partial directed coherence: a new concept in neural structure determination. *Biol. Cyber.*, 84(6):463–474, 2001.

[32] R. Shumway and D. Stoffer. An approach to time series smoothing and forecasting using the EM algorithm. *J. Time. Ser. Anal.*, 3(4):253–264, 1982.

[33] L. Sommerlade, M. Thiel, M. Mader, W. Mader, J. Timmer, B. Platt, and B. Schelter. Assessing the strength of directed influences among neural signals: An approach to noisy data. *J. Neurosci. Methods*, 239:47–64, 2015.

[34] W. Mader, Y. Linke, M. Mader, L. Sommerlade, J. Timmer, and B. Schelter. A numerically efficient implementation of the expectation maximization algorithm for state space models. *Appl. Math. Comp.*, 241:222–232, 2014.

[35] S. Strogatz. Exploring Complex Networks. *Nature*, 410:268–276, 2001.

[36] S. Mei, N. Zarrabi, M. Lees, and P. Sloot. Complex agent networks: An emerging approach for modeling complex systems. *Appl. Soft Comp.*, 37:311–321, 2015.

[37] K. Thakur, C. Revie, D. Hurnik, Z. Poljak, and J. Sanchez. Analysis of swine movement in four Canadian regions: network structure and implications for disease spread. *Transbound. Emerg. Diseases*, 63(1):e14–16, 2014.

[38] R. Diestel. *Graph Theory.* Springer, 3 edition, 2005.

[39] S. Boccaletti, V. Latora, Y. Moreno, M. Chavez, and D. Hwang. Complex networks: Structure and dynamics. *Phys. Rep.*, 424(4-5):175–308, 2006.

[40] R. Diestel. *Graph Theory*, chapter 1, pages 1–30. Springer, 3 edition, 2005.

[41] L. Euler. Solutio problematis ad geometriam situs pertinentis. *CASP*, 8:128–140, 1736.

[42] M. Newman. The structure and function of complex networks. *SIAM Rev.*, 45 (2):167–256, 2003.

[43] V. Latora and M. Marchiori. Efficient behavior of small-world networks. *Phys. Rev. Lett.*, 87(19):198701, 2001.

[44] V. Latora and M. Marchiori. Economic small-world behavior in weighted networks. *Eur. Phys. J. B*, 32(2):249–263, 2003.

[45] M. Newman, S. Strogatz, and D. Watts. Random graphs with arbitrary degree distributions and their applications. *Phys. Rev. E*, 64:26118, 2001.

[46] A. Barrat and M. Weigt. On the properties of small-world network models. *Eur. Phys. J. B*, 13(3):547–560, 2000.

[47] P. Erdős and A. Rényi. On random graphs. *Publ. Math.*, 6:290–297, 1959.

[48] P. Erdős and A. Rényi. On the Evolution of Random Graphs. In *Publication of the Mathematical Institute of the Hungarian Academy of Sciences*, pages 17–61, 1960.

[49] T. Austin, R. Fagen, W. Penney, and J. Riordan. The Number of Components in Random Linear Graphs. *Ann. Math. Statist.*, 30(3):747–754, 1959.

[50] M. Newman. Models of the Small World. *J. Stat. Phys.*, 101(3-4):819–841, 2000.

[51] S. Milgram. The Small-World Problem. *Psychol. Today*, 1(1):61–67, 1967.

[52] I. Sola de Pool and M. Kochen. Contacts and influence. *Soc. Netw.*, 1(1):5–51, 1978.

[53] M. Newman and D. Watts. Renormalization group analysis of the small-world network model. *Phy. Lett. A*, 263(4–6):341–346, 1999.

[54] K. Schindler, S. Bialonski, M. Horstmann, C. Elger, and K. Lehnertz. Evolving functional network properties and synchronizability during human epileptic seizures. *Chaos*, 18(3):033119, 2008.

[55] S. Abe and N. Suzuki. Complex-network description of seismicity. *Nonlin. Processes Geophys.*, 13(2):145–150, 2006.

[56] G.-G. Ha, J. Lee, and A. Nobi. Threshold network of a financial market using the P-value of correlation coefficients. *J. Korean Phys. Soc.*, 66(12):1802, 2015.

[57] K. Steinhaeuser, N. Chawla, and A. Ganguly. Complex networks as a unified framework for descriptive analysis and predictive modeling in climate science. *Stat. Anal. Data Min.*, 4(5):497–511, 2011.

[58] R. Cazabet, H. Takeda, and M. Hamasaki. Characterizing the nature of interactions for cooperative creation in online social networks. *Soc. Netw. Anal. Min.*, 5(1):1–17, 2015.

[59] D. Ferreira, A. Papa, and R. Menezes. Small world picture of worldwide seismic events. *Physica A*, 408:170–180, 2014.

[60] T. Ferrée, M. Clay, and D. Tucker. The spatial resolution of scalp EEG. *Neurocomputing*, 38-40:1209–1216, 2001.

[61] R. Ramb, M. Eichler, A. Ing, M. Thiel, C. Weiller, C. Grebogi, C. Schwarzbauer, J. Timmer, and B. Schelter. The impact of latent confounders in directed network analysis in neuroscience. *Phil. Trans. R. Soc. A*, 371(1997):20110612, 2013.

[62] D. Brillinger. *Time Series: Data Analysis and Theory*, chapter 8, pages 286–290. Classics in Applied Mathematics. SIAM, 2001.

[63] J. Whittaker. *Graphical Models in Applied Multivariate Statistics*, chapter 6, pages 158–159. Wiley, 1995.

[64] R. Shumway and D. Stoffer. *Time Series Analysis and its Applications*, chapter B.2, pages 528–531. Springer Texts in Statistics. Springer, 3 edition, 2011.

[65] R. Dahlhaus. Graphical interaction models for multivariate time series. *Metrika*, 51(2):157–172, 2000.

[66] S. Lauritzen. *Graphical Models*. Oxford Statistical Science Series. Oxford University Press, 1996.

[67] J. Whittaker. *Graphical Models in Applied Multivariate Statistics*, chapter 5, pages 120–147. Wiley, 1995.

[68] A. Zalesky, A. Fornito, and E. Bullmore. On the use of correlation as a measure of network connectivity. *Neuroimage*, 60(4):2096–2106, 2012.

[69] T. Hastie and R. Tibshirani. Generalized additive models. *Stat. Sci.*, 1(3): 297–318, 1986.

[70] J. Whittaker. *Graphical Models in Applied Multivariate Statistics*, chapter 3, pages 71–77. Wiley, 1995.

[71] S. Lauritzen and D. Spiegelhalter. Local computations with probabilities on graphical structures and their application to expert systems. *J. R. Stat. Soc. B*, 50(2):157–224, 1988.

[72] L. Held and D. Sabanés Bové. *Applied Statistical Inference: Likelihood and Bayes*, chapter 2, pages 13–50. Springer, 2013.

[73] L. Held and D. Sabanés Bové. *Applied Statistical Inference: Likelihood and Bayes*, chapter 3, pages 51–78. Springer, 2013.

[74] R. Fisher. On the "Probable Error"of a Coefficient of Correlation deduced from a Small Sample. *Metron*, 1:3–32, 1920.

[75] R. Fisher. The Distribution of the Partial Correlation Coefficient. *Metron*, 3: 329–332, 1924.

[76] S. Ponten, F. Bartolomei, and C. Stam. Small-world networks and epilepsy: Graph theoretical analysis of intracerebrally recorded mesial temporal lobe seizures. *Clin. Neurophysiol.*, 118(4):918–927, 2007.

[77] S. Yu, D. Huang, W. Singer, and D. Nikolić. A small world of neuronal synchrony. *Cereb. Cortex*, 18(12):2891–2901, 2008.

[78] L. Bettencourt, G. Stephens, M. Ham, and G. Gross. Functional structure of cortical neuronal networks grown in vitro. *Phys. Rev. E*, 75(2):021915, 2007.

[79] D. Bassett and E. Bullmore. Small-World Brain Networks. *Neuroscientist*, 12 (6):512–523, 2006.

[80] D. Ferreira, A. Papa, and R. Menezes. On the agreement between small-world-like OFC model and real earthquakes. *Phy. Lett. A*, 379(7):669–675, 2015.

[81] A. Tsonis, K. Swanson, and G. Wang. On the role of atmospheric teleconnections in climate. *J. Climate*, 21(12):2990–3001, 2007.

[82] W. Liang, Y. Wang, Y. Shi, and G. Chen. Co-occurrence network analysis of Chinese and English poems. *Physica A*, 420:315–323, 2015.

[83] J. Chakareski. Cost and profit driven cloud-P2P interaction. *Peer-to-Peer Netw. Appl.*, 8(2):244, 2015.

[84] G. Gilbert. Positive definite matrices and Sylvester's criterion. *Am. Math. Monthly*, 98(1):44–46, 1991.

[85] H. Schwarz and N. Köckler. *Numerische Mathematik*, chapter 2, pages 30–61. Lehrbuch: Mathematik. Teubner, 8 edition, 2011.

[86] J. Stoer and R. Bulirsch. *Introduction to Numerical Analysis*, chapter 8, pages 623–629. Texts in Applied Mathematics. Springer, 2002.

[87] D. Watts. *Small Worlds – The Dynamics of Networks between Order and Randomneess*. Princeton University Press, 1999.

[88] S. Maslova, K. Sneppenb, and A. Zaliznyaka. Detection of topological patterns in complex networks: correlation profile of the internet. *Physica A*, 333:529–540, 2004.

[89] R. Shumway and D. Stoffer. *Time Series Analysis and its Applications*, chapter 6, pages 319–344. Springer Texts in Statistics. Springer, 3 edition, 2011.

[90] R. Kalman and R. Bucy. New results in linear filtering and prediction theory. *J. Fluids Eng.*, 83(1):95–108, 1961.

[91] M. Priestely. *Spectral Analysis and Time Series*, chapter 9, pages 685–689. Probability and Mathematical Statistics. Acad. Press, 6 edition, 1989.

[92] K. Petersen and M. Pedersen. The matrix cookbook, 2012.

[93] A. Einstein. On the movement of small particles suspended in stationary liquids required by the molecular-kinetic theory of heat. *Ann. Phys.*, 17:549–650, 1905.

[94] R. Fisher. On an absolute criterion for fitting frequency curves. *Mess. Math.*, 41:155–160, 1912.

[95] J. Aldrich. RA Fisher and the making of maximum likelihood 1912-1922. *Stat. Sci.*, 12(3):162–176, 1997.

[96] M. Priestely. *Spectral analysis and time series*, chapter 5, pages 304–310. Probability and Mathematical Statistics. Acad. Press, 6 edition, 1989.

[97] A. Dempster, N. Laird, and D. Rubin. Maximum likelihood from incomplete data via the EM algorithm. *J. R. Stat. Soc. B*, 39(1):1–38, 1977.

[98] F. Schweppe. Evaluation of likelihood functions for Gaussian signals. *IEEE Trans Inf. Theory*, 11(1):61–70, 1965.

[99] A. Jazwinski. *Stochastic Processes and Filtering Theory*. Number 64 in Mathematics in Science and Engineering. Acad. Press, 1970.

[100] M. Grewal and A. Andrews. Applications of Kalman filtering in aerospace 1960 to the present [historical perspectives]. *IEEE Trans. Contr. Sys.*, 30(3):69–78, 2010.

[101] H. Rauch, F. Tung, and C. Striebel. Maximum Likelihood Estimates of Linear Dynamic Systems. *AIAA*, 3(8):1445–1450, 1965.

[102] L. Sommerlade. *Time-resolved estimation of direct directed influences*. PhD thesis, University of Freiburg, 2013.

[103] M. Priestely. *Spectral Analysis and Time Series*, chapter 4, pages 206–218. Probability and Mathematical Statistics. Acad. Press, 6 edition, 1989.

[104] C. Wu. On the convergence properties of the EM algorithm. *Ann. Stat.*, 11(1): 95–103, 1983.

[105] A. Raue, M. Schilling, J. Bachmann, A. Matteson, M. Schelker, D. Kaschek, S. Hug, C. Kreutz, B. Harms, F. Theis, U. Klingmüller, and J. Timmer. Lessons learned from quantitative dynamical modeling in systems biology. *PloS One*, 8 (9):e74335, 2013.

[106] J. Oster, M. Geist, O. Pietquin, and G. Clifford. Filtering of Pathological Ventricular Rhythms during MRI Scanning. *Int. J. Bioelectromagn.*, 15(1):54–59, 2013.

[107] D. Schnack. *Lectures in Magnetohydrodynamics: With an Appendix on extended MHD*, volume 780 of *Lecture Notes in Physics*, chapter 1, pages 1–4. Springer, 2009.

[108] D. Abdallah, A. Drochon, V. Robin, and O. Fokapu. Effects of static magnetic field exposure on blood flow. *Eur. Phys. J. Appl. Phys.*, 45:11301, 2009.

[109] D. Schnack. *Lectures in Magnetohydrodynamics: With an Appendix on extended MHD*, volume 780 of *Lecture Notes in Physics*. Springer, 2009.

[110] A. Kolin. An Alternating Field Induction Flow Meter of High Sensitivity. *Rev. Sci. Instrum.*, 16(5):109–116, 1945.

[111] T. Tenforde. Magnetically induced electric fields and currents in the circulatory system. *Prog. Biophys. Mol. Biol.*, 87:279–288, 2005.

[112] A. Gupta, A. Weeks, and S. Richie. Simulation of Elevated T-Waves of an ECG Inside a Static Magnetic Field (MRI). *IEEE Trans. Biomed. Eng.*, 55(7): 1890–1896, 2008.

[113] Y. Kinouchi, H. Yamaguchi, and T. Tenforde. Theoretical Analysis of Magnetic Field Interactions With Aortic Blood Flow. *Bioelectromagnetics*, 17:21–32, 1996.

[114] J. Krug, G. Rose, D. Stucht, G. Clifford, and J. Oster. Filtering the Magneto-hydrodynamic Effect from 12-lead ECG Signals using Independent Component Analysis. *Comput. Cardiol.*, 39:589–592, 2012.

[115] J. Krug and G. Rose. Magnetohydrodynamic Distortions of the ECG in Different MR Scanner Configurations. *Comput. Cardiol.*, 38:769–772, 2011.

[116] J. Oster, O. Pietquin, M. Kraemer, and J. Felblinger. Nonlinear Bayesian Filtering for Denoising of Electrocardiograms Acquired in a Magnetic Resonance Environment. *IEEE Trans. Biomed. Eng.*, 57(7):1628–1638, 2010.

[117] S. Julier and J. Uhlmann. A new extension of the Kalman filter to nonlinear systems. In *11th International Symposium on Aerospace/Defense Sensing* , pages 182–193, 1997.

[118] G. Welch and G. Bishop. An Introduction to the Kalman Filter. Technical report, University of North Carolina, 1997.

[119] P. McSharry, G. Clifford, L. Tarassenko, and L. Smith. A dynamical model for generating synthetic electrocardiogram signals. *IEEE Trans. Biomed. Eng.*, 50 (3):289–294, 2003.

[120] R. Sameni, M. Shamsollahi, C. Jutten, and G. Clifford. A Nonlinear Bayesian Filtering Framework for ECG Denoising. *IEEE Trans. Biomed. Eng.*, 54(12): 2172–85, 2007.

Acknowledgment

First of all, I thank my supervisors Prof. Dr. Jens Timmer and Prof. Dr. Björn Schelter for providing me with the topic of my thesis and for giving me enough latitude to follow my own ideas. I especially thank Jens Timmer for his valuable comments and the interesting discussions we had. I thank Björn Schelter for introducing me to Prof. Dr. Bruce J. Gluckman. Jens Timmer and Björn Schelter made it possible for me to stay for seven months at the Pennsylvania State University in State College, Pennsylvania, with Bruce Gluckman. This was a great experience which I really do not want to miss.

Furthermore, I thank all my colleagues for being great people. First of all, I thank Dr. Madineh Sarvestani for her unbelievable support at Pennsylvania State University. Thank you for letting us stay at your place. It was a priceless experience. Back in Germany, I thank all members of Jens Timmer's group for the great working atmosphere. You are really a cool bunch of guys! I especially thank Dr. Clemens Kreutz, Christian Tönsing, Dr. Daniel Kaschek, Dr. Mirjam Fehling-Kaschek, and Marcus Rosenblatt for proof-reading this thesis. I want to thank Berenika Siddons, Dr. Elke Martinez, and Monika Hattenbach for the relentless commitment in mastering all administrative challenges, ranging from formal changes of position to travel expense accounting.

Last but certainly not least, I would like to express my gratitude to my family and friends. I thank my parents Ute and Dr. Bruno Mader for always believing in me. They provided me with all the support I could possibly imaging, not only during my time at university, but whenever necessary. Thank you for being there. I also thank my parents-in-law for giving every help they can. I had a good time last summer writing up parts of this thesis at your place. I especially thank my daughter Leana for making me laugh every day. It is wonderful to see you grow and to witness how you explore the world so open minded as only a child can do. Thank you for the happiness and joy you keep bringing into my life. Particularly, I thank my wonderful wive Malenka Mader, for her steady support and for being a great discussion partner and valuable college. Thank you for sharing your time with me.

Appendix

Appendix A.

Supplement to Network reconstruction and classification

A.1. Definition of the average distance

The average distance can be defined in slightly different ways. While the general discussion given in the main body is sufficient for this thesis, the different definitions are presented in this section for completeness

In undirected networks, the lower triangular of $\boldsymbol{D}$ is enough to determine the average distance. Two definitions for the average distance

$$L_\mathrm{i} = \frac{2}{N^2} \sum_{i \geq j}^{N} D_{ij} \,, \quad \text{or} \tag{A.1a}$$

$$L_\mathrm{e} = \frac{2}{N(N-1)} \sum_{i > j}^{N} D_{ij} \tag{A.1b}$$

are used. While in Eq. (A.1a) the diagonal elements $D_{ii} = 0$ are included, in Eq. (A.1b) they are not. The two definitions differ by the factor $L_\mathrm{i}/L_\mathrm{e} = (N-1)/N = 1 - 1/N$ which is in $o\,(1/N)$ [11]. In literature [11, 42], also $\tilde{L}_\mathrm{i} = 2/[N(N+1)] \sum_{i \geq j} D_{ij}$ is used, counting the diagonal entries twice.

In directed networks the complete matrix $\boldsymbol{D}$ must be traversed, leading to

$$L_\mathrm{i} = \frac{1}{N^2} \sum_{i,j=1}^{N} D_{ij} \,, \quad \text{or} \quad L_\mathrm{e} = \frac{1}{N(N-1)} \sum_{i \neq j}^{N} D_{ij} \tag{A.2}$$

depending on whether or not diagonal elements are considered.

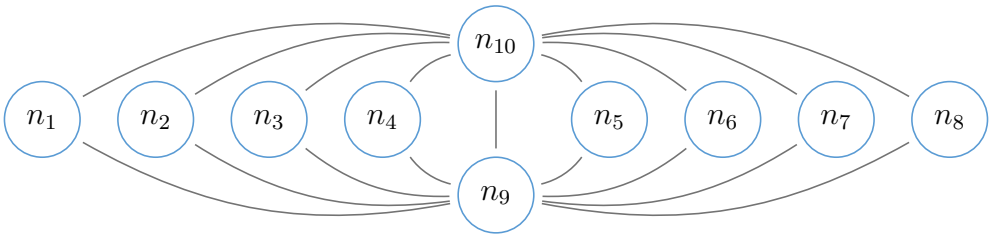

Figure A.1.: In this network, the clustering coefficient converges to one while the transitivity converges to zero with increasing number of nodes. The clustering coefficient evaluates the existence of triangles centered around a node, leading to $c_k = 1$ for $k = 1, \ldots, 8$. The transitivity quantifies if from the existence of a chain of lengths three, e.g. n_1, n_{10}, n_2, it can be concluded that n_1 and n_2 are adjacent. Such behavior is generally referred to as transitive. The figure is taken from [44].

A.2. Transitivity

In Sec. 1.2.3, the local clustering coefficient is introduced as a measure for the local connectivity in a network. Rooted in the sociology literature, the transitivity

$$\boldsymbol{R} = \frac{3 \times \#\text{ of triangles in G}}{\#\text{ of connected triples of nodes in G}} \tag{A.3}$$

is another measure on how well a network is connected locally [42, 45]. A set of three nodes form a *connected triple* when connected by at least two links, and a *closed triple* or *triangle* when connected by three links. The transitivity quantifies if the start and end nodes of a three node chain are also connected, in which case the linkage is transitive.

In contrast to the local clustering coefficient which acts on the nearest neighbors of a node, the transitivity takes into account the connection status of nearest and second nearest neighbors of a node. Thus, the local clustering coefficient of n_1 of Fig. A.1 quantifies if n_9 and n_{10} are connected, but since e.g. n_2 is no direct neighbor of n_1, the connectivity of n_1 and n_2 is irrelevant for the (local) clustering coefficient. However, n_1, n_{10}, n_2 form a connected triple, and therefore appear in the denominator of the transitivity. In fact, for this network, the clustering coefficient converges to one with increasing number of nodes while the transitivity converges to zero [44].

A.3. Average distance in a regular ring network

In Sec. 1.3.1, the scaling of the average distance in a regular ring network is given. This sections presents the exact equations for the average distance and is completed by deriving the scaling behavior. The average distance in $G_{N,h}$ is obtained from the first column $\boldsymbol{D}_1$ of its distance matrix $\boldsymbol{D}$. An expression L^{o} for N odd and L^{e} for N even is derived.

Odd number of nodes First, N odd* and $(N-1)/(2h) \in \mathbb{Z}$ is considered. The lengths of the geodesics recorded in $\boldsymbol{D}_1$ are $\{1, 2, \ldots, (N-1)/(2h)\}$, every value occurring $2h$ times. Using $\sum_{i=1}^{n} i = n(n+1)/2$, the sum over $\boldsymbol{D}_1$ reads

$$\tilde{L}^{\mathbb{Z}\mathrm{o}}(N) = 2h\left(\frac{N-1}{2h}+1\right)\frac{N-1}{4h}\,, \tag{A.4}$$

and the average distance

$$L_{\mathrm{i}}^{\mathbb{Z}\mathrm{o}}(N) = \left(\frac{N-1}{4h}+\frac{1}{2}\right)\frac{N-1}{N}\,, \quad \text{if } D_{ii} \text{ is included} \tag{A.5}$$

$$L_{\mathrm{e}}^{\mathbb{Z}\mathrm{o}}(N) = \frac{N-1}{4h}+\frac{1}{2}\,, \quad \text{if } D_{ii} \text{ is excluded} \tag{A.6}$$

is found.

To derive the general expression for N odd†, $(N-1)/(2h) \in \mathbb{Q}$ is considered. For the first

$$\tilde{N} = \left\lfloor \frac{N-1}{2h} \right\rfloor 2h+1 \tag{A.7}$$

nodes Eq. (A.4) applies. Integer division is denoted by the floor function $\lfloor\cdot\rfloor$. The remaining $N-\tilde{N}$ nodes contribute a path of length $(\tilde{N}-1)/(2h)+1$ each. With

$$\lambda(\tilde{N}) = (\tilde{N}-1)/(2h)+1 \tag{A.8}$$

the sum over $\boldsymbol{D}_1$ reads

$$\begin{aligned}
\tilde{L}^{\mathrm{o}}(N) &= \tilde{L}^{\mathbb{Z}\mathrm{o}}(\tilde{N}) + \left(\frac{\tilde{N}-1}{2h}+1\right)(N-\tilde{N}) \\
&= 2h\left(\frac{\tilde{N}-1}{2h}+1\right)\frac{\tilde{N}-1}{4h} + \left(\frac{\tilde{N}-1}{2h}+1\right)(N-\tilde{N}) \\
&= \lambda(\tilde{N})\left(\frac{\tilde{N}-1}{2}+N-\tilde{N}\right) \\
&= \frac{\lambda(\tilde{N})}{2}(2N-\tilde{N}-1)\,.
\end{aligned} \tag{A.9}$$

If D_{ii} is excluded, the average distance

$$L_{\mathrm{e}}^{\mathrm{o}}(N) = L_{\mathrm{e}}^{\mathrm{zo}}(\tilde{N})\frac{2N-\tilde{N}-1}{N-1} \tag{A.10}$$

$$= L_{\mathrm{e}}^{\mathrm{zo}}(\tilde{N})\left(1+\frac{N-\tilde{N}}{N-1}\right) \tag{A.11}$$

*Example: $N=9$, $h=2$, $\boldsymbol{D}_1 = (0,1,1,2,2,2,2,1,1)^{\mathrm{T}}$

†Example: $N=15$, $h=3$, $\boldsymbol{D}_1 = (0,1,1,1,2,2,2,3,3,2,2,2,1,1,1)^{\mathrm{T}}$

can be formulated in terms of $L_{\mathrm{e}}^{\mathbb{Z}\mathrm{o}}(\tilde{N}) = \lambda(\tilde{N})/2$ [$\rightarrow$ Eq. (A.6)]. As to be expected, $L_{\mathrm{e}}^{\mathbb{Z}\mathrm{o}}$ is the special case of $L_{\mathrm{e}}^{\mathrm{o}}$ for $N = \tilde{N}$.

The average distance including the diagonal can be expressed in terms of $L_{\mathrm{i}}^{\mathbb{Z}\mathrm{o}}(\tilde{N})$ as

$$L_{\mathrm{i}}^{\mathrm{o}}(N) = L_{\mathrm{i}}^{\mathbb{Z}\mathrm{o}}(\tilde{N}) \left(\frac{\tilde{N}}{\tilde{N}-1}\right) \left(\frac{2N-\tilde{N}-1}{N}\right) \tag{A.12}$$

$$= L_{\mathrm{i}}^{\mathbb{Z}\mathrm{o}}(\tilde{N}) \left(\frac{\tilde{N}}{N}\right) \left(\frac{2N}{\tilde{N}-1} - 1\right), \tag{A.13}$$

which includes $L_{\mathrm{i}}^{\mathbb{Z}\mathrm{o}}(\tilde{N})$ as the special $N = \tilde{N}$.

Even number of nodes If N is even[‡] and $N/2h \in \mathbb{Z}$, the largest geodesic is of length $N/(2h)$ occurring $2h-1$ times. Therefore, the sum over $\boldsymbol{D}_1$ is

$$\tilde{L}^{\mathbb{Z}\mathrm{e}}(N) = 2h \left(\frac{N}{2h} + 1\right) \frac{N}{4h} - \frac{N}{2h} \tag{A.14}$$

$$= \left(\frac{N-2}{4h} + \frac{1}{2}\right) N, \tag{A.15}$$

resulting in the expressions

$$L_{\mathrm{i}}^{\mathbb{Z}\mathrm{e}}(N) = \frac{N-2}{4h} + \frac{1}{2}, \qquad \text{if } D_{ii} \text{ is included} \tag{A.16}$$

$$L_{\mathrm{e}}^{\mathbb{Z}\mathrm{e}}(N) = \left(\frac{N-2}{4h} + \frac{1}{2}\right) \frac{N}{N-1}, \quad \text{if } D_{ii} \text{ is excluded.} \tag{A.17}$$

for the average distance.

In the case in which N is even[§] and $N/(2h) \in \mathbb{Q} \setminus \mathbb{Z}$, for the first

$$\tilde{N} = \left\lfloor \frac{N}{2h} \right\rfloor 2h \tag{A.18}$$

nodes Eq. (A.15) applies. Because N and $\tilde{N}$ are both even but not equal, $N - \tilde{N}$ is at least 2. The first of those extra nodes contributes a geodesic of length $\tilde{N}/(2h)$, each other a geodesic of length $\tilde{N}/(2h) + 1$. The total contribution of all extra nodes is

$$\Delta\check{L}^{\mathrm{e}} = \frac{\tilde{N}}{2h} + \left(\frac{\tilde{N}}{2h} + 1\right)(N - \tilde{N} - 1). \tag{A.19}$$

The correction does not vanish for $N = \tilde{N}$, as

$$\Delta\check{L}^{\mathrm{e}} = \frac{N}{2h} - \frac{\tilde{N}}{2h} - 1 \neq 0. \tag{A.20}$$

[‡]Example: $N = 8$, $h = 2$, $\boldsymbol{D}_1 = (0,1,1,2,2,2,1,1)^{\mathrm{T}}$

[§]Example: $N = 14$, $h = 3$, $\boldsymbol{D}_1 = (0,1,1,1,2,2,2,3,2,2,2,1,1,1)^{\mathrm{T}}$

This implies, than Eq. (A.19) cannot be used to formulate an expression independent of $N/(2h)$. The reason becomes evident when combining Eq. (A.14) with Eq. (A.19)

$$\check{L}^{\mathrm{e}} = \left(\frac{N}{2h}+1\right)\frac{N}{2} - \frac{N}{2h} + \frac{\tilde{N}}{2h} + \left(\frac{\tilde{N}}{2h}+1\right)(N-\tilde{N}-1) \tag{A.21}$$

$$= \left(\frac{N}{2h}+1\right)\frac{N}{2} + \left(\frac{\tilde{N}}{2h}+1\right)(N-\tilde{N}-1)\,. \tag{A.22}$$

The term $-\frac{N}{2h}$ needed for $N/(2h) \in \mathbb{Z}$ is compensated by $\Delta\check{L}^{\mathrm{e}}$ in any case. The remaining correction is a multiple of $\tilde{N}/(2h)+1$, introducing an offset of one as shown in Eq. (A.20).

To overcome this deficiency, Eq. (A.19) can be expressed as

$$\Delta\tilde{L}^{\mathrm{e}} = \frac{\tilde{N}}{2h} + \left[\frac{\tilde{N}}{2h} + 1 - \Theta\left(\tilde{N}-N\right)\right](N-\tilde{N}-1)\,, \tag{A.23}$$

where $\Theta(\cdot)$ denotes the Heaviside step function. The average distance including the diagonal elements becomes

$$L_{\mathrm{i}}^{\mathrm{e}}(N) = L_{\mathrm{i}}^{\mathbb{Z}\mathrm{e}}(\tilde{N})\frac{\tilde{N}}{N} + \frac{\tilde{N}}{2hN} + \left[\frac{\tilde{N}}{2h} + 1 - \Theta\left(\tilde{N}-N\right)\right]\frac{N-\tilde{N}-1}{N}\,, \tag{A.24}$$

and without diagonal elements

$$L_{\mathrm{e}}^{\mathrm{e}} = L_{\mathrm{e}}^{\mathbb{Z}\mathrm{e}}(\tilde{N})\frac{\tilde{N}-1}{N-1} + \frac{\tilde{N}}{2h(N-1)} + \left[\frac{\tilde{N}}{2h} + 1 - \Theta\left(\tilde{N}-N\right)\right]\frac{N-\tilde{N}-1}{N-1}\,. \tag{A.25}$$

Both expressions simplify to $L_{\mathrm{i}}^{\mathbb{Z}\mathrm{e}}$ or $L_{\mathrm{e}}^{\mathbb{Z}\mathrm{e}}$, respectively, for $N=\tilde{N}$.

Scaling of $L(N)$ An important feature of a network class is the scaling of its properties. The corrections to the respective integer cases given in Eqs. (A.11), (A.13), (A.24) (A.25) only involve terms of the form $\tilde{N}/N$ and $(N-\tilde{N})/N$. The difference

$$N-\tilde{N} = \begin{cases} (N-1) \bmod 2h & \text{if } N \text{ is odd} \\ N \bmod 2h & \text{if } N \text{ is even} \end{cases} \tag{A.26}$$

is in $[0, 2h-2]$ only traversing even numbers, since both arguments of the modulo operation are even. Therefore, the contribution of

$$\frac{\tilde{N}}{N} = 1 - \frac{2(h+1)}{N} \quad \text{and} \quad \frac{N-\tilde{N}}{N} = \frac{2(h+1)}{N}\,, \tag{A.27}$$

vanishes as N increases. The scaling of all general expressions is hence inherited from their integer counterparts, Eqs. (A.5), (A.6), (A.16) (A.17). Using L to denote the average distance irrespective of N being even or odd,

$$L \propto \frac{N}{4h} = \frac{N}{2g_k} \tag{A.28}$$

scales linearly with N [46]. For this reason, the average distance in regular networks is considered large.

A.4. Scaling of the average distance in random networks

In this section, the scaling of the average distance with the number of nodes N in the model of random networks [→ Sec. 1.3.2] is derived. As a preliminary step, the scaling of the diameter $e(N)$ is assessed, as it defines an upper bound for $L(N)$.

Consider a network from the Erdős-Rényi model with N nodes and mean degree $\mathrm{E}(g_k) = z$, defining $M = Nz/2$. Thus, node n_k is expected to have distance one to z other nodes, distance two to about z^2, distance three to about z^3, and distance s to about z^s nodes [50]. As the diameter is the largest distance in the network, the sum over all distance up to e

$$\sum_{i=1}^{e} z^i = N \tag{A.29}$$

equals the total number of nodes in the network. This sum can be written as the partial sum of the geometric series by letting i start at zero

$$\sum_{i=0}^{e} z^i = \frac{z^{e+1} - 1}{z - 1} = N + 1 \tag{A.30}$$

and adapting the right hand side accordingly. The diameter $e(N)$ as a function of N is then found by rearranging Eq. (A.30) as

$$\begin{aligned}
e(N) &= \log_z[(N+1)(z-1)+1] - 1 && \text{(A.31)}\\
&= \log_z[(N+1)(z-1)] + \log_z\left[1 + \frac{1}{(N+1)(z-1)}\right] - 1 && \text{(A.32)}\\
&\approx \log_z[(N+1)(z-1)] - 1 && \text{(A.33)}\\
&= \log_z(N) + \log_z[1+1/N] + \log_z(z) + \log_z[1+1/z] - 1 && \text{(A.34)}\\
&= \log_z(N) + \log_z[1+1/N] + \log_z[1+1/z] - 1 && \text{(A.35)}\\
&\approx \log_z(N) - 1\,, && \text{(A.36)}
\end{aligned}$$

from which the number of nodes as a function of the diameter

$$N(e) \approx z^{(e+1)}\,. \tag{A.37}$$

is derived. This derivation does not take into account that some of the nodes of distance s might coincide with nodes of distance $\tilde{s} < s$. For $N \gg z$, this imponderability becomes negligible and has therefore no influence on the scaling behavior.

Turning to the average distance, the sum over the lengths of all paths in the network

$$\tilde{L}(N) = \sum_{i=0}^{e(N)} iz^i \tag{A.38}$$

$$= \frac{ez^{e+2} - (e+1)z^{e+1} + z}{(z-1)^2} \tag{A.39}$$

$$= z^{(e+1)} \left(\frac{ez - (e+1) + z^{-e}}{(z-1)^2} \right) \tag{A.40}$$

$$= z^{(e+1)} \left(\frac{e(z-1) - 1 + z^{-e}}{(z-1)^2} \right) \tag{A.41}$$

$$= z^{(e+1)} \left(\frac{e}{z-1} + \frac{z^{-e} - 1}{(z-1)^2} \right) \tag{A.42}$$

has to be normalize by $N \approx z^{(t+1)}$ [→ Eq. (A.37)]. Therefore, the average distance

$$L(N) = \frac{\tilde{L}(N)}{N} \tag{A.43}$$

$$\approx \frac{e(N)}{z-1} + \frac{z^{-e} - 1}{(z-1)^2} \tag{A.44}$$

$$\approx \frac{e(N)}{z-1} \tag{A.45}$$

$$\approx \frac{1}{(z-1)^2} \log_z(N) \tag{A.46}$$

$$\tag{A.47}$$

also scales with $\log_z(N)$, which is slow compared to regular networks [→ Eq. (A.28)]. The average distance in random networks is thus considered small.

A.5. Proof: Partialization as a matrix operation

The algorithm described in Sec. 2.2.7 is proven as follows [67]. The notation in this section is mostly in line with the original publication. Particularly, all vectors are column vectors, but often displayed as row vectors such that $\boldsymbol{Z} = (\boldsymbol{X}, \boldsymbol{Y})$ is written, where $\boldsymbol{Z} = \begin{pmatrix} \boldsymbol{X} \\ \boldsymbol{Y} \end{pmatrix}$ would be entirely correct. Please mind that $\mathrm{var}[(\boldsymbol{X}, \boldsymbol{Y})] = \mathrm{cov}[(\boldsymbol{X}, \boldsymbol{Y}), (\boldsymbol{X}, \boldsymbol{Y})]$ is different from $\mathrm{cov}(\boldsymbol{X}, \boldsymbol{Y})$.

Let $\boldsymbol{Z}$, $\boldsymbol{X}$, and $\boldsymbol{Y}$ be defined as in Sec. 2.2.6 with $u = \dim(\boldsymbol{X})$ and $v = \dim(\boldsymbol{Y})$. Without loss of generality assume $\mathrm{E}(\boldsymbol{Z}) = \boldsymbol{0}$. The linear least square predictor of $\boldsymbol{Y}$ from $\boldsymbol{X}$ is defined as

$$\boldsymbol{Y}(\boldsymbol{X}) = \mathrm{cov}(\boldsymbol{Y}, \boldsymbol{X}) \, \mathrm{var}(\boldsymbol{X})^{-1} \boldsymbol{X} \tag{A.48}$$

$$= \boldsymbol{B}\boldsymbol{X} \,, \tag{A.49}$$

where $\boldsymbol{B} = \operatorname{cov}(\boldsymbol{Y}, \boldsymbol{X}) \operatorname{var}(\boldsymbol{X})^{-1}$ is the $v \times u$ matrix of regression coefficients. The orthogonality of the residuals $\boldsymbol{Y} - \hat{\boldsymbol{Y}}$ on $\boldsymbol{X}$

$$\operatorname{cov}(\boldsymbol{Y} - \hat{\boldsymbol{Y}}, \boldsymbol{X}) = \operatorname{cov}(\boldsymbol{Y}, \boldsymbol{X}) - \operatorname{cov}(\boldsymbol{B}\hat{\boldsymbol{Y}}, \boldsymbol{X}) = 0 \tag{A.50}$$

follows by direct evaluation. Based on $\boldsymbol{B}$, the sweep operator

$$\boldsymbol{L} = \begin{pmatrix} \boldsymbol{I} & \boldsymbol{0} \\ -\operatorname{cov}(\boldsymbol{Y}, \boldsymbol{X}) \operatorname{var}(\boldsymbol{X})^{-1} & \boldsymbol{I} \end{pmatrix} \tag{A.51}$$

is defined. It is $\boldsymbol{L}(\boldsymbol{X}, \boldsymbol{Y}) = (\boldsymbol{X}, \boldsymbol{Y} - \hat{\boldsymbol{Y}})$; $\boldsymbol{L}$ is invertible. Because $\boldsymbol{L}$ inherits the orthogonality property from $\boldsymbol{B}$, $\operatorname{cov}[\boldsymbol{L}(\boldsymbol{X}, \boldsymbol{Y})]$ is block diagonal. By expanding

$$\operatorname{var}[\boldsymbol{L}(\boldsymbol{X}, \boldsymbol{Y})] = \operatorname{var}(\boldsymbol{X}, \boldsymbol{Y} - \hat{\boldsymbol{Y}}) \tag{A.52}$$

$$= \boldsymbol{L} \operatorname{var}(\boldsymbol{X}, \boldsymbol{Y}) \boldsymbol{L}^{\mathrm{T}}, \tag{A.53}$$

the expression

$$\operatorname{var}(\boldsymbol{X}, \boldsymbol{Y}) = \boldsymbol{L}^{-1} \operatorname{var}(\boldsymbol{X}, \boldsymbol{Y} - \hat{\boldsymbol{Y}}) \boldsymbol{L}^{-T} \tag{A.54}$$

is derived. Because $\operatorname{var}(\boldsymbol{X}, \boldsymbol{Y} - \hat{\boldsymbol{Y}})$ is block diagonal, the inverse of Eq. (A.54)

$$\operatorname{var}(\boldsymbol{X}, \boldsymbol{Y})^{-1} = \boldsymbol{L}^{\mathrm{T}} \operatorname{var}(\boldsymbol{X}, \boldsymbol{Y} - \hat{\boldsymbol{Y}})^{-1} \boldsymbol{L} \tag{A.55}$$

$$= \begin{pmatrix} \operatorname{var}(\boldsymbol{X})^{-1} + \boldsymbol{B}^{\mathrm{T}} \operatorname{var}(\boldsymbol{Y}|\boldsymbol{X})^{-1} \boldsymbol{B} & -\boldsymbol{B}^{\mathrm{T}} \operatorname{var}(\boldsymbol{Y}|\boldsymbol{X})^{-1} \\ -\operatorname{var}(\boldsymbol{Y}|\boldsymbol{X})^{-1} \boldsymbol{B} & \operatorname{var}(\boldsymbol{Y}|\boldsymbol{X})^{-1} \end{pmatrix} \tag{A.56}$$

$$=: \begin{pmatrix} \boldsymbol{E}_{\boldsymbol{XX}} & \boldsymbol{E}_{\boldsymbol{XY}} \\ \boldsymbol{E}_{\boldsymbol{YX}} & \boldsymbol{E}_{\boldsymbol{YY}} \end{pmatrix} =: \boldsymbol{E} \tag{A.57}$$

can easily be calculated. The notation $\operatorname{var}(\boldsymbol{Y}|\boldsymbol{X})$ refers to the variance of $\boldsymbol{Y}$ given all linear information of $\boldsymbol{X}$. It is the partial variance of $\boldsymbol{Y}$ with respect to $\boldsymbol{X}$. The matrix of the partial variance $\boldsymbol{E}$ is often called *concentration matrix*. Please note that $E_{\boldsymbol{YY}}$ is the inverse of the partial correlation of $\boldsymbol{Y}$ given $\boldsymbol{X}$.

The proof is completed by stating two corollaries which discuss the relationship of $\operatorname{var}(\boldsymbol{X}, \boldsymbol{Y})^{-1}$ to the partial correlation coefficients. The corollaries are a simple recaps of Corollary 5.8.1 and Corollary 5.8.2 from [67].

Corollary A.5.1. *Each diagonal element of the inverse variance is the reciprocal of a partial variance. [→ Corollary 5.8.1, [67]]*

Proof. Set $v = 1$ such that $E_{\boldsymbol{YY}}$ is scalar and

$$E_{\boldsymbol{YY}} = \operatorname{var}(\boldsymbol{Y} \,|\, \boldsymbol{X})^{-1} = 1/\operatorname{var}(\boldsymbol{Y} \,|\, \boldsymbol{X}_1, \boldsymbol{X}_2, \cdots, \boldsymbol{X}_u)\,. \tag{A.58}$$

As any diagonal element can be selected by first permuting the original random vector, the proposition is true for all diagonal elements. □

Corollary A.5.2. *Each diagonal element of the inverse variance, scaled to have a unit diagonal, is the negative of the partial correlation between the two corresponding variables, partiallized on all remaining variables. [→ Corollary 5.8.2, [67]]*

Proof. Set $v = 2$ and denote the elements of the 2×2 matrix $\boldsymbol{E_{YY}}$ by $\{e_{ij}\}$, then

$$\boldsymbol{E_{YY}} = \begin{pmatrix} e_{11} & e_{12} \\ e_{21} & e_{22} \end{pmatrix} = \operatorname{var}(\boldsymbol{Y} \,|\, \boldsymbol{X})^{-1} . \tag{A.59}$$

This can be rearranged for

$$\operatorname{var}(\boldsymbol{Y}|\boldsymbol{X}) = \begin{pmatrix} \operatorname{var}(\boldsymbol{Y}_1 \,|\, \boldsymbol{X}) & \operatorname{cov}(\boldsymbol{Y}_2, \boldsymbol{Y}_1 \,|\, \boldsymbol{X}) \\ \operatorname{cov}(\boldsymbol{Y}_1, \boldsymbol{Y}_2 \,|\, \boldsymbol{X}) & \operatorname{var}(\boldsymbol{Y}_2 \,|\, \boldsymbol{X}) \end{pmatrix} \tag{A.60}$$

$$= \frac{1}{e_{11}e_{22} - e_{21}e_{12}} \begin{pmatrix} e_{22} & -e_{12} \\ -e_{21} & e_{22} \end{pmatrix} . \tag{A.61}$$

After the matrices are normalized by their respective diagonal elements

$$\begin{pmatrix} 1 & \star \\ \operatorname{cov}(\boldsymbol{Y}_1, \boldsymbol{Y}_2 \,|\, \boldsymbol{X}) / \{\operatorname{var}(\boldsymbol{Y}_1 \,|\, \boldsymbol{X}) \operatorname{var}(\boldsymbol{Y}_2 \,|\, \boldsymbol{X})\}^{1/2} & 1 \end{pmatrix} = \begin{pmatrix} 1 & \star \\ -e_{12}/(e_{11}e_{22})^{1/2} & 1 \end{pmatrix} \tag{A.62}$$

$\operatorname{corr}(\boldsymbol{Y}_1, \boldsymbol{Y}_2 \,|\, \boldsymbol{X}) = -e_{12}/(e_{11}e_{22})^{1/2}$ is found by equating coefficients. The $\star$ represents its respective value from the lower triangular part of the matrix. As argued in Cor. A.5.1, permutation allows any two variables to be selected, and hence the argument applies to all off-diagonal entries. □

A.6. Taylor expansion of the inverse of a partial correlation matrix

In the Taylor expansion of a real function $f(r)$, r can be substituted by the square matrix $\boldsymbol{R}$, where the scalar operations translate to their matrix counterparts. If the convergence radius of the real function is $|r| < d$, than the Taylor series of the matrix function converges for $\|\boldsymbol{R}\| < d$ in case the matrix norm satisfies $\|\boldsymbol{AB}\| \leq \|\boldsymbol{A}\| \, \|\boldsymbol{B}\|$. The real function corresponding to the special case of calculating the inverse of $\mathbf{1} - \boldsymbol{R}$ is

$$f(r) = (1 - r)^{-1} . \tag{A.63}$$

It derivatives are

$$f'(r) = (1 - r)^{-2}, \quad f''(r) = 2(1 - r)^{-3}, \quad f^n(r) = n!(1 - r)^{-n-1} , \tag{A.64}$$

leading to the Taylor series about $r = 0$

$$Tf(r, r_0) = 1 + \sum_{m=1}^{\infty} r^m . \tag{A.65}$$

Consequently, the Taylor series of the matri-valued function is

$$Tf(\boldsymbol{R}, \boldsymbol{R}_0) = 1 + \sum_{m=1}^{\infty} \boldsymbol{R}^m = \sum_{m=0}^{\infty} \boldsymbol{R}^m \,. \tag{A.66}$$

Corollary A.6.1. *The matrix inverse of* $\mathbf{1} - \boldsymbol{R}$ *can be written as*

$$(\mathbf{1} - \boldsymbol{R})^{-1} = \sum_{m=0}^{\infty} \boldsymbol{R}^m \,. \tag{A.67}$$

The series converges for $\|\boldsymbol{R}\| < 1$.

Proof. It is

$$\left(\sum_{m=0}^{\infty} \boldsymbol{R}^m\right)(\mathbf{1} - \boldsymbol{R}) = \sum_{m=0}^{\infty} (\boldsymbol{R}^m) - \boldsymbol{R}^{m+1}) \tag{A.68}$$

$$= \mathbf{1} - \boldsymbol{R}^{m+1} \,. \tag{A.69}$$

If $\lim_{m\to\infty} \boldsymbol{R}^{m+1} = 0$ is satisfied $(\sum_{m=0}^{\infty} \boldsymbol{R}^m)(\mathbf{1} - \boldsymbol{R}) = \mathbf{1}$. Therefore, Cor. A.6.1 hold if $\|\boldsymbol{R}\| < 1$. □

Appendix B.

Supplement to maximum-likelihood estimation in the state-space model

B.1. Correlation of the three dimensional autoregressive chain

The process for which the elements of the covariance matrix are given in Eq. (4.3) is

$$\boldsymbol{X}(t) = \boldsymbol{C}\boldsymbol{X}(t-1) + \boldsymbol{\epsilon}(t)\,, \quad \boldsymbol{\epsilon}(t) \sim \mathcal{N}(\boldsymbol{0}, \boldsymbol{Q}) \tag{B.1}$$

with

$$\boldsymbol{C} = \begin{pmatrix} a_1 & 0 & 0 \\ b_{21} & a_2 & 0 \\ 0 & b_{32} & a_3 \end{pmatrix}\,, \quad \boldsymbol{Q} = \begin{pmatrix} q_1 & 0 & 0 \\ 0 & q_2 & 0 \\ 0 & 0 & q_3 \end{pmatrix}\,. \tag{B.2}$$

It is a stationary process, such that e.g., $\mathrm{var}[x_1(t-1)] = \mathrm{var}[x_1(t)]$ holds. It has expected value zero, $\mathrm{E}[\boldsymbol{x}(t)] = \boldsymbol{0}$. Its variance and covariance equations are derived as follows.

$$\begin{aligned} \mathrm{var}[X_1(t)] &= \mathrm{E}\{X_1(t)^2\} && \text{(B.3)} \\ &= \mathrm{E}\{[a_1 X_1(t-1) + \epsilon_1(t)]^2\} && \text{(B.4)} \\ &= a_1^2\,\mathrm{var}[X_1(t-1)] + \mathrm{var}[\epsilon_1(t)] && \text{(B.5)} \\ &= a_1^2\,\mathrm{var}[X_1(t)] + q_1 && \text{(B.6)} \\ &= \frac{q_1}{1-a_1^2} && \text{(B.7)} \end{aligned}$$

$$\begin{aligned}
\operatorname{cov}[X_1(t), X_2(t)] &= \mathrm{E}\{X_1(t)X_2(t)\} && \text{(B.8)}\\
&= \mathrm{E}\{[a_1X_1(t-1) + \epsilon_1(t)][a_2X_2(t-1) + \epsilon_2(t) \\
&\qquad + b_{21}X_1(t-1)]\} && \text{(B.9)}\\
&= a_1a_2 \operatorname{cov}[X_1(t-1), X_2(t-1)] + a_1b_{21} \operatorname{var}[X_1(t-1)] && \text{(B.10)}\\
&= \frac{a_1b_{21} \operatorname{var}[X_1(t)]}{1 - a_1a_2} && \text{(B.11)}
\end{aligned}$$

$$\begin{aligned}
\operatorname{var}[X_2(t)] &= \mathrm{E}\{[a_2X_2(t-1) + \epsilon_2(t) + b_{21}X_1(t-1)]^2\} && \text{(B.12)}\\
&= a_2^2 \operatorname{var}[X_2(t-1)] + \operatorname{var}[\epsilon_2(t-1)] + b_{21}^2 \operatorname{var}[X_1(t)] \\
&\qquad + 2a_2b_{21} \operatorname{cov}[X_1(t-1), X_2(t-1)] && \text{(B.13)}\\
&= \frac{q_2 + b_{21}^2 \operatorname{cov}[X_1(t), X_2(t)]}{1 - a_2^2} && \text{(B.14)}
\end{aligned}$$

$$\begin{aligned}
\operatorname{cov}[X_1(t), X_3(t)] &= \mathrm{E}\{X_1(t)X_3(t)\} && \text{(B.15)}\\
&= \mathrm{E}\{[a_1X_1(t-1) + \epsilon_1(t)] \\
&\qquad [a_3X_3(t-1) + \epsilon_3(t) + b_{32}X_2(t-1)]\} && \text{(B.16)}\\
&= a_1a_3 \operatorname{cov}[X_1(t-1), X_3(t-1)] \\
&\quad + a_1b_{32} \operatorname{cov}[X_1(t-1), X_2(t-1)] && \text{(B.17)}\\
&= \frac{a_1b_{32} \operatorname{cov}[X_1(t), X_2(t)]}{1 - a_1a_3} && \text{(B.18)}
\end{aligned}$$

$$\begin{aligned}
\operatorname{cov}[X_2(t), X_3(t)] &= \mathrm{E}\{X_2(t)X_3(t)\} && \text{(B.19)}\\
&= \mathrm{E}\{[a_2X_2(t-1) + \epsilon_2(t) + b_{21}X_1(t-1)] \\
&\qquad [a_3X_3(t-1) + \epsilon_3(t) + b_{32}X_2(t-1)]\} && \text{(B.20)}\\
&= a_2a_3 \operatorname{cov}[X_2(t-1), X_3(t-1)] \\
&\qquad + a_2b_{32} \operatorname{var}[X_2(t-1)] \\
&\qquad + a_3b_{21} \operatorname{cov}[X_1(t-1), X_3(t-1)] \\
&\qquad + b_{21}b_{32} \operatorname{cov}[X_1(t-1), X_2(t-1)] && \text{(B.21)}\\
&= \frac{1}{1 - a_2a_3}\{a_2b_{32} \operatorname{var}[X_2(t)] + a_3b_{21} \operatorname{cov}[X_1(t), X_3(t)] \\
&\qquad + b_{21}b_{32} \operatorname{cov}[X_1(t), X_2(t)]\} && \text{(B.22)}
\end{aligned}$$

$$\begin{aligned}
\operatorname{var}[X_3(t)] &= \mathrm{E}\{[a_3X_3(t-1) + \epsilon_3(t) + b_{32}X_2(t-1)]^2\} && \text{(B.23)}\\
&= a_3^2 \operatorname{var}[X_3(t-1)] + \operatorname{var}[\epsilon_3(t)] + b_{32}^2 \operatorname{var}[X_2(t-1)] \\
&\qquad + 2a_3b_{32} \operatorname{cov}[X_2(t-1), X_3(t-1)] && \text{(B.24)}\\
&= \frac{q_3 + b_{32}^2 \operatorname{var}[X_2(t)] + 2a_3b_{32} \operatorname{cov}[X_2(t), X_3(t)]}{1 - a_3^2} && \text{(B.25)}
\end{aligned}$$

B.2. Parameter update equations of the EM algorithm

A recap of the derivation of the parameter update equations of the EM algorithm for the transition matrix $\boldsymbol{C}$ and the covariance matrix of the driving and observational noise $\boldsymbol{Q}$, and $\boldsymbol{R}$, respectively, is given in this section. As the update equations evolve parameter values from the current EM iteration, say ς, to the next, say $\varsigma + 1$, the right hand side of each equation employs the parameter values of the ς-th EM iteration. The left hand side of each equation evaluates to the updated parameter values. These values are used in the $(\varsigma + 1)$-th EM iteration. On the left hand side, the iteration is denoted as superscript.

To derive the update equations, the partial derivatives of the expected value of the log-likelihood function

$$\begin{aligned}\hat{\mathcal{L}}(\boldsymbol{\Theta}) = &-\frac{1}{2}\log|\boldsymbol{\Sigma}_0| - \frac{1}{2}\operatorname{tr}\left\{\boldsymbol{\Sigma}_0^{-1}\left(\boldsymbol{P}_t^m + (\boldsymbol{x}_0^m - \boldsymbol{\mu})(\boldsymbol{x}_0^m - \boldsymbol{\mu})^{\mathrm{T}}\right)\right\} \\ &-\frac{m}{2}\log|\boldsymbol{Q}| - \frac{1}{2}\operatorname{tr}\left\{\boldsymbol{Q}^{-1}\left(\boldsymbol{\gamma} - \boldsymbol{\beta}\boldsymbol{C}^{\mathrm{T}} - \boldsymbol{C}\boldsymbol{\beta}^{\mathrm{T}} + \boldsymbol{C}\boldsymbol{\alpha}\boldsymbol{C}^{\mathrm{T}}\right)\right\} \\ &-\frac{m}{2}\log|\boldsymbol{R}| \\ &-\frac{1}{2}\operatorname{tr}\left\{\boldsymbol{R}^{-1}\sum_{t=1}^{m}\left[(\boldsymbol{y}_t - \boldsymbol{O}\boldsymbol{x}_t^m)(\boldsymbol{y}_t - \boldsymbol{O}\boldsymbol{x}_t^m)^{\mathrm{T}} + \boldsymbol{O}\boldsymbol{P}_t^m\boldsymbol{O}^{\mathrm{T}}\right]\right\},\end{aligned} \tag{B.26}$$

with respect to each parameter is solved for zero. The substitutions

$$\begin{aligned}\boldsymbol{\alpha} &= \sum_{t=1}^{m}\left[\boldsymbol{P}_{t-1}^m + \hat{\boldsymbol{x}}_{t-1}^m(\hat{\boldsymbol{x}}_{t-1}^m)^{\mathrm{T}}\right], \\ \boldsymbol{\beta} &= \sum_{t=1}^{m}\left[\boldsymbol{P}_{t,t-1}^m + \hat{\boldsymbol{x}}_t^m(\hat{\boldsymbol{x}}_{t-1}^m)^{\mathrm{T}}\right], \\ \boldsymbol{\gamma} &= \sum_{t=1}^{m}\left[\boldsymbol{P}_t^m + \hat{\boldsymbol{x}}_t^m(\hat{\boldsymbol{x}}_t^m)^{\mathrm{T}}\right],\end{aligned} \tag{B.27}$$

are used in $\hat{\mathcal{L}}(\boldsymbol{\Theta})$. Non-standard matrix operations are taken from the *Matrix Cookbook* [92]. Please mind that covariance matrices are real and symmetric.

B.2.1. Update equation for the transition matrix

The partial derivative of $\hat{\mathcal{L}}$ with respect to the transition matrix $\boldsymbol{C}$ leads to

$$\begin{aligned}-2\frac{\partial\hat{\mathcal{L}}}{\partial\boldsymbol{C}} &= \frac{\partial}{\partial\boldsymbol{C}}\operatorname{tr}\left[\boldsymbol{Q}^{-1}\left(-\boldsymbol{\beta}\boldsymbol{C}^{\mathrm{T}} - \boldsymbol{C}\boldsymbol{\beta}^{\mathrm{T}} + \boldsymbol{C}\boldsymbol{\alpha}\boldsymbol{C}^{\mathrm{T}}\right)\right] \\ &= -\boldsymbol{Q}^{-1}\boldsymbol{\beta} - \boldsymbol{Q}^{-1}\boldsymbol{\beta} + \boldsymbol{Q}^{-1}\boldsymbol{C}\boldsymbol{\alpha}^{\mathrm{T}} + \boldsymbol{Q}^{-1}\boldsymbol{C}\boldsymbol{\alpha}^{\mathrm{T}} \\ &= -2 + \boldsymbol{C}\boldsymbol{\alpha}^{\mathrm{T}}\boldsymbol{\beta}^{-1} + \boldsymbol{C}\boldsymbol{\alpha}\boldsymbol{\beta}^{-1} \\ &= -2 + 2\boldsymbol{C}\boldsymbol{\alpha}\boldsymbol{\beta}^{-1} \\ &= 0,\end{aligned} \tag{B.28}$$

which is solved for $\boldsymbol{C}$, such that the parameter update

$$\boldsymbol{C}^{\varsigma+1} = \boldsymbol{\beta}\boldsymbol{\alpha}^{-1}\,, \tag{B.29}$$

is found [32].

B.2.2. Update equation for the driving noise covariance matrix

In order to derive the update equation for the covariance $\boldsymbol{Q}$ of the driving noise

$$\boldsymbol{F} = \boldsymbol{\gamma} - \boldsymbol{\beta}\boldsymbol{C}^{\mathrm{T}} - \boldsymbol{C}\boldsymbol{\beta}^{\mathrm{T}} + \boldsymbol{C}\boldsymbol{\alpha}\boldsymbol{C}^{\mathrm{T}} \tag{B.30}$$

is substituted in Eq. (B.26), such that

$$\begin{aligned} -2\frac{\partial\hat{\mathcal{L}}}{\partial\boldsymbol{Q}} &= \frac{\partial}{\partial\boldsymbol{Q}}\left[m\log|\boldsymbol{Q}| + \mathrm{tr}\left(\boldsymbol{Q}^{-1}\boldsymbol{F}\right)\right] \\ &= m\boldsymbol{Q}^{-1} - \boldsymbol{Q}^{-1}\boldsymbol{F}^{\mathrm{T}}\boldsymbol{Q}^{-1} \\ &= m\boldsymbol{Q}^{\mathrm{T}} - \boldsymbol{F}^{\mathrm{T}} \\ &= 0 \end{aligned} \tag{B.31}$$

is derived. By solving for $\boldsymbol{Q}$, the expression

$$\begin{aligned} \boldsymbol{Q}^{\varsigma+1} &= \frac{1}{m}\boldsymbol{F} \\ &= \frac{1}{m}\left(\boldsymbol{\gamma} - \boldsymbol{\beta}\boldsymbol{C}^{\mathrm{T}} - \boldsymbol{C}\boldsymbol{\beta}^{\mathrm{T}} + \boldsymbol{C}\boldsymbol{\alpha}\boldsymbol{C}^{\mathrm{T}}\right) \end{aligned} \tag{B.32}$$

is found. Using Eq. (B.29), this result can be simplified to [32]

$$\begin{aligned} \boldsymbol{Q}^{\varsigma+1} &= \frac{1}{m}\left(\boldsymbol{\gamma} - \boldsymbol{\beta}\boldsymbol{\alpha}^{-1}\boldsymbol{\beta}^{\mathrm{T}} - \boldsymbol{\beta}\boldsymbol{\alpha}^{-1}\boldsymbol{\beta}^{\mathrm{T}} + \boldsymbol{\beta}\boldsymbol{\alpha}^{-1}\boldsymbol{\alpha}\boldsymbol{\alpha}^{-1}\boldsymbol{\beta}^{\mathrm{T}}\right) \\ &= \frac{1}{m}\left(\boldsymbol{\gamma} - \boldsymbol{\beta}\boldsymbol{\alpha}^{-1}\boldsymbol{\beta}^{\mathrm{T}}\right)\,. \end{aligned} \tag{B.33}$$

B.2.3. Update rule for the observational noise covariance matrix

By the substitution

$$\boldsymbol{F} = \sum_{t=1}^{m}\left[\left(\boldsymbol{y}_t - \boldsymbol{O}\boldsymbol{x}_t^m\right)\left(\boldsymbol{y}_t - \boldsymbol{O}\boldsymbol{x}_t^m\right)^{\mathrm{T}} + \boldsymbol{O}\boldsymbol{P}_t^m\boldsymbol{O}^{\mathrm{T}}\right] \tag{B.34}$$

in Eq. (B.26), the expression

$$\begin{aligned} -2\frac{\partial\hat{\mathcal{L}}}{\partial\boldsymbol{R}} &= \frac{\partial}{\partial\boldsymbol{R}}m\log|\boldsymbol{R}| + \mathrm{tr}\left(\boldsymbol{R}^{-1}\boldsymbol{F}\right) \\ &= m\boldsymbol{R}^{-1} - \boldsymbol{R}^{-1}\boldsymbol{F}^{\mathrm{T}}\boldsymbol{R}^{-1} \\ &= 0 \end{aligned} \tag{B.35}$$

is derived. By solving for $\boldsymbol{R}$, the update equation for the covariance matrix of the observational noise

$$\boldsymbol{R}^{\varsigma+1} = \frac{1}{m}\sum_{t=1}^{m}\left[\left(\boldsymbol{y}_t - \boldsymbol{O}\boldsymbol{x}_t^m\right)\left(\boldsymbol{y}_t - \boldsymbol{O}\boldsymbol{x}_t^m\right)^{\mathrm{T}} + \boldsymbol{O}\boldsymbol{P}_t^m\boldsymbol{O}^{\mathrm{T}}\right] . \tag{B.36}$$

is determined [32].

Index